The Role of Crustal Magnetic Fields in Atmospheric Escape from Mars

by

Tristan David Weber

B.S.E., University of Michigan, 2014

M.S., University of Colorado, Boulder, 2017

A thesis submitted to the

Faculty of the Graduate School of the

University of Colorado in partial fulfillment

of the requirements for the degree of

Doctor of Philosophy

Department of Astrophysical and Planetary Sciences

2020

This thesis entitled:
The Role of Crustal Magnetic Fields in Atmospheric Escape from Mars
written by Tristan David Weber
has been approved for the Department of Astrophysical and Planetary Sciences

_____
Prof. David Brain

_____
Prof. Fran Bagenal

_____
Prof. Robert Ergun

_____
Prof. Bruce Jakosky

_____
Prof. Jeffrey Thayer

Date _____

The final copy of this thesis has been examined by the signatories, and we find that both the content and the form meet acceptable presentation standards of scholarly work in the above mentioned discipline.

Weber, Tristan David (Astrophysical and Planetary Sciences)

The Role of Crustal Magnetic Fields in Atmospheric Escape from Mars

Thesis directed by Prof. David Brain

Magnetic fields may have played an important role in shaping the planetary evolution of Mars. Through their ability to guide the flow of charged particles, magnetic fields facilitate both the input of energy and the escape of planetary ions, which at Mars has contributed to the loss of the planet's atmosphere over time. This atmospheric loss has been a primary driver of Martian evolution, altering the planet from one that sustained flows of liquid water to the cold, dry world we observe today.

In this thesis, I use data from the MAVEN spacecraft to characterize the magnetic field environment of Mars, placing a particular emphasis on how Martian crustal magnetic fields affect atmospheric escape.

Through measurements of electron pitch angle distributions and magnetic fields, I analyze magnetic topology throughout the Martian system, allowing us to determine where magnetic fields are providing avenues for energy input and ion escape at Mars. This work was then used as a foundation for the creation of a new technique for identifying magnetic topology at Mars.

I then perform studies of how Martian magnetic topology responds to changes in upstream solar wind conditions, namely solar wind pressure and interplanetary magnetic field direction. Solar wind conditions are expected to have been drastically different throughout solar system history, so an understanding of how magnetic fields at Mars respond to these conditions is needed in the context of interpreting long term evolution. I find that changes in solar wind pressure alter the morphology of crustal magnetic field structures, and that changes in upstream IMF cause local variations in topology on consistent, daily timescale.

Finally, I couple the previous works with direct measurements of escaping ions to estimate the influence that crustal magnetic fields have on atmospheric escape. I find that crustal fields typically

inhibit ion escape from Mars, but that under certain conditions they can instead cause localized enhancements in escape. Comparisons with modeling results in the future may help determine precisely what conditions are necessary for this to occur.

Analysis of the Martian crustal magnetic fields may act as a gateway toward understanding the importance of planetary magnetic fields in general. As we begin to study more and more worlds throughout the universe, the work of this thesis could represent a small step toward characterizing the habitability of planets in general.

Dedication

"It's still magic even if you know how it's done."

- Terry Pratchett, *A Hat Full of Sky*

Acknowledgements

Defending a thesis in 2020, particularly one focused so heavily on other planets, carries with it a strange feeling. Amidst a worldwide pandemic, a painful political swing toward hateful nationalism, and the continued flareups of centuries-long racial inequities, it seems increasingly indefensible to spend so much time dedicated to studying something that is far removed from everyday life and the issues we face here on Earth.

I offer no rebuttal to this thought. It's one that I struggle with on a weekly if not daily basis, and depending on my emotional state such ideas often bring me close to leaving space research and pursuing some other discipline. Yet here I remain, and though I can't provide any counterargument, what I can offer is a sincere expression of hope and of gratitude.

I feel hopeful that studying other worlds can help us as humans gain a deeper appreciation for our place in the universe and for one another. I feel hopeful that the work we do as professional scientists can help shift the public awareness toward rational and effective humanitarian ideals. And I feel hopeful that those who are lucky enough to have scientific research as a profession will put in the necessary effort to make such opportunities available to everyone. Studying Mars is a luxury, make no mistake. But it is a luxury that I hope is soon available to everyone who feels that tug of curiosity when they look up at the night sky.

And I feel gratitude – gratitude in particular to all of the people that make others feel safe and loved. In a year of hardship like this one, I can think of nothing more important. In my own life, I'm incredibly blessed to have many such people to thank. Thank you to my mom, who early in my life instilled in me a true love of learning, and who throughout years of change has always

provided a steady, comforting cushion of love and support. Thank you to my dad for teaching me to have a Zen, thoughtful outlook on life, and for getting me to stay up late by the campfire to watch meteor showers and talk about science fiction. Thank you to my sister Kiana, who continues to inspire and amaze me by lighting up stages and Broadway shows as a literal rock star, while somehow still being so humble that she treats *me* like I'm the cool sibling. Thank you to Martin for entering into our family with so much love and care.

Thank you so very much to each and every person that helped me manage and overcome my panic attacks – I don't think I could have done it without you.

Thank you to my APS cohort who managed to stay cheery and supportive of each other through late nights, frustrating work loads, and impenetrable lectures, all while tolerating my endless requests for one more game of masquerade. Thank you to the numerous APS grad students that helped foster fun and inclusive community throughout the years. Thank you and *rock on* to both Gluten for Punishment and The Trash Pandas for rekindling my passion for noisy music and rowdy performance. Thank you to the wonderful, wild, irreplaceable Jeeps for creating a family of fun and laughter here – your friendship has truly made this my home. Thank you to the Boulder ultimate frisbee community for taking me into the fold and igniting in me a love of sports and athletics that I'd never before been able to find. An enormous thank you to my advisor Dave Brain for the years of encouragement, advice, patient instruction, and infectious enthusiasm. I quite honestly can't imagine a better mentor to guide my scientific (and personal) growth, and I feel strongly that choosing to work for you was among the best decisions I've ever made.

And, of course, thank you to Jackson. Your constant presence in my life holds me together in more ways than you may know.

Contents

Tables

Table

Figures

Figure

Preface

One of the more overstated ideas in popular science articles is that Mars became a cold, dead planet simply due to the loss of its magnetic field. Upon the time of writing this thesis, a web search of "What happened to Mars?" returns a host of articles recounting the planet's demise, including one stating that "after Mars's magnetic field disappeared, the solar wind stripped the atmosphere away", one arguing that "Earth is a world teeming with life while Mars is a barren wasteland ... due to the presence of our planet's magnetic field", and one particularly on-the-nose essay simply titled "Death by Magnetic Field". Upon my entry into graduate school, such was my confident understanding of the history of Mars, marking me as one of the many students lucky enough to feel less knowledgeable upon the completion of their PhD than they did when starting. This is what growth looks like, I am assured.

This is not to say that the idea of "Death by Magnetic Field" is necessarily wrong, per se. We just don't know it to be the case. Planetary systems that we can reach to use as data points are few and far between, and those with verified habitability are almost nonexistent (there's just the one, really). By definition this makes it difficult for us to determine just how important any single factor is in a planet's evolution. Earth, our defining example of what habitability means, does possess a strong magnetic field, but did Mars need a magnetic field to maintain its own habitability? Do other planets? Maybe. Probably not.

In truth, the line of reasoning makes intuitive sense. We now know for certain that Mars once had water on its surface. To sustain this water it must have once had a thicker atmosphere. And protecting the atmosphere it once had a magnetic dynamo, a planet-sized force field much like

the one we are lucky enough to have here at Earth, shielding us from the solar wind. Once this magnetic field disappeared, it's natural to expect that the water followed soon after.

As with any problem the size of a planet, though, the reality of the situation is much more complex.

Each link in this chain of logic has its own set of caveats and clarifications (several of which will be discussed in this thesis), and even the assumption that Mars was once habitable may be a flawed one. Persistent scientific efforts continue to refine our understanding of how planets evolve, but it remains unclear whether global magnetic fields are truly important for planetary habitability.

Herein lies my contribution toward answering this question. As a doctoral dissertation, it contains many of the typical features one might expect. Grandiose big-picture ideas, clinical scientific language, and intensely specific minutia all can be found within. At times it is focused and precise, at others wild and uncontrolled, and at all points it represents the culminating output of hundreds of hours of work, thought, and emotional energy.

In other words, here be science. Enter if ye dare.

Chapter 1

Introduction

1.1 Water on Mars

The Martian surface contains extensive evidence that water once flowed across the planet. This has been speculated since as early as the 1800s, when early telescope observations led some astronomers to conclude that large channels of water stretched across the planet's surface (Figure 1.1, Schiaparelli, 1882). Some even went so far as to say that these features must be canals, carved by intelligent beings. All such claims were incorrect, and were later shown to have simply been due to optical illusions from low resolution telescopes (Evans and Maunder, 1903). The idea remained in the public consciousness, however, and serious discussion of water on Mars was revived in the 1970s when the Mariner 9 spacecraft returned images of winding erosional features carved into the Martian surface (Figure 1.2a). Since then, a wealth of morphological evidence for water on early Mars has been recorded, including extensive valley networks (Figure 1.2b), deltas deposited by ancient rivers (Figure 1.2c), and outflow channels carved by catastrophic flows (Figure 1.2d). Alongside these features we also find abundant mineralogical evidence (see Ehlmann and Edwards, 2014, and references within). Spectroscopic images from orbiting spacecraft reveal widespread aqueous minerals that would only have formed through persistent contact with water. Rovers on the surface have discovered hematite "blueberries", formed through the flow of water through iron-rich sediments, and phyllosilicate clays that signal the presence of an ancient lake bed.

Together, these findings make it clear that surface water was a regular feature on early Mars, and that it played a large role in the planet's geological history. On Mars today, however, the atmospheric temperature and pressure are too low to support any significant amount of stable liquid water. From this we infer that Mars must have previously held a much thicker atmosphere, with an associated greenhouse effect that could provide the required warmer temperatures.

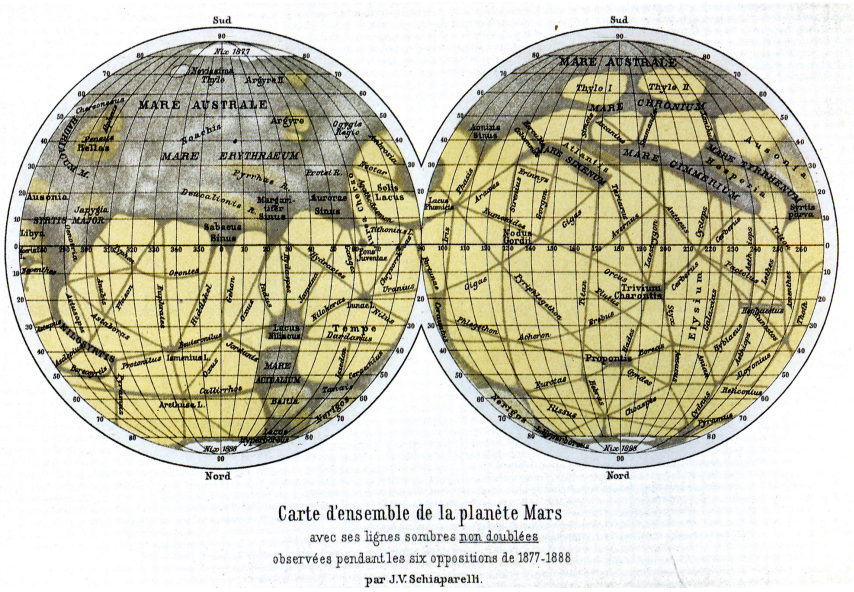

Figure 1.1: Giovanni Schiaparelli's 1888 map of speculated water channels on Mars.

In analyzing the time history of the Martian climate, it is important to note that evidence of past surface water is found almost exclusively on Mars's more ancient terrains. This can be seen in Figure 1.3, which contains maps of where we have currently identified valley networks and aqueous minerals. These features are scattered broadly across Mars's ancient southern highlands, which were formed 4.1-3.7 billion years ago. The younger Northern lowlands, most of which finished forming by 3.4-3.0 billion years ago, appear to have experienced little contact with surface water. This suggests that stable flows of surface water ceased to operate somewhere between these two time periods, marking the planet's primary transition to the cold and dry world that we observe today. This transition is not currently well understood, though it appears to have been a gradual shift that was still marked by sporadic fluvial activity. Large outflow channels appear to have been

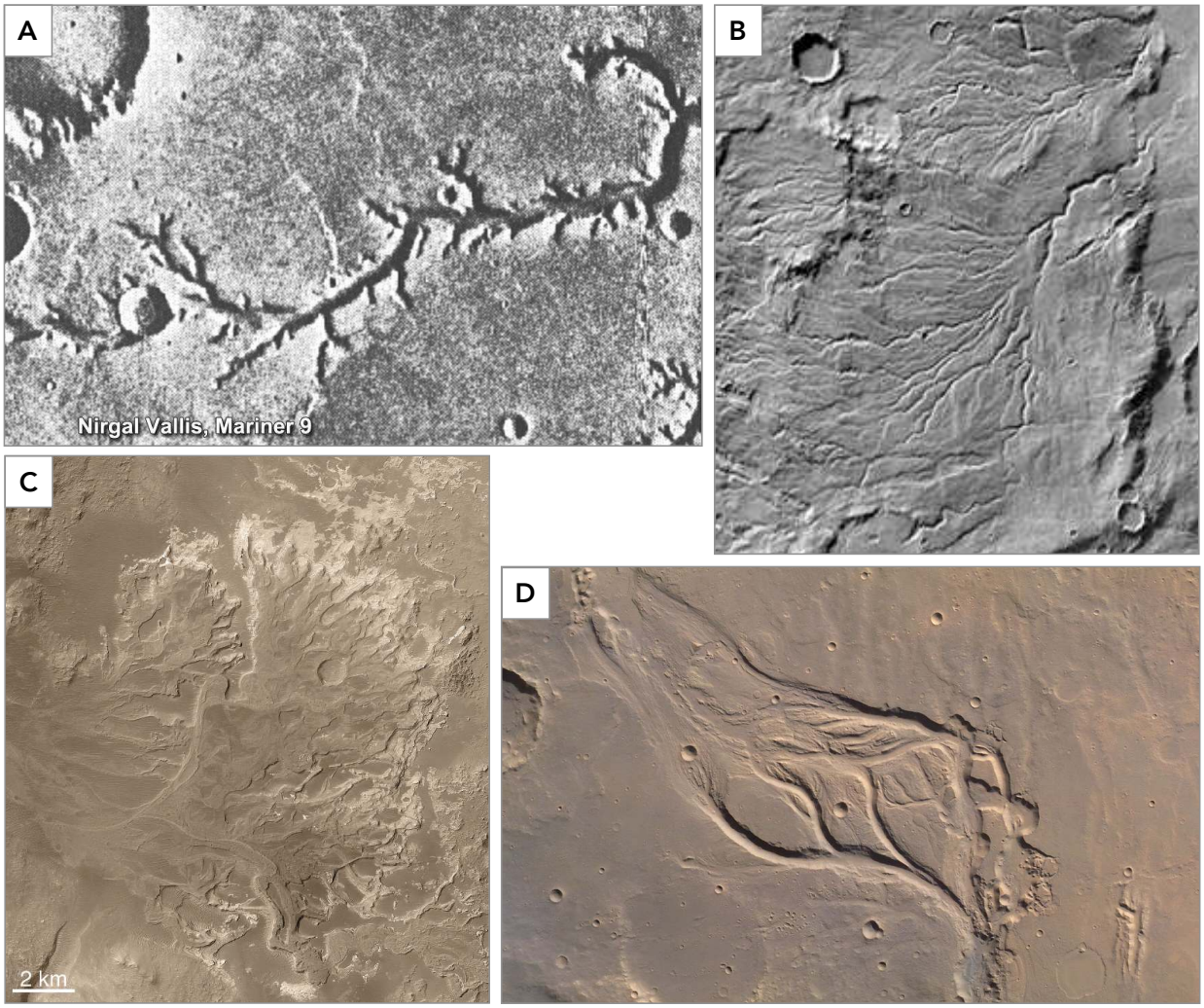

Figure 1.2:
(A) Nirgal Vallis, an ancient river channel, as captured by the Mariner 9 spacecraft. *Image Credit: NASA/JPL-Caltech.*
(B) Valley Network formation in Warrego Valles. *Image credit NASA/JPL-Caltech.*
(C) Eberswalde Delta, captured by Mars Global Surveyor. *Image Credit: NASA/JPL/MSSS.*
(D) Outflow channel near Aurorae Chaos, imaged by Mars Express. *Image Credit: ESA/DLR/FU Berlin/J. Cowart, CC BY-SA 3.0 IGO.*

carved by catastrophic floods during this time (e.g. Chapman et al., 2010). Inverted river beds and valley networks can be found in some terrains that formed 3.5-3.0 billion years ago (e.g. Griffin and Zimbelman, 2009; Kerber and Head, 2010). And mineralogical evidence from Gale crater suggests that lake sediments were deposited there sometime after the crater's formation ∼3.7 billion years ago (Grotzinger et al., 2015).

The history of liquid water on Mars therefore appears to be long and complex. With some certainty, however, we are able to make the following claims:

(1) Prior to 3.5 billion years ago, liquid water flowed regularly across the surface of Mars.

(2) Maintaining flows of this kind would have required a thicker atmosphere than we find on Mars today.

(3) By 3.0 billion years ago, regular flows of liquid surface water had ceased.

(4) Today, only 6 mbar of atmosphere remain at Mars, and the planet's surface is cold and dry.

From this we find ourselves naturally asking "why did Mars lose its atmosphere?". This has been an active subject of study for the past thirty years, and with recent results from orbiting spacecraft and ground-based rovers we become ever-closer to reaching an answer. Our current state of understanding is outlined in the next sections.

1.2 Atmospheric Loss at Mars

Here we will discuss a series of different processes that have contributed to atmospheric loss at Mars. In the context of habitability, our main focus is in understanding what drove the removal of the atmosphere that existed 4.0-3.5 billion years ago, when surface water was common. It is currently debated just how thick the atmosphere must have been at this point. Though there is agreement that the surface of early Mars must have been warmer and wetter than we observe today, exactly how much warmer or how much wetter remains an open question (see Wordsworth, 2016, and references within). Studies analyzing the distribution of crater sizes on Mars have suggested

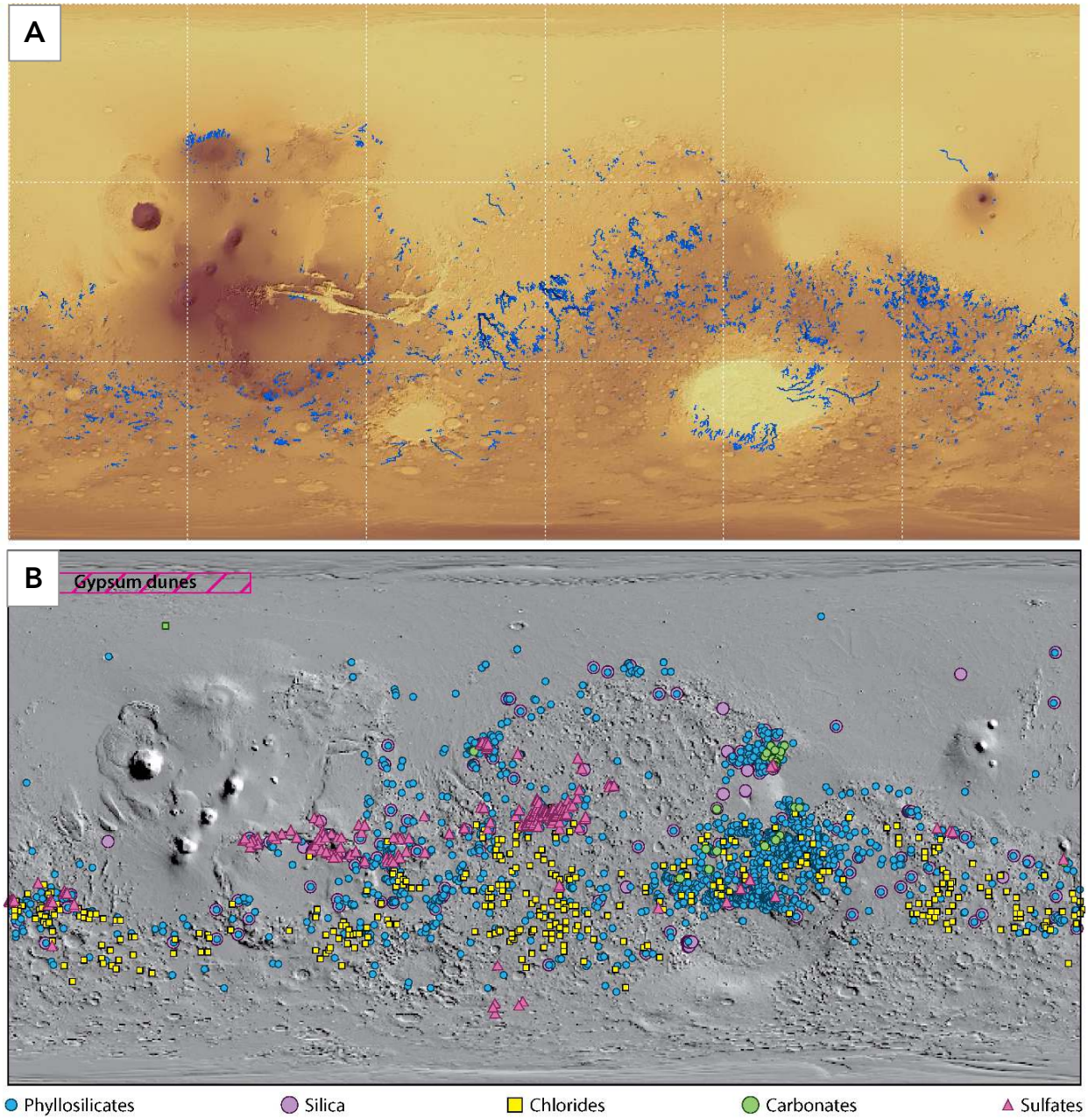

Figure 1.3:
(A) Identified locations of valley networks on Mars, from Hynek et al. (2010).
(B) Map of identified aqueous mineral deposits on Mars, from Ehlmann and Edwards (2014).

that Mars likely had 1-4 bar of atmosphere as recently as 3.6 billion years ago, though the error bars on such calculations can be very high. A recent study by Jakosky et al. (2018) suggests that it is not unreasonable to expect that at least one bar of atmosphere has been lost over time. We therefore use this number as a point of comparison in this section when discussing the atmospheric loss processes that may have shaped the evolution of the Martian climate.

1.3 Ground sequestration

Some fraction of the atmospheric loss at Mars has been due to absorption into the planet's surface. The total amount lost over time in this way is currently unknown, but estimates have been constructed based on analysis of the possible reservoirs in which atmospheric volatiles could be stored. The Martian polar caps, for example, contain seasonal deposits of CO_2 ice that can contain up to a third of the current Martian atmosphere during winter (the equivalent of $\sim$2 mbar). This does not represent a long-term store of atmospheric carbon, as the CO_2 ice sublimates back into the atmosphere come summer, but the polar caps also contain a large covering of water ice that could potentially trap CO_2 via clathrate structures (Dobrovolskis and Ingersoll, 1975). Even so, recent studies have shown it unlikely that the polar caps account for any large volume of stored atmospheric sequestration, with most estimates suggesting they contain just a few millibars of CO_2 (Stewart and Nimmo, 2002). A much larger atmospheric reservoir is that of carbon bearing minerals, formed through chemical reactions between water, atmospheric CO_2, and metal ions in Martian rocks. The resulting carbonate minerals were long expected to be the key to Mars' missing atmosphere (e.g. Pollack et al., 1987), but analysis of Martian surface dust (Bandfield et al., 2003) and carbonate outcroppings (Ehlmann et al., 2008) have found markedly low concentrations of carbonate minerals. In total, the carbonate deposits that we have found appear to account for at most 12 mbar of dissolved CO_2, a small fraction of the original Martian atmosphere (Edwards and Ehlmann, 2015). This suggests that the atmosphere lost from Mars must have either (1) been stored in much deeper carbonate deposits, inaccessible and hidden from view, or (2) escaped to space, leaving the planet permanently. In assessing the first possibility, a study by Wray et al.

(2016) found evidence of subsurface carbonate minerals exposed by impact craters and erosion features. Outside of opportunities provided by natural geology of this kind, however, we currently have no straightforward way of investigating the deep subsurface of Mars. Instead, we turn toward analyzing the possibility that much of the Martian atmosphere has escaped to space over time.

1.4 Escape to Space

In order for an atmospheric particle to escape to space, it must gain enough energy to overcome the planet's gravitational potential well. This requires reaching the planet's escape velocity, $v = \sqrt{\frac{2GM_M}{r}}$, where G is the gravitational constant, M_M is the mass of Mars, and r is the particle's distance from the center of the planet. At the surface of Mars, a particle would theoretically need be traveling upward at 5.03 km/s to escape the planet, but in practice such a particle would certainly collide with other atmospheric particles along the way, losing its energy and remaining bound to the planet. It is therefore more useful to consider particles escaping from the planet's exosphere, the region of space where the atmosphere is sparse enough to make collisions unlikely. The transition into this region, referred to as the exobase, is typically taken to occur at the altitude where the mean free path of a particle becomes larger than the atmospheric scale height. At Mars, this balance occurs at an altitude of roughly 170 km, varying between 140 to 200 km depending on season and solar zenith angle (Jakosky et al., 2017). At this altitude, atmospheric scale heights of 10 to 15 km are typical. And though we often refer to the exobase as occurring at a single specific altitude, it is more properly thought of as a transition region that is 10-20 km thick (see, e.g. Fox and Hać, 2009). Additionally, because ions, electrons, and neutral particles each have different collision cross-sections, they will also each have slightly different exobase altitudes. The exobase is typically found at 180-200 km for ions and 140-170 km for electrons, though the both of these depend on the local magnetic field environment as well (Xu et al., 2017b).

With all of these caveats in mind, we can construct a reasonable benchmark for particle escape from Mars: Any particle that reaches the exobase moving upwards at greater than escape velocity ($\sim$ 4.9 km/s at this altitude) is likely to escape the planet. Physical mechanisms for escape

are therefore considered to be those that can bring particles to this state. In practice, most such mechanisms provide energy to particles more directly than they provide velocity, so we tend to analyze whether particles can be brought to escape *energy*, a mass-dependent quantity. Hydrogen, for example, need only reach an energy of 0.13 eV to escape, whereas O and O_2 must reach 2 eV and 4 eV respectively.

In the following sections we will discuss several different processes that can energize particles enough to escape. Each of these processes has contributed to atmospheric escape over time in some capacity, but calculating the total amount of atmosphere that each has caused to be lost to space remains a highly complex problem. With recent observations and modeling studies, we now have fairly robust estimates for present-day escape rates, but using these rates to extrapolate backwards in time requires us to consider how they would have varied throughout Martian history. This encompasses a range of solar conditions, ever-changing atmospheric parameters, and variations in geologic activity, each of which are relatively unconstrained at the present. For each process discussed here, we will therefore provide estimates of both the present day escape rate and the total contribution to atmospheric loss, but it is worth noting here that the latter will always carry a high degree of uncertainty. A summary of these estimates is provided in Figure 1.4. Additionally, we note here that it is possible that this is not an exhaustive list. Studies of the planets in our solar system suggest that these are the dominant escape channels to consider, but there remains the possibility that some important mechanism has escaped our attention thus far.

1.4.1 Jeans Escape

In a collisional atmosphere, particle energies are spread across a thermal distribution that is determined by their density and temperature. When some fraction of this distribution exceeds the escape energy, those particles are able to escape directly, a process referred to as Jeans escape. Because the energy required for escape scales directly with mass, Jeans escape is most efficient at removing light particles from an atmosphere. At Mars specifically, the typical thermospheric temperature of 250-300 K is often sufficient to provide escape energy to a significant fraction of H

	Current escape [10^{24} s^{-1}]	Integrated escape over time	Primary escaping species	Notes/Caveats
Jeans Escape	500	50 - 100 m GEL of water	H_2, H	Primarily responsible for loss of water, not CO_2 or other dominant atmospheric constituents.
Photochemical Escape	20 - 70	270 - 700 mbar	O	Estimates are highly dependent on EUV flux and particle interaction cross-sections.
Ion Escape	2 - 5	5 - 1000(?) mbar	O^+, O_2^+	Loss early in Martian history has high uncertainty
Sputtering	0.1 - 0.5	>600 mbar	All	No direct observations. Estimates come from models and isotope fractionation data.
Hydrodynamic Escape	—	>70% of initial gas	All	Almost all occurred prior to 4 billion years ago.
Impact Erosion	—	10 - 800 mbar	All	Almost all occurred prior to 3.8 billion years ago.

Figure 1.4: Table of escape rates for known atmospheric loss processes. Integrated escape estimates are calculated methods that vary by study. The references for each of these estimates are presented in the corresponding subsections of Section 1.4.

and H_2 particles, but to almost no particles of heavier species such as O and CO_2. Additionally, lighter isotopes of a given species are more likely to escape, meaning that over time Jeans escape can lead to an increase in the D/H ratio of an atmosphere. Mars's current D/H ratio is over five times larger than that of Earth (Krasnopolsky et al., 1997), suggesting that Jeans escape is responsible for the loss of a substantial amount of Hydrogen throughout Martian history. Recent studies of Jeans escape at Mars have calculated a present-day escape rate of $5 \times 10^{26}\,s^{-1}$, with variations of up to several orders of magnitude depending on season and the presence of dust-storms (Chaffin et al., 2014; Bhattacharyya et al., 2015; Yamauchi et al., 2015; Rahmati et al., 2017; Heavens et al., 2018). If we assume that Hydrogen lost from mars is all initially sourced from H_2O, then total amount of H loss to space over the last 4 billion years corresponds to an initial inventory of water equivalent to a global layer 50-100 m deep (Mahaffy et al., 2015).

1.4.2 Hydrodynamic escape

As low-mass particles escape the atmosphere of Mars (primarily through Jeans escape), any collisions that they experience can transfer energy and momentum to heavier atmospheric species. If escape fluxes are strong enough, this can energize the heavier particles such that they escape as well. The result is essentially an upward wind of light species that "drags" atmospheric heavies along with it, a process referred to as hydrodynamic escape. At present-day Mars, the escape flux of Hydrogen is not high enough for hydrodynamic escape to have any significant effect, and modeling studies have shown that this has likely been the case for the last four billion years (e.g. Zahnle and Kasting, 1986). In the first few hundred million years after the planet's formation, however, the EUV environment was much more intense. This is expected to have driven large quantities of hydrodynamic escape, removing nearly all of the initial Martian atmosphere (Lammer et al., 2011). Similar loss of atmosphere was likely experienced by all the terrestrial planets. This all occurred well before the last known time that water flowed on Mars, however, and therefore is often not included in discussions of Martian habitability.

1.4.3 Photochemical Escape

As particles in Mars's atmosphere are continually ionized or dissociated by solar photons, a range of ionized and neutral species are created (e.g. Benna et al., 2015). The resulting mixture of particles facilitates a complex set of chemical reactions, some of which are exothermic enough to provide particles with escape energy. This process is referred to as photochemical escape, and has been the subject of many modeling studies (McElroy et al., 1977; Lammer and Bauer, 1991; Fox, 1993; Fox and Hać, 2009). Informed by spacecraft observations of particle densities and temperatures, these studies have determined that photochemical escape is likely the primary driver of neutral escape at Mars today for elements heavier than hydrogen. In particular, large amounts of oxygen escape is driven by the dissociative recombination of O_2+, in which an O_2+ ion recombines with an electron to create two neutral oxygen atoms. These oxygen atoms are imparted with the energy released in the reaction, which is typically enough to bring both of them to escape energy. Dissociative recombination also occurs for $CO_2{}^+$, CO^+, and N^+, leading to the escape of neutral carbon and nitrogen as well.

However, despite this wealth of modeling results, direct measurement of photochemical escape remains difficult. This is largely because the hot oxygen corona of Mars is a broad and tenuous region, and distinguishing between bound and escaping oxygen requires us to resolve a very small difference in energy located at a very low energy range ($\sim$ 2eV). Instead, studies tend to infer the rate of photochemical escape using comparisons of plasma measurements to empirical models (Rahmati et al., 2017; Lillis et al., 2017). These studies calculate present-day escape rates of $\sim 5 \times 10^{25}\ \mathrm{s}^{-1}$. Using this number, Lillis et al. (2017) calculate that photochemical escape could account for roughly 500 mbar of atmosphere lost over Mars's history, though uncertainty associated with the dependence of this process on solar EUV conditions leads to numbers anywhere from 270 to 700 mbar.

1.4.4 Sputtered Escape

When a precipitating energetic particle impacts the Martian atmosphere, energy and momentum are transferred to the atmospheric particles. This is referred to as atmospheric sputtering. If enough energy is transferred, an impacted particle can be brought above escape energy, and because incident particles are often very energetic it is possible for the impact of one incident particle to lead to the escape of many atmospheric particles. As of yet, no observations have provided conclusive evidence of sputtering occurring or driving escape at Mars. However, modeling studies have long predicted that sputtering could be a substantial contributor to atmospheric loss. Solar wind protons were initially suggested as a candidate for sputtering at unmagnetized planets (Watson et al., 1980), but we now know that most of these protons are deflected by electromagnetic forces before reaching the atmosphere. A fraction of solar wind protons do become neutral due to charge-exchange, subsequently impacting the atmosphere (Halekas et al., 015b), but this population is small in comparison to that of O+ pickup ions precipitating from the Oxygen corona. With energies of several keV, these particles are expected to be the dominant source of sputtering escape at Mars. Modeling studies suggest a present-day escape rate due to sputtering on the order of $10^{23}\,\mathrm{s}^{-1}$, significantly lower than that of other loss processes (Luhmann and Kozyra, 1991; Leblanc and Johnson, 2001; Leblanc et al., 2018). However, this escape rate is expected to increase dramatically during periods of more intense solar wind, with some studies suggesting that rates would have been as high as $10^{26} - 10^{27}\,\mathrm{s}^{-1}$ during the extreme conditions of the early solar system (Luhmann et al., 1992; Leblanc and Johnson, 2001; Wang et al., 2015).

Estimates of total escape due to sputtering are typically based on isotope ratios of atmospheric gases. In the upper atmosphere, particle species diffusively separate such that lighter species extend to higher altitudes. As a result, these lighter gases are more likely to be impacted by incoming particles and are more susceptible to sputtering escape. This leaves the atmosphere enriched in heavier elements, and allows us to use the ratios of stable isotopes as a proxy for determining total loss due to sputtering. Photochemical escape can fractionate isotope ratios in a similar manner,

however, making it difficult to determine which loss process has been dominant for some gas species. This makes $^{38}Ar/^{36}Ar$ a particular useful ratio, as argon is chemically inert does not participate in photochemical escape. Using this ratio to model escape backwards in time, Jakosky et al. (2017) determined that 66% of the argon ever present in the Martian atmosphere has been lost due to sputtering. Lighter atmospheric constituents such as oxygen were likely even more susceptible to the effects of sputtering, due both to their lower escape energy and their proportionately higher abundance in the upper atmosphere. This means that if we assume an initial atmosphere of 1 bar, sputtering may have been responsible for greater than 660 mbar of loss.

1.4.5 Impact Erosion

Meteor impacts provide energy and momentum to the Martian atmosphere, ejecting particles at a rate proportional to the size and frequency of impacts. This may have driven significant amounts of loss early in the solar system's history when impacts were more frequent. Using an estimated time history of impactor rates, Brain and Jakosky (1998) found that impact erosion may have removed 50-90% of the original Martian atmosphere. Similar studies by Svetsov (2007) and Pham et al. (2009) reported estimates of atmospheric loss due to impacts ranging from 10 mbar to 800 mbar depending on the timing and intensity of the Late Heavy Bombardment (LHB). However, impacts can also deliver volatiles to the planet, and some studies have shown that numerous small impactors depositing atmospheric gas over time may outweigh any erosion caused by large impactors (De Niem et al., 2012). All of these studies agree that impact erosion only had a significant effect through the end of the LHB, and that for the last 3.5-4 billion years escape rates due impacts have been negligible in comparison to other loss processes. As with hydrodynamic escape, impact erosion is therefore less relevant to the atmospheric escape that has occurred since Mars was last potentially habitable, and is often discounted in such discussions.

1.4.6 Ion Escape

Unlike neutral particles, ions are subject to electromagnetic forces, and they therefore have a separate set of processes by which they can reach escape energy. At a fundamental level, all of these processes involve the acceleration of ions by electric fields, which arise according to the generalized Ohm's law:

$$\mathbf{E} = -\mathbf{v} \times \mathbf{B} + \frac{1}{ne}\mathbf{J} \times \mathbf{B} + \frac{1}{ne}\nabla P_e \ldots \tag{1.1}$$

This describes how the electric field $\mathbf{E}$ is formed due to the interaction of the bulk plasma velocity $\mathbf{v}$, the magnetic field $\mathbf{B}$, the current density $\mathbf{J}$, and the electron pressure gradient ∇P_e, with n and e as the plasma number density and the electron charge. On the right hand side of the equation we find three terms, each of which accounts for a different type of electric field that could be accelerating ions away from Mars.

The term $-\mathbf{v} \times \mathbf{B}$ represents the motional electric field of the solar wind, and is responsible for substantial quantities of escape from the upper ionosphere and exosphere. Here, freshly ionized particles are accelerated to move away from Mars at the solar wind speed, a process referred to as "ion pickup". Upon being picked up, the particles begin to gyrate around the interplanetary magnetic field (IMF) with a gyroradius larger than the radius of Mars (typically 1-10 martian radii). Some of these ions are then accelerated back into Mars (driving sputtering loss, as discussed in the previous section), but numerical simulations have shown that most of them escape the planet in a "plume" of particles that extends outward and around the planet in the direction of the motional electric field (Luhmann, 1990; Fang et al., 2010a). This was recently confirmed by Dong et al. (2015b), who used MAVEN data to show that this plume accounts for $\sim$ 25% of all escaping energetic O+ ions. Model results suggest that ion pickup is responsible for escape rates on the order of 10^{24} s^{-1} (Fang et al., 2008, 2010a).

The term $\frac{1}{ne}\mathbf{J} \times \mathbf{B}$ represents the Hall electric field, and $\frac{1}{ne}\nabla P_e$ the ambipolar electric field. Both of these are able to accelerate ions upward from low altitudes, providing them with enough

energy to escape directly upon reaching the exosphere. Processes of this kind are often referred to by the catch-all term "ion outflow" in the literature, with reference to a variety of different initial acceleration mechanisms (Moore and Horwitz, 2007; Yau et al., 2007; Collinson et al., 2015; Xu et al., 2018b). Discrete aurorae, for example, have been observed at Mars by multiple spacecraft (Bertaux et al., 2005; Leblanc et al., 2008; Deighan et al., 2018) with correlated observations of large electric potentials (Xu et al., 2020a), and the associated heating is expected to drive outflow from the Martian crustal field regions (e.g. Ergun et al., 2006). Indirect measurements of the ambipolar electric field, meanwhile, have found that it creates a potential drop of 1-1.5 V at most locations around the planet (Xu et al., 2018b). While this potential drop is not strong enough to accelerate heavy ions to escape energy, it may still loft them to higher altitudes where they are more easily energized by other mechanisms and eventually escape, as suggested by Ergun et al. (2016). Studies have also shown that wave heating may be responsible for a large fraction of ion loss (Andersson et al., 2010), as might the bulk removal of portions of the Martian ionosphere through instabilities or the detachment of magnetic flux rope structures (Terada et al., 2002; Penz et al., 2004; Brain et al., 2010).

Using spacecraft measurements to distinguish between any of these escape mechanisms, however, is a difficult task. In situ measurements of particle fluxes and electromagnetic fields can provide us with the knowledge of whether ions are likely to escape, but often provide very little information on what brought these ions to their current state. This information is instead frequently gained contextually, or though comparisons to kinetic plasma models. In the end, all ions that escape from mars will eventually by picked up by the solar wind, and in the context of understanding atmospheric escape throughout Martian history, the most important measurement may simply be the total quantity of escaping ions, regardless of acceleration mechanism.

Measurements of this kind have been made numerous times, with the first such estimates dating back to the Soviet missions Mars 2, Mars 3, and Mars 5. Using the *Registrator Intensivnosti Electronov Protonov* (RIEP) instruments aboard these spacecraft, Bogdanov et al. (1975) and Vaisberg et al. (1977) reported total ion escape rates of $10^{25}\,\mathrm{s}^{-1}$. Measurements made fifteen years

later by the Phobos spacecraft resulted in an estimated ion escape rate of $3 \times 10^{25}\,\mathrm{s}^{-1}$ (Lundin et al., 1990), and fifteen years after that studies using Mars Express reported escape rates of roughly $3 \times 10^{24}\,\mathrm{s}^{-1}$ (Lundin et al., 2008; Nilsson et al., 2011; Ramstad et al., 2015). Most recently, results from MAVEN have provided calculated escape rates of $3 \times 10^{24}\,\mathrm{s}^{-1}$ (Brain et al., 2015, only accounting for particles above 25eV) and $3 \times 10^{24}\,\mathrm{s}^{-1}$ (Dong et al., 2015b, only accounting for O+ above 6eV).

We have therefore found, across a range of years and different spacecraft, a quite consistent value of $10^{24} - 10^{25}\,\mathrm{s}^{-1}$ for the total ion escape from Mars. This is at least an order of magnitude lower than the rate of neutral escape, and if taken as a constant value through time would only account for the loss of a few mbar of Martian atmosphere. However, from studies of other stars it is expected that the sun was significantly more active early in the solar system (Ribas et al., 2005; Wood, 2006). With ∼10 times the present-day EUV and X-ray intensity and ∼10-100 times the present-day solar wind pressure, it is expected that ancient Mars would have experienced much higher rates of ionization and much stronger electric fields, leading to significantly higher ion escape. We therefore find it necessary to study the processes driving ion escape today, such that we can understand how they may have varied throughout Martian history and contributed to the loss of the Martian atmosphere. At a fundamental level, these processes are facilitated by Mars's interaction with the solar wind, which is the subject of the next section.

1.5 The Solar Wind Interaction with Mars

As the solar wind flows outward through the solar system, each planetary object that it encounters represents an obstacle of some kind, disrupting the flow and leading to an often complex plasma interaction. Depending on the object's internal magnetic field, atmospheric size, distance from the sun, and surface conductivity, the specifics of this interaction can vary greatly. However, they can be classified into three broad categories that differ mainly in size, structure, and the extent to which the objects are shielded from the solar wind.

For those objects that possess a strong magnetic dynamo (e.g. Earth, Jupiter), the planetary

magnetic field deflects solar wind particles directly via the Lorentz force. As the incoming particle flow is diverted, it exerts a pressure on the outer edges of the magnetosphere, compressing it and stretching it to form a long magnetic tail that extends anti-sunward with the flow direction (see Figure 1.5a). The resulting structure resembles classical pictures of supersonic fluid flow around an obstacle, with the overall size and shape depending upon the strength of the incoming flow. During periods of strong solar wind, a global magnetosphere will shrink, and during periods of weak solar wind it will expand. Under typical solar wind conditions, most solar wind particles are disrupted or deflected tens of planetary radii before reaching the planet, first at a bow shock, where the solar wind is decelerated to subsonic speeds, and then at a magnetopause, where the planetary magnetic field meets the incoming IMF in a pressure balance. As a result, much of the atmosphere at a magnetized planet is completely shielded from solar wind particles. Some regions, however, remain exposed, as magnetic reconnection between the planet's intrinsic field and the IMF creates magnetic field lines that connect directly between the planet and the solar wind. Particles that flow along these field lines are are funnelled into the polar regions of the planet. Here they impact the atmosphere, depositing large amounts of energy and generating aurora as they do.

On the other end of the spectrum of solar-wind interactions lie objects such as the Moon, which possess no intrinsic magnetic field and little to no atmosphere. In an interaction of this kind, solar wind particles impact the planetary surface directly, and as these particles are absorbed a wake region is created (see Figure 1.5b). If the object has a conductive surface or subsurface, the relative motion of the IMF can induce surface currents via Faraday's law. These currents generate a magnetic field that opposes the external field, but the size of this induced field is typically not strong enough to offset the pressure of the incoming solar wind, and is therefore negligible in terms of any shielding it might provide. In general, Moon-like bodies are treated as representing virtually no obstacle to the incoming solar wind, and as being completely exposed to solar wind particles.

Between these two extremes lie the class of solar system objects that have no intrinsic magnetic field, but do possess a substantial atmosphere. In this type of interaction, EUV radiation from the Sun ionizes a substantial portion of the upper atmosphere, creating an electrically conducting

ionosphere. Once again via Faraday's law, currents are induced that oppose the external field, and due to high ionospheric conductivity these currents are generally strong enough to shield the atmosphere below. As the IMF is unable to penetrate into the ionosphere, it piles up in front of the body, resulting in a magnetosphere structure that is similar to that of the intrinsic magnetic field case, but of comparably small size (typically only extending a fraction of a planetary radius past the surface). This type of interaction, illustrated in Figure 1.5c, is often referred to as an "induced magnetosphere". Examples in our solar system include Venus, Titan, and Mars. At these planetary bodies, the solar wind has access to much of the upper atmosphere, but is typically shielded from penetrating deeper. At Mars however, the interaction is more complex, deviating from this standard picture due to the presence of crustal magnetic fields.

1.6 Crustal Magnetic Fields

An unexpected discovery at Mars in recent years was that many regions of the planet's crust are highly magnetized. This was first observed in 1998 by the MGS spacecraft, which found anomalously strong magnetic fields present over small spatial scales during its aerobraking and science phasing orbits (Acuna et al., 1998). It was soon determined that regions of magnetization are scattered across the planet's surface, likely having formed when different parts of the crust cooled and solidified while in the presence of a global magnetic dynamo (Acuna et al., 1999). That global dynamo has long since shut off, but the crustal magnetic fields that remain are still strong enough to dominate their local plasma environment. Spacecraft orbiting at several hundred kilometers altitude find field strengths in excess of 500 nT, ten times stronger than comparable magnetic anomalies at Earth (e.g. Langlais et al., 2010), and the recently deployed InSight lander has reported magnetic fields whose vertical components alone are greater than 1000 nT (Johnson et al., 2020). At these strengths, Martian crustal magnetic fields dwarf those typically found in the interplanetary magnetic field, and are therefore the primary magnetic influence throughout much of the Martian ionosphere.

However, crustal magnetic fields are not spread evenly across the planet. Rather, they are

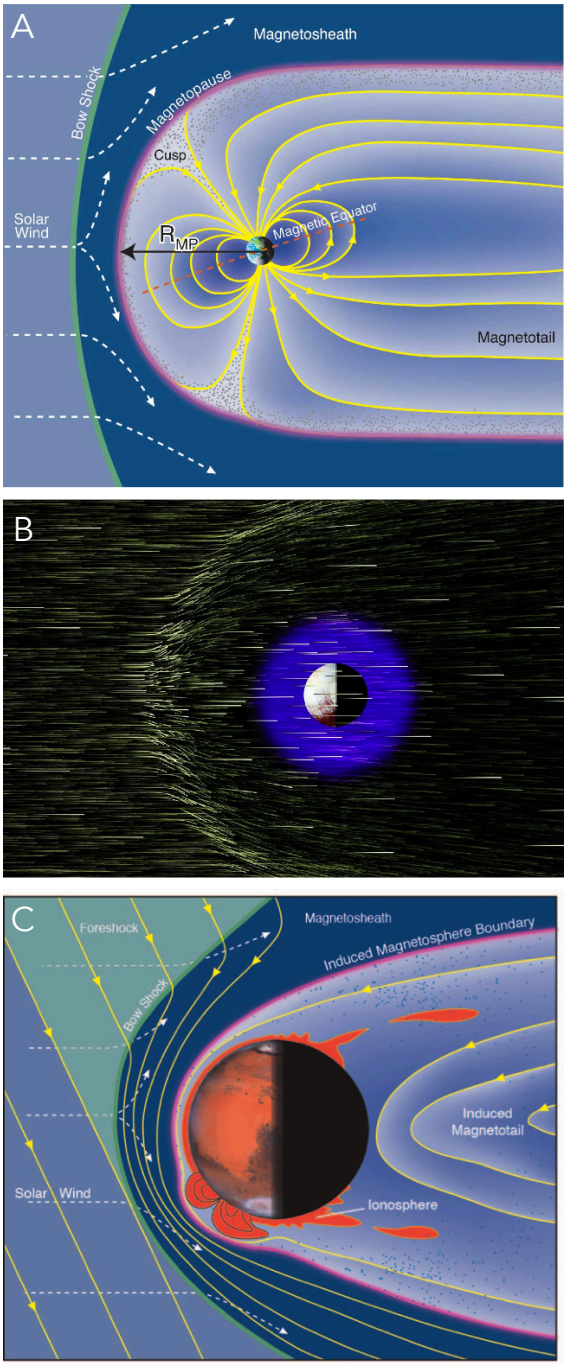

Figure 1.5: Diagrams of solar Wind interactions with planetary bodies, namely:
(A) Earth, a magnetized interaction, Credit: Fran Bagenal and Steve Bartlett
(B) Pluto, a moon-like interaction, from Bagenal et al. (2016); Credit: Steve Bartlett and NASA'S Scientific Visualization Studio
(C) Mars, an induced magnetosphere interaction, from Brain et al. (2017); Credit: Fran Bagenal and Steve Bartlett

clustered together in groupings of varying size, including one particularly large complex of fields that covers much of Mars's southern hemisphere (See Figure 1.6). By comparison, the regions surrounding the Hellas and Argyre basins, as well as most of the northern hemisphere, are relatively unmagnetized. From this we can make a few interesting inferences.

First, the fact that crustal magnetism appears to be most dominant in the ancient, heavily cratered southern hemisphere can give us an estimate of when the global dynamo shut off. Specifically, it appears that the global dynamo was present during the formation of the ancient southern terrain (>4 Gyr ago) but not during the creation of the younger surface features and impacts (∼3.8-4 Gyr ago), meaning that it must have ceased to operate between these two time frames. More sophisticated estimates of the dynamo shutoff timing place it as occurring roughly 4.1 Gyr ago (Lillis et al., 2013; Morschhauser et al., 2018), though there are some that argue that it happened several hundred million years later (e.g. Schubert et al., 2000; Mittelholz et al., 2019). This time period therefore may have represented a significant shift in the evolution of the Martian atmosphere, as the planet transitioned from a global magnetosphere interacting with the solar wind to an induced magnetosphere.

Second, correlation of crustal magnetism with geologic surface features can help us characterize the magnetization in the context of Martian geologic history. Densely packed regions of opposite magnetic polarity suggest that Mars's former dynamo likely underwent regular pole reversals (Arkani-Hamed, 2001), as we observe at Earth and the Sun, and theorize should occur at Jupiter and Saturn (Hathaway and Dessler, 1986). The magnetic polarity present at any point in time was then captured by any portions of the crust experiencing melting events, creating crustal field contours that map along fault lines, around impact basins, and around the edges of regions of volcanic activity. Connerney et al. (2005) have even suggested that the magnetic lineations observed in the southern hemisphere could be indicative of plate tectonics on ancient Mars, with crustal spreading analogous to the seafloor of Earth, though this result has been debated (Breuer and Spohn, 2003).

Third, and of most relevance to this thesis, the nonuniform distribution of crustal magnetic

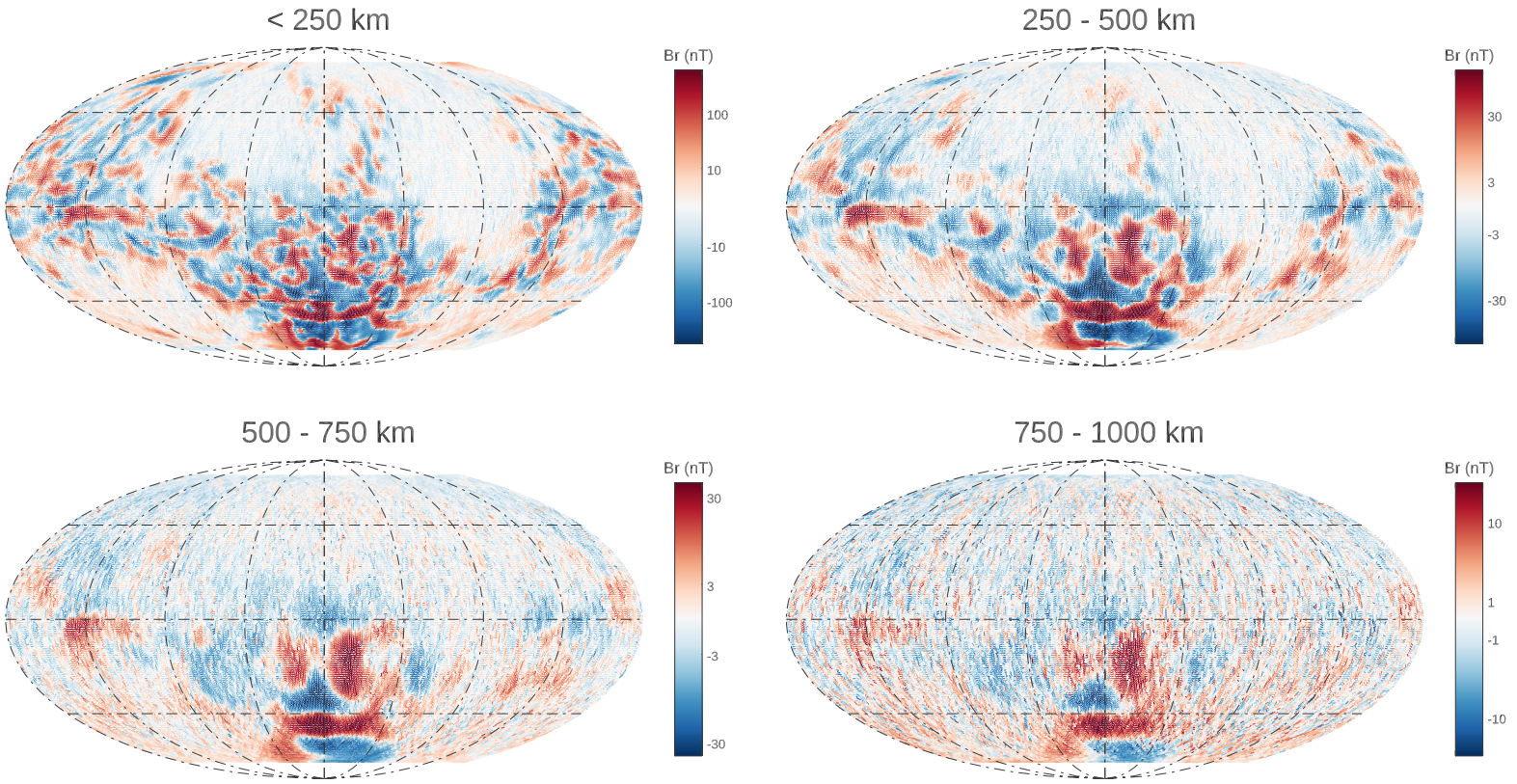

Figure 1.6: Maps of the Martian crustal magnetic fields at four different altitude ranges. For each 1° lat × 1° lon bin, the median magnetic field measured by MAVEN over 5 years of observations is represented by a whisker. Radial magnetic field strength is encoded in the whisker color, and the horizontal direction of the magnetic field is encoded in the whisker direction. Note that the color scales differ for each altitude range, so as to accentuate morphology rather than absolute magnitude.

fields means that at any given time, different regions of the planet are likely subject to very different magnetic field environments. The resulting situation is one unlike any of the typical solar wind interactions discussed in the previous section. Rather than an atmosphere that is shielded from the solar wind or one that is exposed, Mars represents a hybrid of the two situations. In some areas, crustal field structures provide shielding analogous to that of a global dipole, with horizontal fields deflecting low energy particles from the solar wind. Where these structures reconnect with the solar wind, they create "cusps" of vertically oriented fields that may behave similarly to the polar inflow regions we observe at magnetized planets, channeling energy into localized pockets (see Figure 1.7. And in the unmagnetized regions of Mars, the solar wind interacts directly with the top of the conducting ionosphere, creating a more typical induced magnetosphere. To complicate matters further, the way any particular location on Mars interacts with the solar wind varies greatly as it rotates between the dayside and the nightside, as well as with changes in the incoming solar wind conditions. Crustal fields that are just strong enough to stand off the solar wind during typical conditions may be completely overpowered during periods of increased solar wind pressure.

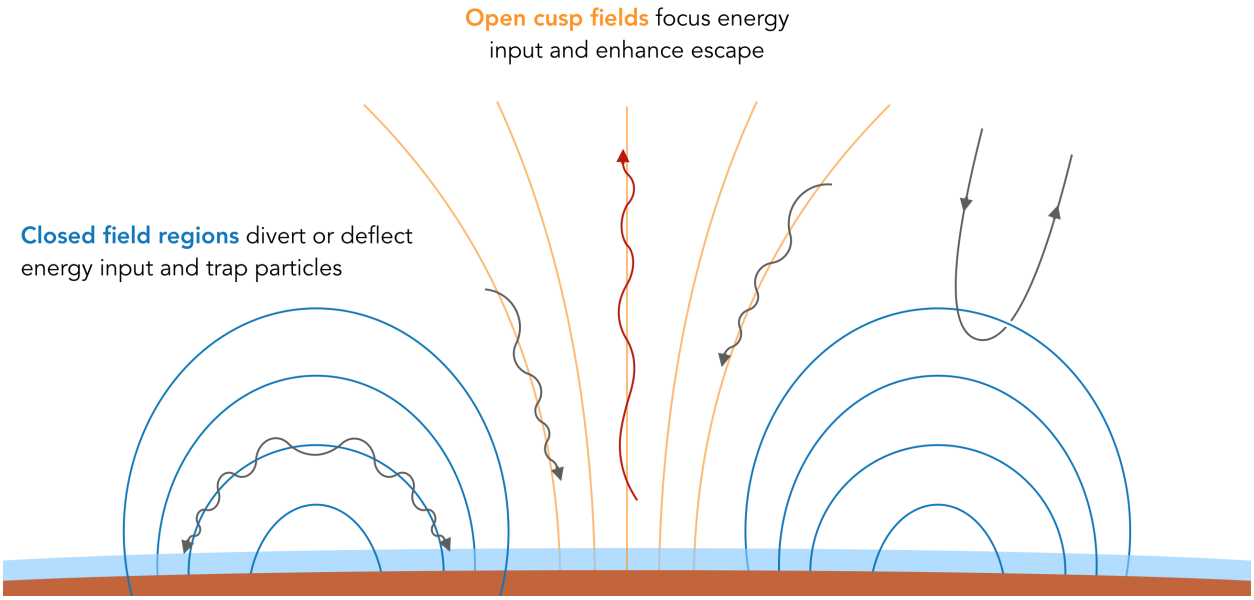

Figure 1.7: Illustration of Martian crustal field cusps

The overall influence that this complex system has on atmospheric escape is not immediately

clear. The presence of magnetic shielding on a local scale would seem to inhibit escape to some degree, but the prevalence of energized cusp regions could do just as much to funnel enhanced escape through these channels. Alternatively, it could be just as possible that the effects of the crustal magnetic fields are negligible when compared to the other sources of atmospheric escape at Mars, particularly when considering the planet's relatively weak gravitational pull (as discussed in section 1.4). In any case, an analysis of how the crustal fields affect atmospheric escape should be illuminating, both in constraining the evolution of Mars and in understanding how planetary magnetic fields affect atmospheric escape on a broader scale. Such an analysis is the ultimate goal of the work behind this thesis.

At its core, a work of this kind represents a study of how ion escape varies between the magnetized and unmagnetized regions of Mars. This requires us to understand not just the flows of ions but also the structure of magnetic fields that facilitate these flows. In other words, to study the difference in ion escape between areas that are magnetically shielded or exposed, we must first have a way of distinguishing between these two situations. We therefore find ourselves interested in a technique to determine when and where magnetic fields are connected to the planet or to the solar wind. This area of study is that of magnetic topology, the subject of the next section.

1.7 Magnetic Topology

At its core, topology is the branch of mathematics that studies how to classify objects by their underlying form, rather than by the specifics of their exact shape (e.g. a circle, a square, and a triangle are each made of just one loop, despite their differing amounts of pointy bits). It is the process of distilling complex problems down to their most essential properties, and then analyzing where these properties exist and where they do not. This form of analysis is broadly applicable, with use in graph theory, DNA sequencing, and quantum mechanics, to name a few.

Magnetic topology is no different. In this case, the property we are interested in is the endpoint connections of magnetic field lines. While charged particles moving across magnetic field lines are deflected by the lorentz force, those moving along the field are unimpeded, meaning that

studying the magnetic endpoints often allows us to determine to what areas a charged particle population has direct access. And in the case of a solar wind interaction with a planetary obstacle, any field line's endpoints can only be connected to either the IMF or to the planet's magnetic field. Therefore, regardless of any specific path a field line may traverse, there are only three magnetic topologies for us to consider: (1) Closed, in which a field line is connected on both ends to the planet, (2) Open, in which a field line is connected to both the planet and the IMF, and (3) Draped (or unconnected), in which a field line is connected on both ends to the IMF (see Figure 1.8).

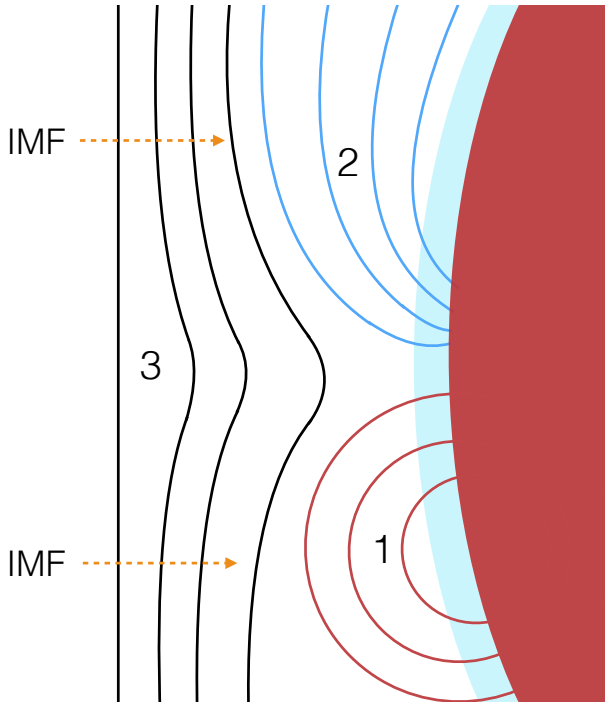

Figure 1.8: Illustration of possible Martian magnetic field topologies, these being (1) closed, (2) open, and (3) draped.

This focus allows us to determine at a broad level what locations are magnetically linked such that charged particles can move between them. However, it is important to note at this point that magnetic field lines are a mathematical construct, real only in the sense that they represent information about the underlying field and its effects on particles. When we say that a magnetic field line links two locations, we are making a statement only about the present instant, and about the path that a massless charged particle would follow. No physical particle will ever follow the

path of a field line precisely, and the extent to which it deviates from this path depends upon a multitude of factors, including the particle's energy and mass, the strength of the magnetic field, and the rate at which the field is changing. While this is a somewhat pedantic distinction, it will become increasingly important as we apply our study of magnetic topology to ion escape at Mars. Field lines that are closed for electrons might still allow heavier ions to escape, and particles gyrating around one field line will frequently drift onto other lines that may not share the same topology.

Still, the formalization of magnetic topology is a very useful one, and under many circumstances particles follow magnetic field lines quite closely (such as in the compelling visualizations that nature provides us with loops in the solar corona, or aurora in the night sky). Provided that we understand the caveats associated with labeling the magnetic field as being "closed" or "open", we can use these distinctions to characterize magnetic shielding at Mars.

1.7.1 Methods of Studying Magnetic Topology

However, analyzing magnetic topology using spacecraft measurements can be a difficult task. While computer simulations provide the ability to trace an entire field-line for a snapshot in time, in-situ magnetometer measurements provide us only with a local magnetic field vector, giving no information on how that magnetic field behaves far from the spacecraft. To identify magnetic topology we therefore have to make inferences using additional information. Some of this information can be gained contextually, using the strength and direction of the magnetic field. Strong fields directed radially outward near the surface of Mars, for example, are likely to be crustally sourced, while those far from the planet are more likely to be connected to the solar wind. For a more robust calculation, however, studies typically combine magnetic field measurements with those of charged particle fluxes. In general, the primary goal of these studies is to trace particle flows backwards to where they originated. While we are unable to directly measure the magnetic field far from the spacecraft, we know that charged particles reaching the spacecraft have traveled along the magnetic field already, and by studying these particles in detail we can determine (1) where they came from

and (2) what sorts of magnetic fields they encountered along the way.

Analysis of this kind was first used in studies of the interaction between Earth's magnetosphere and the IMF, particularly in the context of early efforts to understand magnetic reconnection. Since then, several different methods have been used to infer magnetic topology in the magnetospheres of Mercury (Gershman et al., 2015), Venus (Zhang et al., 2012), Mars (Brain et al., 2007; Xu et al., 2017a; Weber et al., 2017), Jupiter (Goertz et al., 1976; Connerney et al., 2001), Saturn (Acuna et al., 1981; Smith et al., 2016), and in the solar wind (Kahler and Hundhausen, 1992). Here we explore two such techniques.

One technique for identifying magnetic topology involves distinguishing between source populations of electrons. By identifying the characteristic energy signatures of electrons that are sourced from the solar wind, a planetary magnetosphere, or a planetary atmosphere, this method allows you to determine to which of those locations the spacecraft-measured magnetic field is magnetically linked. If we see, for example, electrons carrying solar wind energy signatures flowing in from one direction, and electrons carrying ionospheric energy signatures flowing in from the opposite direction, we can deduce that the magnetic field we are measuring is connected to both the planet and the solar wind, and is therefore topologically open. Similar determinations can be made for other topologies, though the characteristic energy signatures of interest will vary by planetary body based on atmospheric constituents. At Mars, the abundant photoionization of CO_2 produces a series of distinctive signatures in ionospheric electron energy spectra, including a series of sharp peaks between 22 and 27 eV, a steep decrease in flux between 60 and 70 eV (sometimes called the "photoelectron knee"), and another steep drop just past 500 eV (Frahm et al., 2006b; Xu et al., 2017a; Peterson et al., 2016). An spectrum of this kind measured by MAVEN is shown in red in Figure 1.9, alongside measured spectra of the solar wind (blue), magnetosheath (green), and magnetotail (black). As seen in this figure, solar wind energy spectra tend to feature higher fluxes overall, with a steady decrease in flux from low energy to high energy. This makes it very possible (though not always easy) to distinguish between the solar wind and the Martian ionosphere (e.g. Mitchell et al., 2001, 2016). Similar methods have been used to study magnetic topology at Earth,

often in analyzing crossings of the magnetopause and the topological changes that take place during magnetic reconnection events (Fuselier et al., 2012).

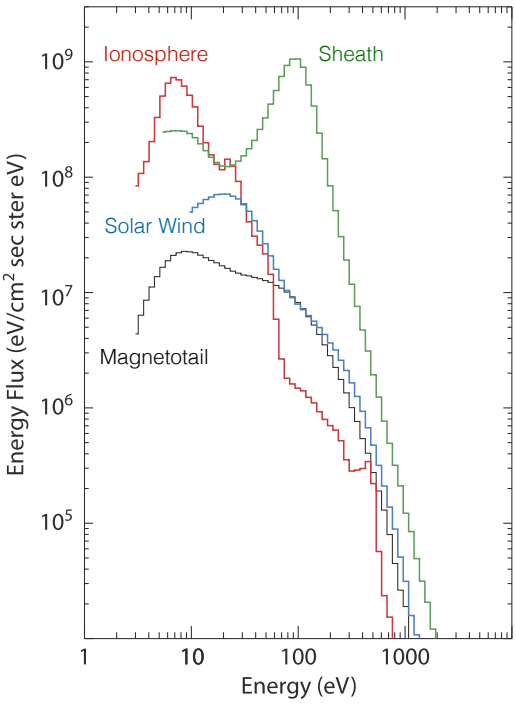

Figure 1.9: Characteristic electron energy spectra at Mars, adapted from Mitchell et al. (2016).

Another common technique for identifying topology studies the flow directions of electrons to determine how these flows have been modified in the process of reaching the spacecraft. Most commonly this involves the study of Electron pitch angle distributions (PADs), which describe the flow of electrons relative to the local magnetic field. These can be used to determine whether the measured magnetic field is connected to a location where electrons are being magnetically reflected or lost due to collisions. The presence of loss cones, for example, can be taken to indicate that some particles are being mirrored while others are absorbed by the atmosphere (See Figure 1.10a). If we see that loss cones of this sort in both the electron flux traveling parallel to the magnetic field and the flux traveling antiparallel to field (Figure 1.10b), we can conclude that the magnetic field is connected to the atmosphere in both directions, and is therefore topologically closed. If we

see a loss cone in only one direction, however, this may tell us that the field is topologically open. Furthermore, the shape of a loss cone can provide information on the strength of the magnetic field where the particles are mirrored, the atmospheric density where the particles are lost, and any parallel electric fields the particles encountered along their trajectory (Lillis et al., 2008). A more complete explanation of this technique will be presented in Chapter 2, wherein we use pitch angle distributions to map magnetic topology on the Martian nightside. Methods similar to this have been used to study magnetic topology at Earth (Mitchell et al., 1987), Mars (Brain et al., 2007), Jupiter (Zhang et al., 2017), Ganymede (Frank et al., 1997; Williams et al., 1997), and the IMF (Kahler et al., 1996).

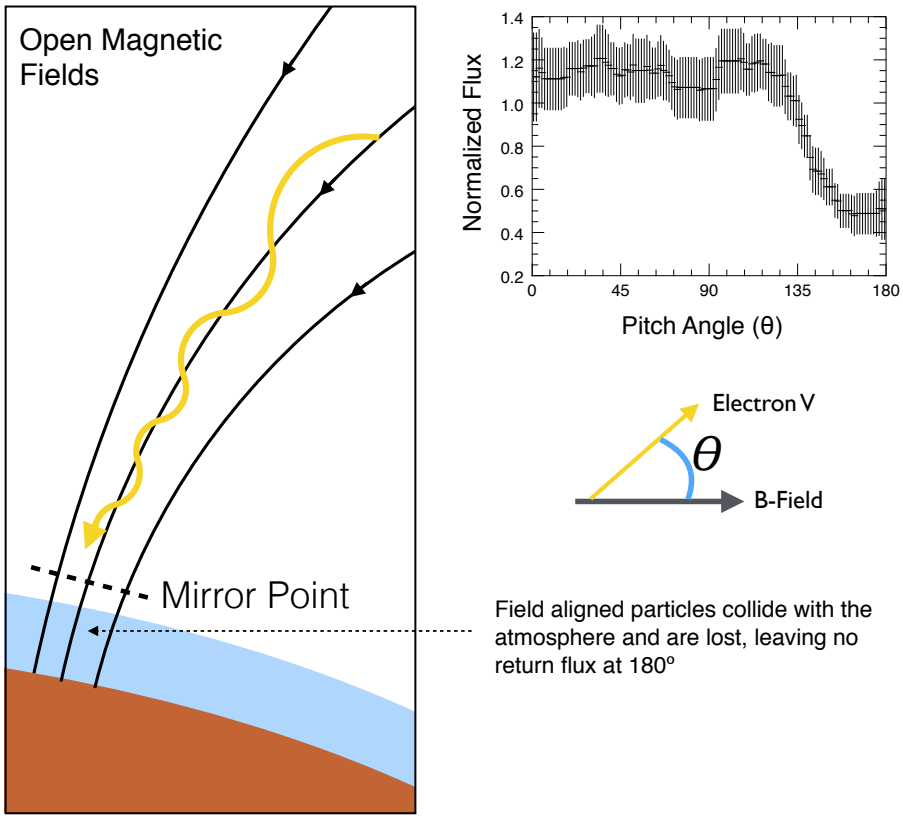

Figure 1.10: Example electron pitch-angle distribution indicating open field topology at Mars.

In this thesis I will use both of the above methods. Each has its own strengths and weaknesses, and each can excel in the correct context, but to make a truly robust system for understanding

magnetic topology we find that it is necessary to use the information gained from both techniques. This is due in large part to the complexity of Mars' solar wind interaction, as has been shown in many previous studies of magnetic topology at Mars. These studies are discussed next.

1.7.2 Studies of Magnetic Topology at Mars

The magnetic field environment of Mars has been an active area of interest since spacecraft first arrived at the planet (e.g. Dolginov et al., 1976; Vaisberg and Smirnov, 1986; Dubinin et al., 1994), but became particularly noteworthy during the MGS mission and the associated discovery of crustal magnetic fields. Informed by the new MGS data, a wide variety of modeling groups performed simulations of the Martian magnetosphere using MHD (Ma et al., 2002; Liemohn et al., 2007b; Terada et al., 2009), Hall-MHD (Harnett and Winglee, 2007), and hybrid (Kallio et al., 2006; Modolo et al., 2006; Brecht and Ledvina, 2007) modeling approaches. Several such studies focused specifically on magnetospheric structure and magnetic topology (Ma et al., 2002; Harnett and Winglee, 2003; Kallio et al., 2006; Liemohn et al., 2007a), together forming a picture of a magnetosphere that is both highly irregular (due to the interaction of the crustal fields with the IMF) and highly dynamic (due to how this interaction varies with solar wind conditions and the rotation of crustal magnetic field sources).

During this same time, there were also several studies of magnetic topology performed using spacecraft data. Mitchell et al. (2001) used electron energy distributions to distinguish between closed and open fields on the Martian nightside, as well as to separate measurements of ionospheric plasma from those of shocked magnetosheath plasma. Krymskii et al. (2002) compared magnetic field measurements to a simplified dipole model of a crustal field source to infer magnetic topology in the strongest crustal field regions. Brain et al. (2007) used pitch-angle distributions measured by MGS to make global maps of magnetic topology (this study is discussed more in Chapter 2, as it inspiration for much of the initial work done in this thesis). And a few studies used radar soundings from *Mars Express* to indirectly study effects of local magnetic topology on the Martian ionosphere (Gurnett et al., 2005; Nielsen et al., 2007).

Since the arrival of MAVEN at Mars, our ability to study magnetic topology at the planet has increased greatly. With the increased availability of magnetic field and plasma measurements across a range of altitudes, geographic locations, and solar local times, a series of data and modeling studies have been performed. New studies using global MHD simulations of Mars have investigated a range of topics including global ion escape (e.g. Ma et al., 2015; Dong et al., 2015b), space weather effects (Dong et al., 2015a; Luhmann et al., 2017; Ma et al., 2017), the rotation of the planet's crustal fields (Ma et al., 2014; Fang et al., 2015), and the effects of upstream drivers (e.g. Ma et al., 2014). Hybrid simulations have meanwhile been used to address similar problems at spatial scales where particle kinetics become necessary, including studies of global ion escape (Kallio and Barabash, 2012; Brecht et al., 2016; Jarvinen et al., 2016, 2018), the structure of the interaction with the solar wind (Holmstrom and Wang, 2015; Modolo et al., 2016), the effects of crustal magnetic fields (Brecht and Ledvina, 2014), or the effects of a weak dipole field at Mars-like planets (Egan et al., 2019; Sakata et al., 2020).

In all of these studies, magnetic topology plays an important role in shaping particle dynamics, and in many cases it is calculated explicitly (e.g. Luhmann et al., 2017; Ma et al., 2017) or is even a primary focus of the work (Ulusen et al., 2016; Xu et al., 2018c).

The wide coverage of MAVEN data has now also allowed for direct analysis of topology across the entire parameter space. This has included studies presenting geographic maps of topology (Xu et al., 2017a; Weber et al., 2017; Xu et al., 2019), topology of the martian magnetotail (DiBraccio et al., 2018), variations in topology due to solar wind drivers (Xu et al., 2018a; Weber et al., 2019; Xu et al., 2020b), case studies of reconnection at Mars (Harada et al., 2015, 2018), and the impacts of topology on ionospheric processes (Adams et al., 2018; Fowler et al., 2019).

As a result of these studies, we now have a significantly improved (though still incomplete) understanding of magnetic topology of Mars. This is presented in the following sections of this thesis. Focusing primarily on crustal magnetic field regions, this thesis aims to characterize magnetic topology and use it to interpret measurements of ion outflow from Mars. First, we describe the techniques we use to analyze magnetic topology. Second, we study the typical structure of crustal

field topology. Third, we identify how this structure varies under different conditions. And finally, we use the previous works to interpret how crustal magnetic fields at Mars influence atmospheric escape from the planet.

Chapter 2

Characterizing magnetic topology at Mars

This chapter was originally published as "Characterization of low-altitude nightside martian magnetic topology using electron pitch angle distributions" (Weber et al., 2017). It has been adapted here to fit within the narrative flow of the thesis.

Abstract: Magnetic field lines at Mars act as direct pathways for both energy inflow and ion escape. Local variations in magnetic field topology can therefore directly impact the interaction between the solar wind and the Martian ionosphere. One method of analyzing magnetic topology is through the use of electron pitch angle distributions (PADs). Previous PAD investigations have characterized magnetic topology in the Martian system using data from the Mars Global Surveyor (MGS) spacecraft, but these studies were orbitally constrained to ∼400km altitude and 2 AM/2 PM local time. With the Mars Atmosphere and Volatile Evolution (MAVEN) mission, we are now able to extend this analysis to a larger range of altitudes and local times. Here we use electron PADs measured using the Solar Wind Electrostatic Analyzer (SWEA) and Magnetometer (MAG) instruments on MAVEN to analyze the magnetic topology of the nightside Martian environment. We use several characteristic PAD shapes to determine where Martian magnetic field lines are open or closed to the solar wind, and present frequency maps of how these PAD shapes vary both geographically and with altitude. Finally, we present an initial analysis of the variation of the PAD shapes with local time, finding that trapped electron distributions become increasingly frequent as crustal fields rotate from dusk to dawn across the nightside of Mars.

2.1 Introduction

Because Mars lacks a global dynamo, the interplanetary magnetic field (IMF) carried by the solar wind is able to directly interact with the planet's ionosphere. As the IMF drapes around the planet, it forms an induced magnetosphere similar to those of other unmagnetized bodes in the solar system. The Martian system is uniquely complex, though, due to the presence of crustal magnetic fields. Scattered in clusters across the planet's surface are pockets of crustal magnetism, remnant from when the planet possessed a global magnetic field (Acuna et al., 1999). As the IMF encounters Mars, it interacts with these crustal magnetic fields to produce an intricate topological system. In some areas, the crustal magnetic field lines reconnect with the IMF to produce lines of connectivity between the planet and the solar wind, while in other areas they are unaffected and act as small-scale magnetic shields. Because of this, energetic inputs from the solar wind (such as auroral heating) can often be restricted to localized regions of the Martian atmosphere. This in turn means that variations in magnetic topology can affect particle escape, and over time may have influenced the planet's evolution.

The energization and outflow of charged particles at Mars is inherently dependent on the magnetic field environment. Low energy ions and electrons will travel along magnetic field lines much more readily than across them, meaning that the local magnetic field acts as a direct determinant of the path of ionspheric particles. Atmospheric ion outflow can therefore be locally suppressed or enhanced depending on where magnetic fields are providing an avenue of escape. Ergun et al. (2016) demonstrated that high electron temperatures observed in the ionosphere could cause significant fluxes of ambipolar ion escape, and that this escape is enhanced by nearly an order of magnitude in regions of vertical open field topology. Just as importantly, the deposition of solar wind energy into the Martian atmosphere is also guided by magnetic fields. On the nightside of Mars, superthermal electron flux acts as a dominant source of energy input (Fox et al., 1993). These electrons precipitate into the Martian atmosphere along the IMF and impart their energy as they collide with the atmosphere, ionizing and heating particles (Lillis et al., 2009; Leblanc et al.,

2008). The previously mentioned crustal magnetic fields add an extra layer of complexity. First discovered and mapped by Mars Global Surveyor (MGS), these magnetic fields have since been shown to frequently reconnect with the IMF as well as periodically form detached magnetic loops that flow away from Mars (Eastwood et al., 2008; Brain et al., 2010). Because magnetic field lines at Mars can serve as direct paths for both energy inflow and particle escape, it is important to characterize where and under what conditions magnetic fields do or do not connect to the IMF.

Magnetic fields at Mars are typically considered to have three possible field topologies: (1) closed, where the field line is connected at both ends to Mars, (2) open, where the field line is connected to Mars at one end and to the IMF at the other, or (3) unconnected (or "draped"), where the field line is solely connected to the IMF (Nagy et al., 2004; Bertucci et al., 2003; Brain et al., 2007). Figure 1.8 illustrates these possible configurations, labeled as 1, 2, and 3 respectively. In this study we are most interested in solar wind interactions with the Martian atmosphere, so here we define closed and open field lines through their connection to the atmosphere rather than to the planet's surface. For the same reason, we also do not analyze draped field lines within this study.

Distinguishing between these configurations, however, can prove difficult. Spacecraft measurements of magnetic field provide only a local magnetic field vector, giving no information on how that magnetic field behaves far from the spacecraft. For this reason, determination of magnetic topology requires the use of particle data in addition to magnetic field measurements. One such method is the use of electron energy spectra to determine the source of a measured electron population. Ionospheric and solar wind plasma each carry a characteristic electron energy signature, and the identification of these signatures can reveal the regions to which a magnetic field line is connected. This method has been used previously to identify high-altitude open field lines carrying atmospheric particles out into the Martian magnetotail (Frahm et al., 2006b) as well as open fields connected to crustal structures allowing the entrance of high energy solar wind electrons (Mitchell et al., 2001; Dubinin et al., 008b). This method is also used to map magnetic topology in a recent study by Xu et al. (2017a), the results of which will be discussed more in later sections.

A separate method of identifying magnetic field topology involves the use of electron pitch angle distributions (PADs) to determine the ways in which directional electron flux has been altered along a measured field line (this method is detailed in Section 2). Pitch angle distributions are frequently used to analyze the topology of the IMF as it flows through the solar system (e.g. Larson et al., 1997; Gosling et al., 2001), and were previously used to study magnetic topology at Mars by Brain et al. (2007). That study used electron PADs calculated by MGS to create a series of maps describing variations in magnetic topology across the surface of Mars. From these maps, it was determined that the strong crustal field complexes in the southern hemisphere are dominated by closed field topology everywhere except for small cusps located between the crustal loops, and that the weakly magnetized northern hemisphere of Mars is dominated by open and draped topologies. However, the analyses presented in this study were limited in several important ways. First, the orbit of MGS only allowed for sampling at 2 AM and 2 PM local time. The rotation of the planet still allowed for complete coverage of the Martian surface and crustal fields, but field lines are likely to transition between open and closed as they move through different local times, a feature that MGS was unable to study. Second, the analysis was only performed for data in a narrow range of altitudes centered on 400km. This provides a consistent baseline to work with, but an accurate description of Martian topology requires analysis across many altitudes. Draped field lines located at 400 km might rest directly above open or closed field lines (as in Figure 1.8), information that would be missed by MGS.

In the study presented here we use MAVEN data to address these limitations, expanding upon the work of Brain et al. (2007). We use data from across the Martian nightside to analyze geographic distributions of magnetic topology, and we present a first analysis of how pitch angle distributions vary with local time on the nightside of Mars. While the nightside environment can be characterized quite accurately through the use of pitch angle distributions, dayside analysis is made complicated by the presence of active photoelectron production. This can often isotropize PADs, drowning out many topological PAD signatures. Characterization of dayside topology using PADs is therefore left to a more dedicated future study. Additionally, the dayside regime is where

the electron energy spectra method of Xu et al. (2017a) is most accurate, and in future works these two methods will be combined to create a full analysis of Martian magnetic topology.

In section 2 of this study we present descriptions of the data products used and our method of processing PAD distributions. In section 3 we describe how PADs are used to infer magnetic topology. In section 4 we present a case study illustrating our interpretation of PAD signatures. In section 5 we compare overall PAD statistics to those reported by the MGS spacecraft. In section 6 we present maps of how these PAD shapes vary geographically and with altitude. In section 7, we present an initial analysis of local time variations across the nightside of Mars. In section 8, we summarize these results and suggest areas of future study that would improve our understanding of the Martian magnetic environment.

2.2 Description of Instrument and PAD Shapes

The primary data product used in this study is that of electron pitch angle distributions measured using the Solar Wind Electron Analyzer (SWEA) and Magnetometer (MAG) instruments on MAVEN (Connerney et al., 2015; Mitchell et al., 2016). SWEA is a hemispheric electrostatic analyzer designed to measure both solar wind electrons and ionospheric photoelectrons at Mars across a series of energies spanning 3 eV to 4.6 keV. The instrument field of view covers 360° in azimuth with 22.5° resolution and 120° in elevation with 20° resolution. The electron energy flux distributions measured by SWEA are paired with magnetic field vectors measured by the Magnetometer (MAG) to produce a PAD every 2 seconds. Due to the large instrument field of view, SWEA generally samples a wide range of angles relative to the magnetic field direction. This means that the resulting PADs generally are able to cover the complete range of pitch angles, from 0° (parallel to the magnetic field) to 180° (anti-parallel). When the magnetic field direction is close to SWEA's axis of symmetry, the PAD range is narrower (a minimum range of 120° resulting when the magnetic field points directly along this axis). The data used in this study were collected between 10 October 2014 and 24 March 2017, spanning slightly over one Martian year. Over this time, MAVEN's orbit continually precessed, with its periapsis location progressing across the dawn,

dusk, day, and night sides. Though MAVEN's elliptical orbit samples altitudes up to ∼6000 km, in this study we are primarily interested in magnetic topology near the ionosphere and so only consider data taken below 500 km. Additionally, this study is restricted to the nightside of mars, only using data taken within the geometric shadow of the planet.

The general method used in this study is to determine the topology of the magnetic fields observed by MAG through analysis of the PAD signatures measured by SWEA. To accomplish this, 800,000 PADs were analyzed and labeled as corresponding to distinct PAD shapes. Here we use PADs measured for 100-300 eV electrons. This energy range is chosen both because it effectively targets the shocked incoming solar wind particles that are expected to dominate the nightside, and because it is directly comparable to the 115 eV PADs used by Brain et al. (2007). In order to increase the counting statistics of our electron fluxes, groups of four consecutive PADs were co-added. For each measured angle, the electron energy fluxes of these four PADs were summed, and their corresponding errors were propagated. Groups of four were chosen so as to give reasonably large flux counts without decreasing the spatial resolution too drastically. We found that co-adding in this way allowed for the most robust identification of PAD shapes, and we verified that the results do not change appreciably when using individual PADs or groups of two instead. In these cases, the statistical trends presented in this paper remained the same, with observation frequencies changing by only 5-10 percentage points. Co-adding in this way produced 200,000 co-added PADs, each corresponding to eight seconds of measurement. Every distribution was then separated into a downward component and an upward component using the measured direction of the magnetic field. These components were labeled individually according to the relative fluxes of electrons traveling parallel and perpendicular to the magnetic field, as compared to the error (σ) associated with the measured electron flux. The four possible classifications are:

(1) Parallel flux is 2σ greater than perpendicular flux ("Field-Aligned Beam')

(2) Parallel flux is 2σ lower than perpendicular flux ("Loss Cone")

(3) Parallel flux and perpendicular flux are within 2σ ("Isotropic")

(4) Parallel and perpendicular flux are within 2σ but flux at intermediate pitch angles (40° - 50°) is 2σ greater than perpendicular flux ("Conic")

Combining a PAD's four possible upward and four possible downward signatures results in 16 possible unique PAD signatures, a selection of which are shown in figure 2.1. One final signature is the "electron depletion" (figure 2.1f), in which the electron flux is within 2σ of zero in all directions. This signature represents a large depletion in superthermal electron flux, the implications of which are discussed later. Out of the 200,000 PADs, ∼10,000 were excluded due to having either no usable data below 20° pitch angle or no usable data above 160° pitch angle. When this occurs it is usually due to the spacecraft blocking a large section of SWEA's field of view. For the rest of the PADs, a successful match was found to one of our PAD signatures. In the following sections, we discuss the interpretation of these different PADs, first describing how PAD shapes are used to infer magnetic topology and then providing a case study to illustrate these inferences.

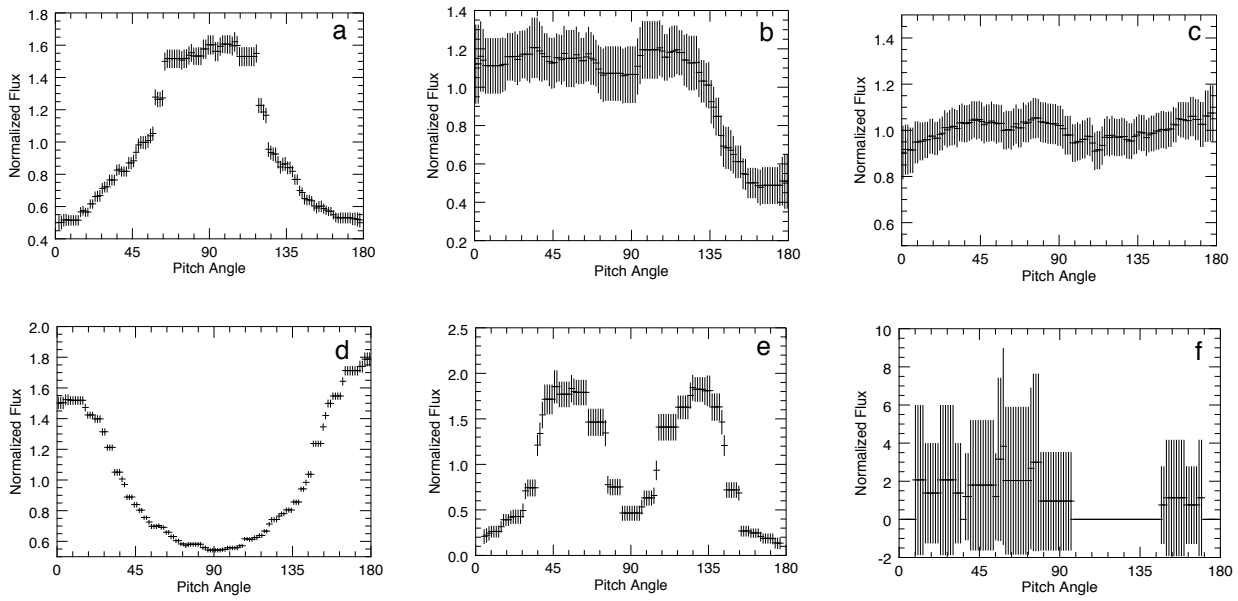

Figure 2.1: A selection of PAD signatures that are observed by SWEA. In order: (a) two-sided loss cone, (b) one-sided loss cone, (c) fully isotropic, (d) double field-aligned beam, (e) conic, and (f) electron depletion. The vertical lines represent 2σ error bars as calculated from the measured electron fluxes using Poisson statistics. Each PAD shown here is normalized such that the average flux is equal to 1

2.3 Interpretation of Pitch Angle Distributions

Open field lines (labeled "2" in Figure 1.8) are those that are connected both to the Martian atmosphere and the IMF. These lines provide a region of interaction between solar wind particles and the ionosphere, and it is through this interaction that we are able to easily identify the open lines with PADs. As electrons travel downward toward Mars along an open field line, they encounter stronger magnetic fields as the field lines converge. Through conservation of the first adiabatic invariant, these electrons eventually mirror, reflecting back upwards once the magnetic field strength becomes sufficiently large. However, the location of this mirror point varies based on electron pitch angle. Particles moving more directly along the field line are able to travel further down into the martian atmosphere before mirroring, and in doing so are more likely to be absorbed by the collisonal atmosphere and lost. This results in a PAD depleted in upward returning field-aligned flux, otherwise known as a one-sided loss cone (figure 2.1b). To identify open field lines, we therefore search for PADs in which the downward flux is either isotropic or field-aligned and the upward flux contains a loss cone. Example observations of these loss cones are shown in the case study that is presented in the next section. One-sided loss cones have been studied previously at Mars for the purposes of mapping the Martian crustal fields (Mitchell et al., 2007), inferring magnetic topology (Brain et al., 2007), and estimating neutral atmosphere densities (Lillis et al., 2005).

Closed magnetic field lines (labeled "1" in Figure 1.8) are loops of magnetic field connected to the Martian atmosphere at both ends ("footpoints"). Depending on whether these footpoints are located on the dayside or nightside of Mars, closed loops can exhibit a variety of PAD signatures. In this study we only consider the signatures that are produced when both footpoints are located on the nightside of the planet: electron depletions (Figure 2.1f) and two-sided loss cones (Figure 2.1a).

Electron depletions are large reductions in superthermal electron flux on the nightside of Mars that were first observed by MGS and have since been investigated by several authors (Mitchell et al., 2001; Dubinin et al., 008b; Lillis and Brain, 2013; Steckiewicz et al., 2015; Shane et al., 2016). These

depletions are due to the presence of closed loops of magnetic field that have lost their associated electron population through recombination with the atmosphere. While on the dayside of Mars, these loops are fill with plasma due to the presence of significant photoionization, but after rotating to the nightside this electron source process is lost, and the loss process of atmospheric absorption dominates. Because electron depletions are robust trackers of closed field lines, we identify them in the PAD analysis presented here, defining depletions as those PADs that have flux rates that are statistically zero across all pitch angles.

Two sided loss cones (also referred to as trapped distributions) result from electrons adiabatically mirroring between regions of increased magnetic field strength. As electrons travel along closed magnetic field loops and move to lower altitudes, they encounter stronger magnetic fields and are reflected back upwards in the same manner as on open field lines. But unlike on open field lines, these particles then travel along the loop to the other footpoint and reflect once more, creating a population of trapped, mirroring electrons. As discussed previously, particles moving more directly along the field (i.e. pitch angles near 0° or 180°) travel lower in altitude before mirroring and thus are more likely to be lost. This leads to a PAD that exhibits a loss cone in both the parallel and antiparallel direction. Two-sided loss cones have been extensively studied for particles trapped within the Earth's magnetosphere (Lyons et al., 1972; West et al., 1973; Abel and Thorne, 1998), and have previously been used at Mars to infer closed field topology (Brain et al., 2007; Lillis et al., 2009) as well as to estimate low altitude magnetic field strength (Mitchell et al., 2007; Lillis et al., 2008).

It is important to note here that cross-terminator closed field lines, containing one footpoint on the dayside and one footpoint on the nightside, can often be mistaken for open field lines with the analysis method used in this study. As photoelectrons from the dayside travel to the nightside, they can be mirrored or absorbed, producing the same one-sided loss cone signature as open field lines. This photoelectron signal is often too weak in the 100-300 eV energy range to affect our analysis, but it is still a source of error (particularly near the terminator) that should be recognized throughout this study.

2.4 Case Study

Figure 2.2 contains data taken during an inbound pass deep on the nightside of Mars, throughout which a variety of PAD signatures are observed. This orbit reaches periapsis at an altitude of 152 km and a solar zenith angle of 178°. A comparison between the measured and modeled magnetic fields shows that the modeled crustal field contribution (Cain et al., 2003) matches the measurements almost exactly. This suggests that the magnetic fields here are dominated by crustal sources. On panels 3 and 4 are plotted electron fluxes and PADs obtained by SWEA, and the observations are divided into three time periods that show distinct PAD shapes. At the start of time period 1, a clear conic signature is present. Conical PADs were studied in detail by Ulusen et al. (2011), who proposed that they may be formed through the merging of neighboring open field lines, forming new closed loops. However, these signatures are rare enough ($< 1\%$) that they are ignored in this study. Here, the conic quickly transitions into a trapped distribution, indicating closed field topology. Transitioning to time period 2, SWEA begins to measure consistent one-sided loss cones, characterized by a strong depletion in field-aligned flux away from the planet. This suggests that the crustal fields being sampled here are connected to the IMF. The strong radial magnetic field component observed until 04:39 suggests that MAVEN is sampling a cusp between crustal field structures. After this point the field is directed more horizontally, but the one-sided loss cones remain, suggesting that MAVEN has likely transitioned to measuring the upper section of a weaker crustal field structure that is also open to the solar wind. This signature abruptly vanishes at 04:41, with the total electron flux dropping to near zero and remaining there. This extended electron depletion suggests that MAVEN is passing deep within closed nightside crustal fields. Here there is no solar wind input, and any trapped ionospheric population from the dayside has decayed away due to atmospheric absorption. At brief intervals we observe spikes in the electron flux, such as at 04:43 or just before 04:47. These have been observed previously (Mitchell et al., 2001), and are generally taken to indicate small pockets of open magnetic field located between closed crustal structures. Here, the flux spikes between 04:42 and 04:44 do not contain enough 100-300 eV electrons to be

recognized by our PAD processing, but the spike at 04:47 produces a brief loss-cone signature, with electron flux extending slightly past 90° pitch angle. This allows us to identify it as open to the solar wind.

2.5 Comparison to Mars Global Surveyor Results

Before studying the full distribution of field topologies across the nightside, it is useful to first make a comparison to the results obtained by Brain et al. (2007). Here we limit our MAVEN data to the region of space that was sampled by MGS, allowing us to directly compare PAD observation frequencies as an initial check for consistency. This is shown in Table 2.1, which contains the relative occurence rates for a variety of PAD shapes. For each shape, two numbers are shown. These represent the percentage of PADs on the nightside of Mars that exhibit the corresponding shape, as measured by MAVEN and by MGS, respectively. The MGS results are as reported in Brain et al. (2007), and the MAVEN results only use data taken between 1-3 hours local time and 350-450 km altitude.

While the observation frequencies reported by MAVEN and MGS for each PAD are not entirely equivalent, the overall trends shown are comparable. The most commonly identified PAD shape is an incident isotropic distribution with a loss cone in the return flux, generally indicative of open field lines. These account for $\sim$ 25% of all observations. Two-sided loss cones are also fairly dominant, accounting for 12% of MAVEN PAD measurements and 12.8% of MGS PAD measurements. As discussed before, these PADs usually represent particles mirroring within closed field topology. One large difference between the results of Brain et al. (2007) and those presented here is the decreased likelihood of measuring electron depletions. While MGS observed electron depletion PADs 31.5% of the time, MAVEN encounters them only $\sim$ 17% of the time while near 2 AM and 400 km. This discrepancy is mainly due to two factors. First, MAVEN's sampling near 2AM local time has not covered all geographic locations equally, with a greater number of PADs sampled in the Mars' Northern hemisphere. This means that the largest crustal field complexes (located in the southern hemisphere) were sampled less frequently, leading to comparatively small

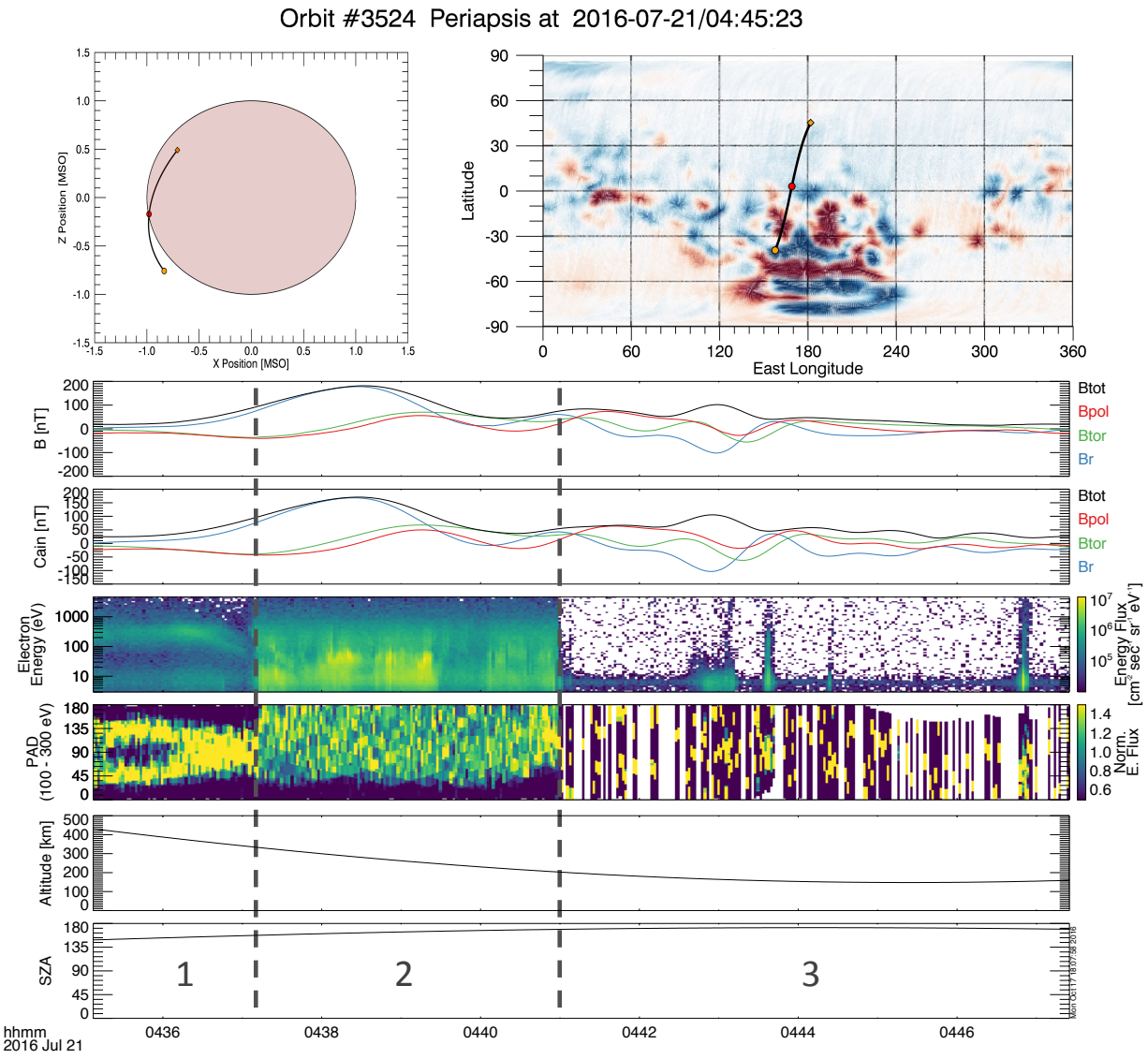

Figure 2.2: Inbound pass of MAVEN located deep on the nightside of Mars. The orbit trajectories shown in the upper panels are capped at an altitude of 500 km, with inbound marked by an orange circle, outbound an orange diamond, and periapsis a red circle. The upper right panel contains a map of radial crustal field strength measured by MGS, as shown in Brain et al. (2003). The instrument data panels show, in order from top to bottom: (1) magnetic field vector shown in spherical coordinates (Br = radial, Btor = toroidal [ϕ], Bpol = poloidal [θ], Btot = total magnitude), (2) Modeled crustal magnetic field contribution from the Cain model (Cain et al., 2003), (3) Electron energy spectrogram in units of energy flux, (4) Pitch angle distributions of 100-300 eV electrons, with each measurement normalized by its mean value, (6) MAVEN's altitude, and (7) Solar zenith angle.

frequency of observing electron depletions. Additionally, the increased accuracy of the SWEA instrument when compared to MAG/ER means that fewer PADs are found to have fluxes that are statistically equal to zero. This causes some PADs that would have been identified as electron depletions to instead be labeled as isotropic distributions with low count rates. For this reason, MAVEN has also observed fully isotropic distributions much more frequently than MGS, with these accounting for $\sim 20\%$ of observations rather than 8.8% of observations.

	Incident PAD Signature				
Returning PAD Signature	Isotropic	Loss Cone	Beam	Conic	Depletion
Isotropic	19.8 / 8.8	4.6 / 1.1	5.4 / 3.4	1.3 / 0.3	-
Loss Cone	25.7 / 23.1	11.8 / 12.8	4.4 / 7.5	0.9 / 0.4	-
Beam	0.6 / 0.6	0.1 / 0.2	1.3 / 2.8	0.5 / 0.2	-
Conic	0.4 / 0.8	0.2 / 0.3	1.9 / 3.9	1.3 / 1.4	-
Depletion	-	-	-	-	17.0 / 31.5

Table 2.1: Percentage of 100-300 eV PADs with the given PAD distribution. The percentages in each cell represent MAVEN observations and MGS observations, respectively. MAVEN data was limited to 350-450 km and 1-3 local time for the purpose of comparison to MGS's mapping orbit. MGS statistics are taken from Brain et al. (2007)

2.6 Statistical Maps

2.6.1 Open Field Lines

Brain et al. (2007) presented maps of one sided loss cone measurements using MGS data taken at 400 km, 2 AM local time. With these maps they showed that open field lines are found across the nightside at all geographic locations that are not dominated by crustal fields. Here we explore this result further, extending the analysis through the larger parameter space covered by MAVEN.

Figure 2.3a is a geographic map of one-sided loss frequency, using all MAVEN data taken below 500 km on the nightside of Mars. The color in each bin represents the fraction of PADs measured in that bin that exhibited a loss cone in upward electron flux. Overlayed on the map are contours of radial crustal magnetic field strength (20 and 40 nT) as measured at 400 km by MGS.

Throughout the strong crustal fields in the southern hemisphere, one-sided loss cones are relatively infrequent. This implies that the crustal fields, as would be expected, are rarely open to the solar wind. However, in the regions where crustal fields are directed most radially (the center of the contours), one-sided loss cones are observed very frequently, approaching 50% of observations. In this way we can see that these crustal cusp regions are frequently open to the solar wind, acting as narrow windows of connectivity among the crustal complexes.

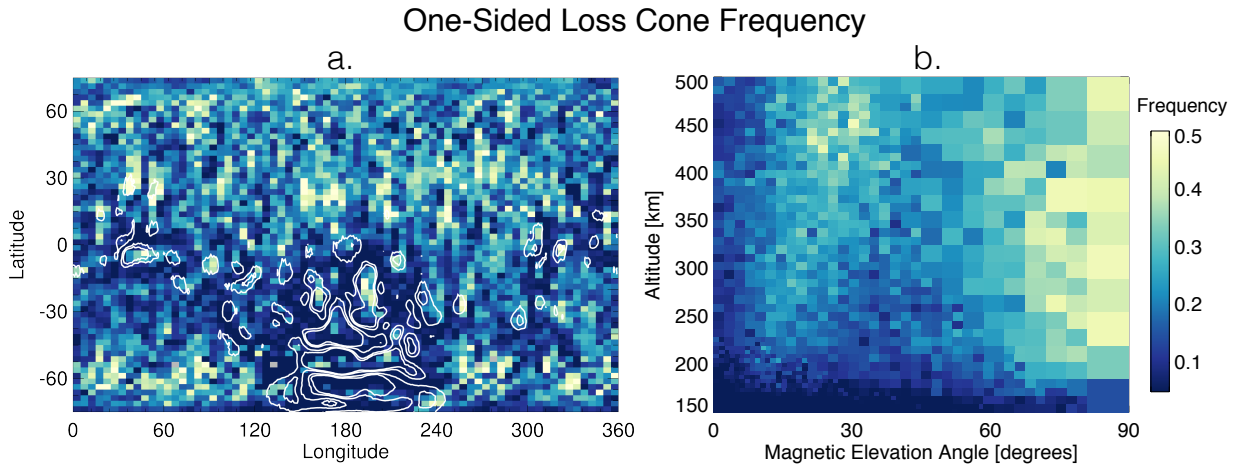

Figure 2.3: (a) Geographic distribution of one-sided loss cones on the nightside of Mars below 500 km. The bins are 2.5° by 2.5°, and the color in each bin represents the fraction of PADs measured within that bin that were identified as containing loss cones. "Nightside" is here taken to mean the geometric shadow of the planet. Contour lines of MGS inferred radial crustal magnetic field strength of 20 and 40 nT at 400km are included (Connerney et al., 2001). (b) Observation frequency on the nightside as a function of altitude and magnetic elevation angle. Colorbar applies to both figures.

Across the non-crustal regions, such as the weakly magnetized northern hemisphere, loss cones are more uniformly common. As discussed in Brain et al. (2007), these loss cones, while indicative of open field lines, don't necessarily suggest a connection to crustal sources. Rather, this signature could also be produced by draped lines of IMF that intersect the Martian atmosphere, with absorption and scattering producing a depletion in return flux. In regions of weak crustal magnetization, it is likely that both configurations are present, and in most respects they carry the same implications. In both situations the solar wind can interact with the Martian atmosphere to

deposit energy or guide ion escape, though the interaction might penetrate deeper when there are crustal sources guiding the field lines down toward the planet.

This is explored more in figure 2.3b, which shows nightside open field line frequency as a function of altitude and magnetic elevation angle. Here, 0° represents horizontal and 90° represents vertical with respect to the surface of the planet. Once again, bin coloration represents the fraction of PADs identified as one-sided loss cones, and here the bin size varies with data density such that each bin contains at least 100 data points. In this figure we can see two distinct favored orientations for open field lines. First, vertically oriented fields appear to display open topology at a relatively enhanced frequency. When these vertical fields extend to low altitudes (below $\sim$ 300 km), as they would in a crustal cusp, loss cones become particularly frequent, accounting for roughly 50% of observations. Second, one-sided loss cones are also found at low magnetic elevation angles, but more commonly when these fields are located at higher altitudes (above $\sim$ 400 km). This population of observed loss cones likely represents open field lines threading through the nightside atmosphere. At lower altitudes, a greater portion of horizontal fields are crustally sourced and closed to the solar wind. This leads to fewer measurements of one-sided loss cones. Interestingly, there appears to be a distinct minimum in loss cone frequency at the mid-range elevation angles between 40° and 60° . Open field lines are much more dominant in vertical crustal cusps and horizontal lines of draping IMF.

Nightside open field lines were also mapped by Xu et al. (2017a) through the identification of characteristic energy spectra. That study also found open field lines to be consistently present across the northern hemisphere, but at an overall lower frequency than we find here (20% of measurements as compared to 40%). Additionally, the open field lines that we identify throughout crustal field cusps are not reflected in Xu et al. (2017a). This is due to the open field identification method of that work requiring the presence of photoelectrons. Open field lines that connect directly to the nightside of Mars contain no photoelectrons and are therefore labeled as “draped” in their study, while those open fields that connect to the dayside of the planet are correctly classified.

2.6.2 Closed Field Lines - Electron Depletions

The distribution of observed electron depletions is explored in Figures 2.4a and b. Figure 2.4a shows a geographic map of electron depletion frequency for all PADs measured below 500km on the nightside of the planet. As expected, electron depletions are most commonly found in and around crustal field structures, and seem to be most dominant near the inner sections of the crustal field arcades. This agrees with the previous results of Brain et al. (2007) at 400km, as well as those of Steckiewicz et al. (2015), who studied decreases in electron fluxes in three different energy ranges measured by SWEA to analyze electron depletions in the Northern hemisphere of Mars. With this geographic distribution in mind, Figure 2.4b explores the altitude dependence of electron depletions. Plotted here is the frequency of observing electron depletions on the nightside as a function of altitude and crustal field strength. Crustal field strength is inferred using the Cain model of crustal fields (Cain et al., 2003). A trend can be immediately identified, with electron depletions measured more frequently at lower altitudes and in stronger crustal fields. Within the strongest crustal fields, electron depletions account for nearly 100% of measurements. Additionally, one can see here that at the lowest altitudes electron depletions dominate even in regions of weak crustal field strength. As discussed in Steckiewicz et al. (2015), this indicates the upper boundary of the collisonal atmosphere, where the electrons are lost due to CO_2 absorption regardless of their magnetic environment. Electron depletions were also mapped by Xu et al. (2017a), and the observation frequencies shown here agree very well with the results of that study.

2.6.3 Closed Field Lines - Two-Sided Loss Cones

A geographic map of trapped distributions is shown in Figure 2.5a. Once again this map includes all PADs measured below 500 km on the nightside of Mars. Like electron depletions, trapped PAD signatures are expected to indicate closed field lines. As such they are also seen to occur more frequently near crustal magnetic sources, with almost no trapped distributions found in the weakly magnetized sections of the Northern hemisphere. But unlike electron depletions,

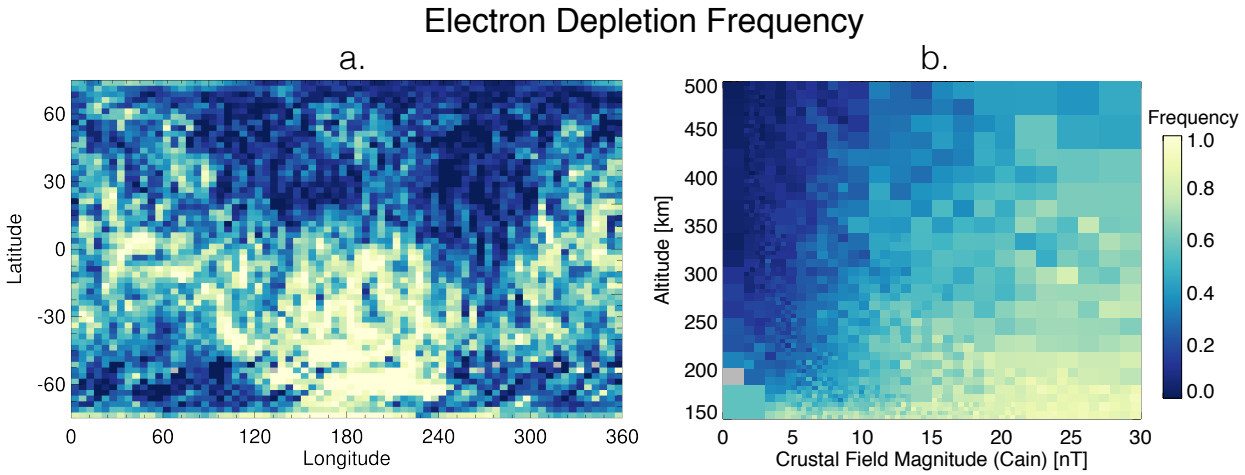

Figure 2.4: (a) Geographic distribution of electron depletions on the nightside of Mars below 500 km altitude. The bins are 2.5° by 2.5°, and the color in each bin represents the fraction of PADs measured within that bin that were identified as depletions. "Nightside" is taken to mean the geometric shadow of the planet. (b) Observation frequency as a function of altitude and modeled crustal field strength at the point of measurement (Cain model). Colorbar applies to both figures.

two-sided loss cones are preferentially located around the edges of crustal field structures. In the centermost sections of the large crustal field complexes, trapped distributions are almost entirely absent, but near the more weakly magnetized perimeters they are found frequently. We also observe that trapped distributions are especially common in an area near 140° E, 70° S, as was reported in Brain et al. (2007). Based on the study of Lillis and Brain (2013), it seems that this region also experiences consistently large fluxes of electron precipitation regardless of upstream solar wind conditions. The exact reason for this is not fully understood, but it is likely that the trapped distributions shown here are sourced from this enhanced electron precipitation.

We can investigate the altitude dependence of trapped distributions more fully with Figure 2.5b, which shows trapped distribution frequency as a function of altitude and crustal field strength. Here we can see that trapped distributions are found more commonly within strong crustal fields and at high altitudes. In this way, trapped distributions and electron depletions complement each other. Both are indicative of the closed topology found in crustal field loops, but while electron depletions dominate the enclosed low altitude sections, trapped populations fill the high altitude outer edges of the loops. This confirms a commonly held picture of closed field lines on the nightside

of Mars. The outer sections of crustal fields are populated with mirroring electrons that are likely supplied either through the recent closing of field lines by magnetic reconnection or through inward diffusion from the surrounding crustal cusps that are open to the solar wind. The inner layers are meanwhile significantly depleted, having lost much of their associated plasma population to atmospheric collisions. This was previously illustrated in Brain et al. (2007) using MGS data at 400 km and 2 AM local time. Here we have extended the analysis to show that the trend holds for data across the nightside of Mars.

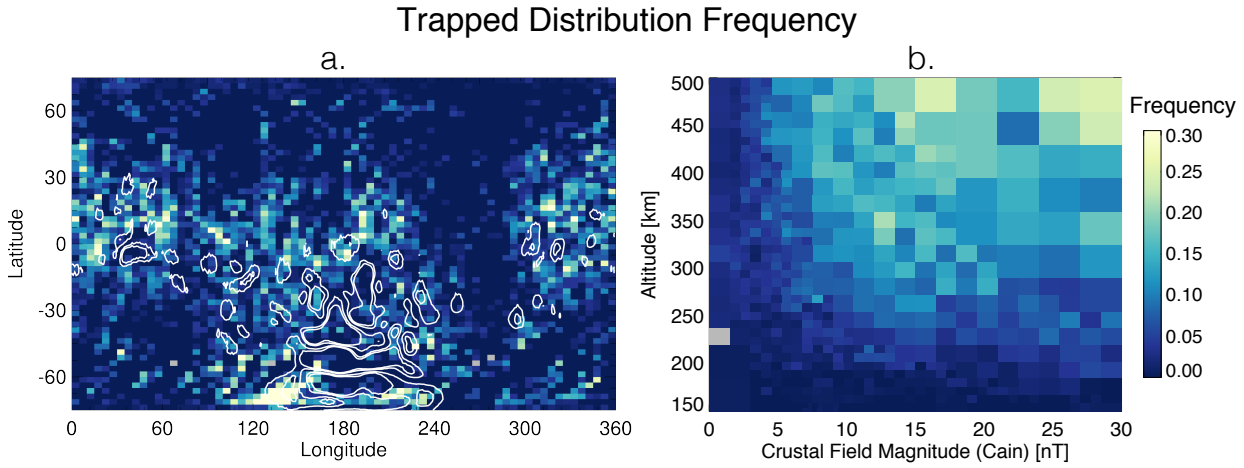

Figure 2.5: (a) Geographic distribution of two-sided loss cones on the nightside of Mars below 500 km. The bins are 2.5° by 2.5°, and the color in each bin represents the fraction of PADs measured within that bin that were identified as two-sided loss cones. Nightside is here taken to mean the geometric shadow of the planet. Contour lines of MGS inferred radial crustal magnetic field strength of 20 and 40 nT at 400km are included. (b) Observation frequency as a function of altitude and modeled crustal field strength at the point of measurement (Cain model). Colorbar applies to both figures.

2.7 Local Time Variations of Trapped Distributions

In addition to studying the frequency of PAD signatures across the nightside of Mars as a whole, MAVEN provides us with the opportunity to further analyze how these PAD frequencies vary with local time. Because MGS's mapping orbit was limited to 2AM/2PM local time, Brain et al. (2007) was never able to address how magnetic fields at Mars might experience topological

changes as they rotate around the planet. Here we can start to study this possibility. Continuing directly from the previous section, we focus our analysis on how trapped electron signatures vary with local time on the nightside of Mars.

While MAVEN's orbital progression has provided for data across all local times at Mars, the geographic and altitude coverage at each local time has varied greatly. Because we know that PAD shapes are strongly influenced by the crustal field environment, this means that we could encounter strong observational biases when separating our data. We therefore analyze the data in the manner of Figure 2.6, which explores how the frequency of observing trapped distributions on the nightside of Mars changes from dusk to dawn. Once again only considering data taken in the planet's shadow, we break our analysis into three sections of local time. For each local time segment, we map the observation frequency as a function of altitude and crustal field magnitude. Though the exact regions sampled to produce each panel may be different, dividing the data in this way allows us to remove the crustal field sampling biases present between local times.

In each of the three panels, the general trend in where trapped signatures are observed remains constant, with a higher observation frequency at higher altitudes and in strong crustal fields. However, moving from dusk (18 LT) to dawn (06 LT), the total occurrence rate of trapped PADs increases across all altitudes. At 200 km altitude this is an increase in frequency from ~ 0.05 to ~ 0.15, while at 400km it is an increase from a frequency of ~ 0.15 to ~ 0.25.

It is important to consider that the local time variations observed here might also be due to sampling biases present in the solar wind conditions. It is currently not well described how changes in the solar wind affect low-altitude topology at Mars, so we must account for the possibility that the upstream solar wind might have been very different when Maven sampled the dawn side of the planet as compared to the dusk side. This is explored in Figure 2.7. Here we show the chance of observing a trapped distribution below 500 km on the nightside of Mars as a function of the strength of the upstream solar wind. Solar wind dynamic pressure was determined for each measured PAD using MAVEN measurements of the solar wind from earlier in the same orbit (Halekas et al., 2016). One representative value of solar wind pressure was taken for each orbit and

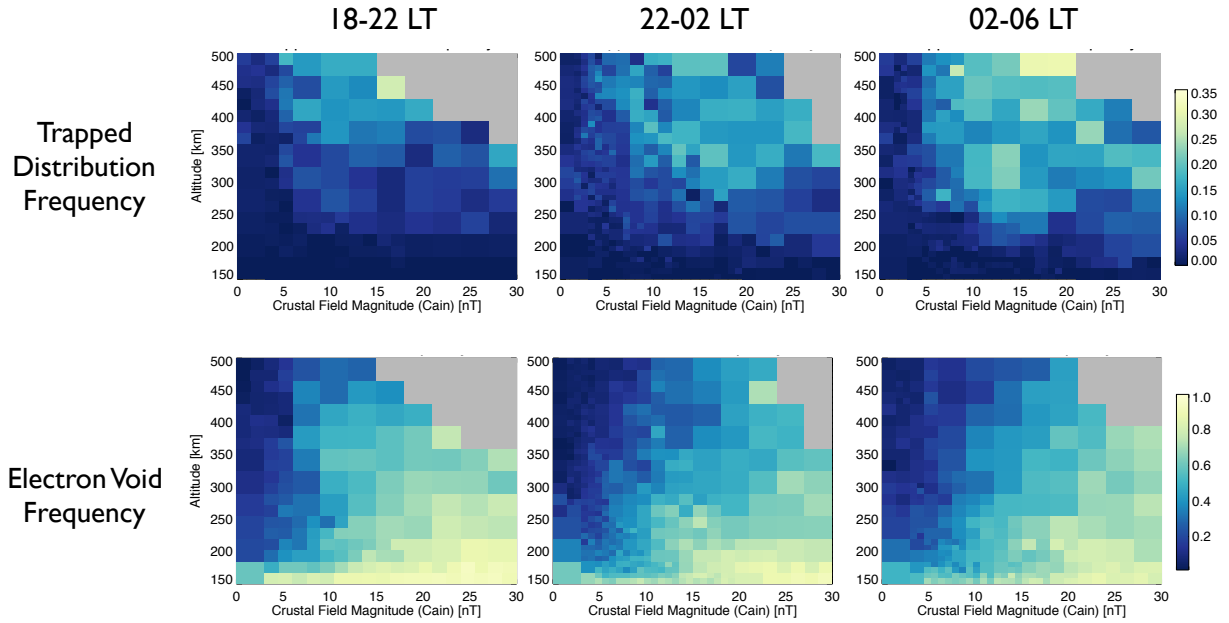

Figure 2.6: Observation frequencies of two-sided loss cones are shown as a function of altitude and modeled crustal field strength for three local time divisions. The color in each bin represents the fraction of PADs measured within that bin that were identified as two-sided loss cones. Gray is used for bins without an adequate number of data points (¡ 50). Only observations made within Mars' shadow are included here. Colorbar is shared between all panels.

applied to all the measurements made within that orbit. Orbits in which MAVEN did not sample the solar wind were excluded in making this figure. Because two-sided loss cones are essentially only relevant near crustal sources (see Figure 2.5), we also exclude PADs measured far from crustal fields (Cain Model Strength < 5 nT). Two sets of data points are shown on the plot. Those in red represent data taken between 18 and 24 local time (the duskward half of Mars' nightside), while those in blue represent data taken between 0 and 6 local time (the dawnward half). Vertical error bars were calculated from a simplistic Poisson statistic, using the square root of the number of

identified trapped PADs. Horizontal error bars represent the range of pressures used in calculating the corresponding percentage.

There are two main conclusions to be drawn from this figure. First, regardless of the incoming solar wind pressure, two-sided loss cones are found roughly twice as often on the dawn side of Mars as compared to the dusk side. This confirms the result shown in Figure 2.6 and demonstrates that it is not due simply to a solar wind sampling bias. Second, it appears that the incoming solar wind pressure does cause variability in low altitude PAD shapes, as the observation frequency of two-sided loss cones is not constant through the varied conditions. This is to be expected, as the magnetic topology across Mars is intrinsically dependent on interactions with the solar wind. However, there does not seem to be a straightforward trend present in the figure shown here (though a slight increase in trapped signature observations might be present at higher solar wind pressures). Solar wind drivers are likely to affect low altitude magnetic topology in a complex manner deserving of its own study. As such, the specifics and implications are not discussed here, and will rather be explored in a future work.

Thus far we have not identified a definite cause of the observed local time variations. One possibility is that magnetic fields are more likely to have closed topology on the dawnward half of the nightside. This would be surprising, but could conceivably be due to spatial differences in how reconnection processes are established in the Martian system. This possibility could be addressed through modeling studies. A second explanation could be that closed magnetic field loops become increasingly likely to contain trapped PADs rather than electron depletions as they rotate through the nightside. This could be due to a local time asymmetry in the electron precipitation that sources the trapped distributions, though the incoming electron flux is not expected to be higher near dawn.

2.8 Summary and Conclusion

We present a statistical analysis of electron pitch angle distributions calculated using the SWEA and MAG instruments aboard MAVEN. We use these pitch angle distributions to infer

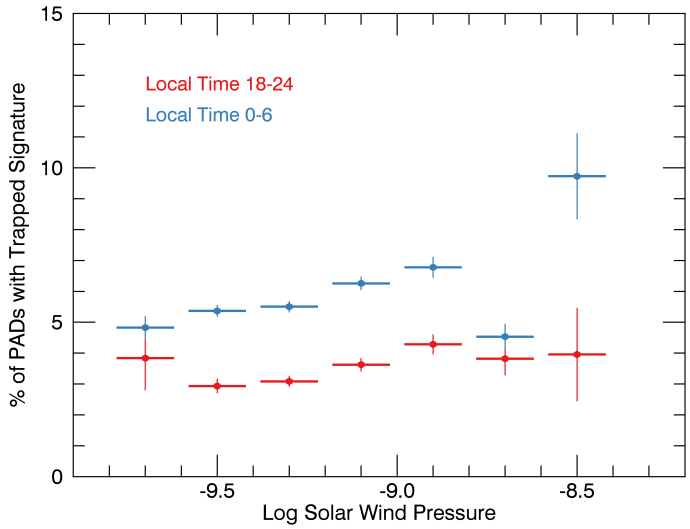

Figure 2.7: Percentage of observed PADs on the nightside of Mars showing a trapped signature during different upstream solar wind strengths. Only observations made near crustal fields (Cain model Strength $>$ 5 nT) and below 500 km were included in this figure.

the magnetic topology below 500 km across the nightside of Mars. We find good agreement with previous results obtained by the MGS spacecraft at 400 km altitude and 2 AM local time, and then extend this analysis to the broader range of altitudes sampled by MAVEN. We find that crustal sources on the nightside exhibit closed topology almost uniformly, and are composed of an outer layer of mirroring particles that surround a core significantly depleted of electrons. Open field lines are found across the nightside in two favored configurations. They drape across all regions not dominated by crustal sources, but only extend to the lowest altitudes consistently in the crustal cusps, where they descend directly vertically. We then present an analysis of local time variations in trapped electron signatures. Two-sided loss cones become increasingly frequent as crustal magnetic field sources move from dusk toward dawn across the nightside of Mars. While we have not identified a physical explanation for this, we can confirm that the variation appears to be guided by local time, rather than due to any sampling bias. The work presented here serves both to confirm the results of previous studies, as well as to act as a foundation for future studies on how magnetic topology at Mars varies with upstream solar wind conditions. As MAVEN continues

to collect PAD data, it is filling in an even more complete parameter space. Increased statistics at all local times, altitudes, geographic locations, and upstream conditions will allow for a better understanding of the topological dynamics in the Martian system. Through comparisons with other MAVEN datasets we should be able to quantify the effect that variations in magnetic topology have on particle outflow and energy transport.

Chapter 3

Effects of solar wind pressure

This chapter was originally published as "The influence of solar wind pressure on Martian crustal magnetic field topology" (Weber et al., 2019). It has been adapted here to fit within the narrative flow of the thesis.

Abstract: We present a study of changes in Martian magnetic topology induced by upstream solar wind ram pressure variations. Using electron energy spectra and pitch angle distributions measured by the Mars Atmosphere and Volatile EvolutioN (MAVEN) spacecraft, we classify the topology of magnetic field lines in the Martian space environment across a range of solar wind conditions. We find that during periods of high solar wind dynamic pressure, draped fields are pushed to lower altitudes on the dayside of the planet, compressing closed fields. At the same time, open topology becomes more prevalent on the nightside due to the broadening of crustal cusp regions. The result is a decrease in closed topology at all locations around Mars, suggesting that the Martian ionosphere becomes significantly more exposed to solar wind energy input during high solar wind pressure. This could likely contribute to elevated levels of ion escape during these periods.

3.1 Introduction

Magnetic fields in the Martian space environment facilitate a complex interaction between the solar wind and the planet's ionosphere. By directing the flow of charged particles, they control the structure of energetic electron precipitation across Mars (Dubinin et al., 008a; Lillis et al., 2009; Lillis and Brain, 2013; Xu et al., 2014a; Lillis et al., 2018). These electrons enter the atmosphere and impart energy, leading to impact ionization (Fillingim et al., 2007, 2010; Němec et al., 2011; Lillis et al., 2011; Lillis and Fang, 2015), local heating (Fox and Dalgarno, 1979; Krymskii et al., 2004; Sakai et al., 2016), and the production of aurora (Haider et al., 1992; Brain et al., 2006a; Leblanc et al., 2008). At the same time, magnetic fields also guide the outward flow of low energy ions, regulating ion escape processes in the martian ionosphere (Ergun et al., 2016; Collinson et al., 2015; Jakosky et al., 2018).

The Martian plasma processes described above are governed largely by the presence of crustal magnetic fields (Acuna et al., 1998, 1999; Brain et al., 2003), which interact and reconnect with the interplanetary magnetic field (IMF) to produce a unique and dynamic magnetic environment. The result is a system in which magnetic field lines can be (1) connected solely to Mars (closed), (2) connected to both Mars and the solar wind (open), or (3) connected solely to the solar wind (draped), as illustrated in Figure 1.8. Differentiating between these cases allows us to determine which locations around Mars are shielded from or exposed to solar wind influence, and provides insight into where and how ion outflow may occur. Magnetic topology at Mars has therefore been the subject of many studies, including several providing statistical maps of topology (Brain et al., 2007; Xu et al., 2017a; Weber et al., 2017) and many using topological analysis to support case studies of interesting phenomena in the Martian magnetosphere (e.g. Mitchell et al., 2001; Frahm et al., 2006b; Dubinin et al., 008b; Eastwood et al., 2008; Brain et al., 2010)

The reconnection processes that produce open and closed magnetic field lines occur continuously, meaning that magnetic topology at Mars is constantly changing. As the planet rotates, crustal magnetic field loops encounter new lines of IMF that might be favorable for reconnection.

It is therefore likely that many crustal field footpoints transition between open and closed topology as they rotate from day to night and back (e.g. Brain, 2007; Ma et al., 2014). Additionally, upstream IMF conditions can exhibit large changes on an hourly time scale, and these changes have been shown to affect Martian magnetic topology (DiBraccio et al., 2018). The direction of the incoming IMF in particular is a primary determinant of topology and morphology throughout the Martian magnetotail (Yeroshenko et al., 1990; Dubinin et al., 1994; Brecht, 1997), and it is likely (though has not yet been demonstrated) that that this dependency carries down to lower altitudes as well. Similarly, solar wind dynamic pressure has been shown to affect the large scale structure of the Martian magnetosphere (Verigin et al., 1993; Ma et al., 2002), but there has not yet been an evaluation of how solar wind pressure influences magnetic topology throughout the martian crustal fields. Here we present such an analysis, using measurements of electron flux and vector magnetic field from the MAVEN spacecraft to investigate how changes in solar wind dynamic pressure affect the occurrence rates of closed, open, and draped field topologies across mars.

In section 2 of this study we describe the instruments and data products used, the measurements we use to characterize upstream solar wind, and our method of identifying topology. In sections 3 and 4 we present results from the dayside and the nightside of Mars, respectively. And in section 5 we summarize our findings and discuss implications.

3.2 Methods

3.2.1 Identifying Topology

To identify magnetic topology in this study, we use a method that is presented and described in Xu et al. (2019). This method combines two previous techniques for analyzing topology that each have their own areas of strength and weakness. One method is that of using characteristic electron energy spectra to identify the presence of photoelectrons or solar wind electrons. By analyzing the presence and flow direction of these populations, one can determine whether a local magnetic field is connected to Mars, the solar wind, or both. This method is outlined in Xu et al. (2017a),

in which it was used to map magnetic topology across Mars. However, because this technique uses photoelectrons to identify field lines connected to Mars, it is unable to identify open fields connected to the nightside of the planet. Fortunately, this is the region that is most accurately analyzed by the second method, which uses characteristic electron pitch angle distributions to study the ways in which electron fluxes have been affected in the process of reaching the spacecraft. By identifying loss cones, we are able to determine whether a local magnetic field is connected to the Martian atmosphere in one or both directions. This approach is described in detail in Brain et al. (2007) and Weber et al. (2017), which used Mars Global Surveyor (MGS) and MAVEN data, respectively, to map magnetic topology at Mars. On the dayside of Mars, using this method of analysis becomes more difficult due to the presence of isotropic photoelectron production, and so the combined method instead uses the energy spectra technique in those situations. For a complete description of the logic tree used in the combined method for topology identification, see section 2.3 of Xu et al. (2019).

3.2.2 Instruments

Electron pitch angle distributions and energy spectra used in this study were measured using the Solar Wind Electron Analyzer (SWEA) (Mitchell et al., 2016) and Magnetometer (MAG) (Connerney et al., 2015) instruments on the MAVEN spacecraft (Jakosky et al., 2015a). SWEA is a hemispheric electrostatic analyzer that measures the fluxes of electrons ranging from 5eV to 4.6 keV with an energy resolution of $\Delta E/E = 16.7\%$. It has a 360 by 120 degree field of view, measuring electron energy flux distributions that we pair with magnetic field measurements to calculate pitch angle distributions and directional electron energy distributions. Magnetic field measurements are supplied by MAG, which uses two triaxal fluxgate sensors to produce vector field measurements at 32 Hz with an accuracy of 0.1 nT.

In this study we use data collected between 01 December 2014 and 26 April 2018. During this time, MAVEN's orbit continually precessed, providing data coverage across a range of local times, crustal field strengths, and solar wind conditions. Because this study is focused on mag-

netic topology within the Martian ionosphere, we only use data collected below 800 km altitude. Additionally, we exclude any data in which the electron pitch angle distribution had no coverage within the thirty degrees directly parallel or antiparallel to the field, as these field-aligned fluxes are necessary for our method of topology identification.

3.2.3 Solar Wind Data

In this study we separate data based on upstream solar wind conditions. To achieve this we used orbit averaged measurements of solar wind density and velocity from direct sampling of the solar wind by the Solar Wind Ion Analyzer (SWIA) instrument (Halekas et al., 2015). For orbits in which MAVEN did not directly encounter the solar wind, we instead use a proxy that is calculated using SWIA measurements of solar wind protons that have undergone charge exchange, entered the martian atmosphere, and are encountered by MAVEN at periapsis. These measurements are presented in Halekas et al. (015b). Those orbits where both the proxy and direct measurements were unavailable are excluded from this study.

A histogram of orbit-averaged solar wind pressure measurements is shown in Figure 3.1. In this distribution we divide the measurements into low, medium, and high solar wind pressure, as delineated in the figure. These divisions are used throughout the results presented in this paper.

3.3 Dayside Results

Figure 3.2 contains results that describe how solar wind pressure affects magnetic topology on the Martian dayside across a range of altitudes and magnetic field strengths. For this figure we only use data taken below 800 km and at a solar zenith angle of less than 90 degrees. Each panel shows how frequently a specific topology was observed in a given altitude range as a function of field strength (more specifically, the average field strength observed in that location at 400 km by MGS). Each column therefore corresponds to the full set of topologies observed at a given altitude, while each row corresponds to how an individual topology varies across altitude. The results in each panel also contain three separate lines corresponding to low, medium, and high solar wind

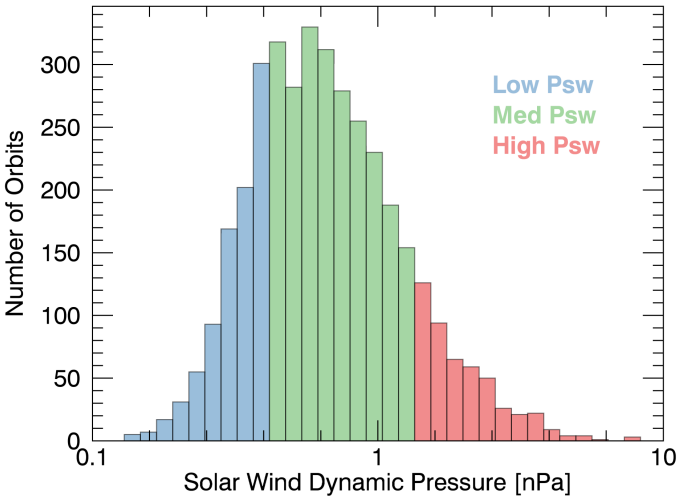

Figure 3.1: A histogram of orbit-averaged MAVEN measurements (either direct or by proxy) of solar wind dynamic pressure. The histogram is split into three subdivisions, representing the definitions of low, medium, and high solar wind pressure that are used in this study.

pressure, using the divisions described in Figure 3.1.

Beginning with the panels describing closed topology (top row), we can see that closed field topology becomes less common at higher altitudes, as would be expected, and that this change is most pronounced in the weaker field regions, where crustal field loops do not extend as high above the surface. Additionally, we see a dependence on solar wind pressure, with high pressure leading to a decrease in closed field topology of up to a factor of two. This variation is strongest at higher altitudes and over regions of lower field strength, where crustal field influences are weaker and more susceptible to solar wind forcing. By contrast, the strongest crustal field regions show almost no variation with solar wind pressure, remaining mostly closed in all situations. Finally, at altitudes just above the traditional exobase region (170-250 km), fields exhibit closed topology consistently, regardless of crustal field strength or solar wind conditions. This is in agreement with Xu et al. (2017a), in which maps of magnetic topology showed almost uniformly closed fields below 200 km on the dayside.

Moving to the panels describing open topology (middle row), we can see that open fields be-

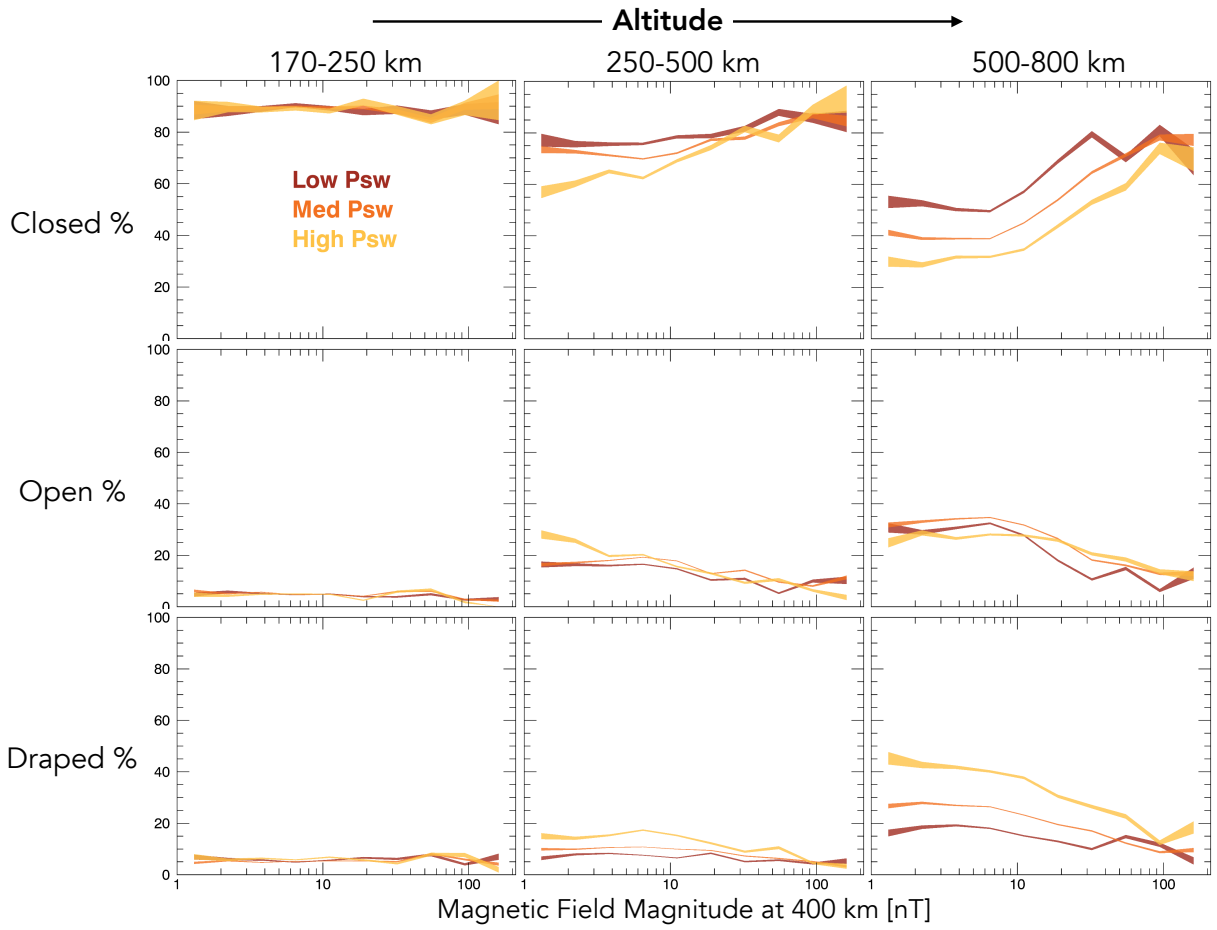

Figure 3.2: Each panel in this figure displays the percentage of observations within an altitude range (denoted at the top) that were of the specified magnetic topology (denoted on the left). Within each panel the results are plotted as a function of the average crustal magnetic field strength at 400km, as measured by MGS. The results are separated into three lines that correspond to measurements taken during low, medium and high solar wind pressure conditions, and the width of each line represents a one standard deviation error in the calculated percentage. This figure only uses data collected on the dayside of Mars, where dayside and nightside are defined by the geometric shadow of the planet.

come more prevalent at higher altitudes, and that there is a dependence on magnetic field strength, with the strong field regions being open to the solar wind less frequently than the weaker regions. However, the frequency of open field topology does not depend strongly on solar wind pressure. Rather, the decrease in closed field topology observed at high solar wind pressure appears to be offset by an increase in draped topology (bottom row), for both the mid-altitude and high-altitude regions. This suggests that the reduction in dayside closed topology caused by high solar wind pressure is primarily due to incoming draped fields being pushed to lower altitudes and compressing crustal field loops. This is illustrated in Figure 3.3, which contains a depiction of the crustal field response to high solar wind pressure on both the dayside and the nightside of Mars.

In interpreting these results, it is important to note that the trends identified here apply to the statistical whole, but that any individual region or magnetic cusp may respond somewhat differently. Additionally, in this study we group together regions of similar magnetic field strength and treat them as generally behaving in the same way, but we recognize that this may not always be the case. For example, Xu et al. (2017) found an asymmetry on the dayside between certain low-altitude unmagnetized regions in the northern and southern hemispheres, a feature that is not explored in this study.

3.4 Nightside Results

In Figure 3.4, we present data in the same format as Figure 3.2, but now only using data taken within the geometric shadow of the planet.

We can see many similar trends those observed on the dayside. At higher altitudes we observe less closed topology and more open and draped topology. Closed fields are also more common in the stronger crustal field regions, while open and draped fields are less common. However, this dependence on the local crustal field environment appears to be much stronger on the nightside of Mars. While on the dayside fields are almost uniformly closed below 250 km, on the nightside in this same region we see a variation in closed topology frequencies from 30% to 70%, depending on the crustal field strength. This trend holds at higher altitudes as well. Between 500 and 800 km

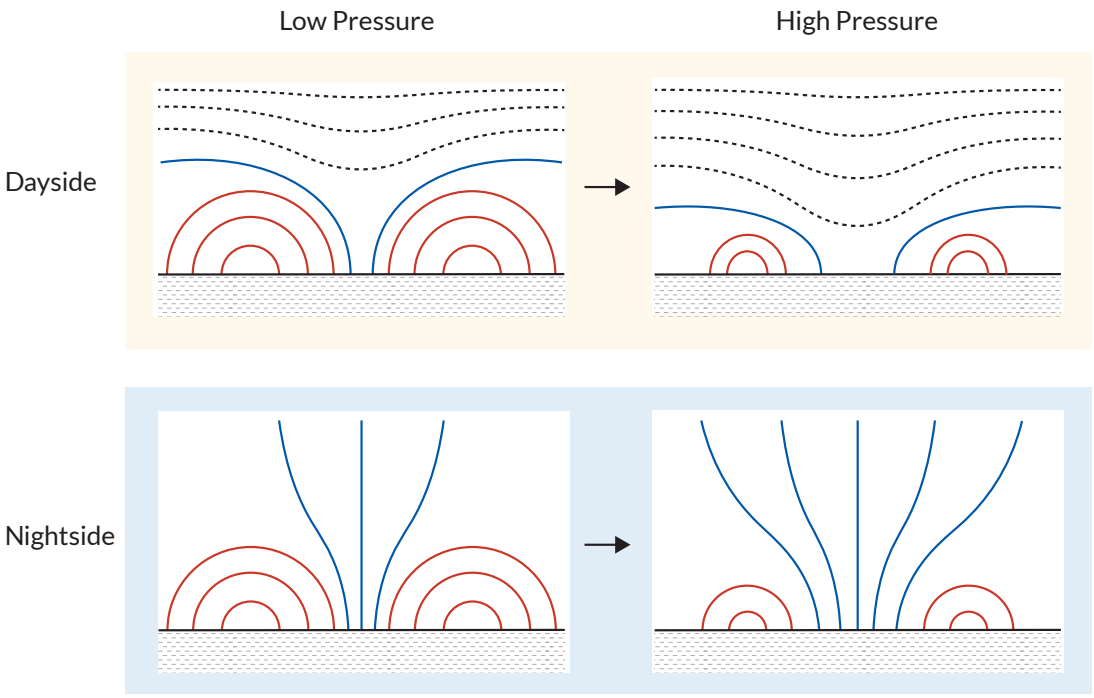

Figure 3.3: An illustrative diagram of how crustal fields on the dayside and the nightside respond to an increase in solar wind pressure.

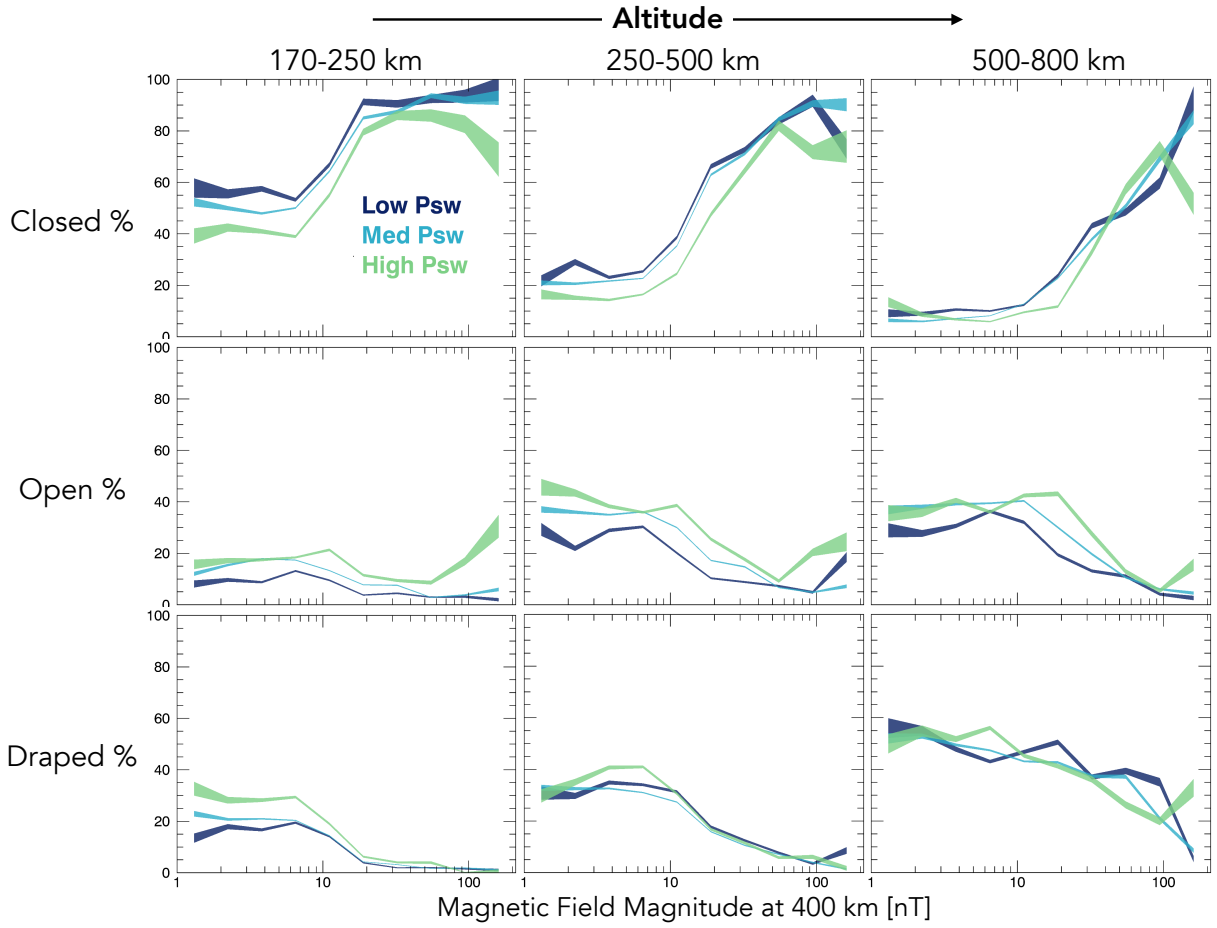

Figure 3.4: Each panel in this figure displays the percentage of observations within an altitude range (denoted at the top) that were of the specified magnetic topology (denoted on the left). Within each panel the results are plotted as a function of the average crustal magnetic field strength at 400km, as measured by MGS. The results are separated into three lines that correspond to measurements taken during low, medium and high solar wind pressure conditions, and the width of each line represents a one standard deviation error in the calculated percentage. This figure only uses data collected on the nightside of Mars, where dayside and nightside are defined by the geometric shadow of the planet.

altitude, closed topology is found in the weak field regions close to 0% of the time but in the strong field regions up to 80% of the time.

Solar wind pressure variations are also similar to those seen on the dayside, but with a few important differences. Just as on the dayside, high solar wind pressure decreases the frequency of closed fields, but unlike on the dayside these changes are more pronounced at lower altitudes than at high altitudes. Between 180 and 250 km, high solar wind pressure leads to a decrease in closed field topology of 20 percentage points across all field strength, while at 500-800 km altitude we see little variation with solar wind pressure, if any. Additionally, on the dayside this reduction in closed topology is balanced solely by an increase in draped topology, but on the nightside it is instead primarily balanced by an increase in open topology. Furthermore, these variations are present across all crustal field strengths, whereas on the dayside it is only the weak field regions that exhibit variations with solar wind pressure. Because we see this pressure-driven increase in open topology at low altitudes and in strong crustal field regions, it appears that we are seeing the expansion and broadening of crustal cusp regions on the nightside during periods of high solar wind pressure, as is illustrated in Figure 3.3.

It is not immediately apparent why increased ram pressure in the upstream solar wind would compress crustal fields on the nightside of the planet, but we believe that this effect is due to an associated increase in magnetic field strength in the Martian magnetotail. It has been demonstrated that an increase in solar wind pressure translates into increased magnetic pressure in the tail (e.g. Lillis et al., 2018), and we suggest that this causes the compression of nightside crustal fields and produces the topological trends shown here.

3.5 Discussion and Conclusion

In this work we used a new method of topology identification to analyze how changes in solar wind pressure affect topology at Mars across a range of magnetic field strengths. We find that high solar wind pressure tends to decrease the presence of closed fields throughout the Martian system, with the most substantial changes occurring in regions of weaker crustal field influence. On the

dayside of the planet, this decrease in closed topology is due to an increase in draped topology, with lines of unconnected IMF extending to lower altitudes during periods of high pressure. On the nightside of the planet, it is instead complemented by an increase in open topology, due to the expansion of crustal field cusps.

Both of these variations are likely to cause an increase in ion outflow. As draped fields penetrate to lower altitudes on the dayside, they interact with more and more ions that they are able to remove through the $\mathbf{J} \times \mathbf{B}$ force and the motional electric field. At the same time, the increased presence of open topology on the nightside creates additional pathways for cold ion outflow down the magnetotail. Previous studies have shown that high solar wind pressure can increase global ion outflow from Mars (Edberg et al., 2010; Nilsson et al., 2011; Ma et al., 2014), and we suggest that this effect is caused in large part by the topological changes demonstrated here.

Additionally, changes induced by solar wind pressure, such as those presented here, are of particular note when taken in the context of conditions throughout solar system history. Models and observations of other stars have suggested that several billion years ago, when the Martian dynamo shut off and crustal magnetic fields first began to interact with the solar wind, the solar wind pressure was on the order of 100 times as strong as the present day value (e.g. Lammer et al., 2004; Grießmeier et al., 2004; Lundin et al., 2007). It is thus probable that conditions and variations even more extreme than those shown in the "high" solar wind pressure case here were prevalent during this period. This in turn could produce enhanced ion outflow during that time period, though it is important to note that at that point in time the Martian atmosphere was at least 20 times thicker (e.g. Kite et al., 2014), and the crustal fields may have been stronger than today (Shahnas and Arkani-Hamed, 2007). The net result of these competing effects could be investigated more thoroughly in the future with the use of numerical models.

Chapter 4

Effects of interplanetary magnetic field direction

This chapter was originally published as "The influence of interplanetary magnetic field direction on the topology of Martian crustal field cusps" (Weber et al., 2020). It has been adapted here to fit within the narrative flow of the thesis.

Abstract: Crustal magnetic fields influence a range of plasma processes at Mars, guiding the flow of energy from the solar wind into the planet's atmosphere at some locations while shielding it at others. In this study we investigate how the topology of crustal fields varies with changes in the direction of the incoming interplanetary magnetic field (IMF). Using plasma measurements from MAVEN and MGS, we identify magnetic topology throughout the Martian ionosphere and perform a statistical analysis of crustal magnetic field topology during different IMF configurations. We find that the topology of crustal field cusp regions is dependent on IMF direction, and that cusps transition between open and closed topology regularly as they rotate through the nightside of Mars. Finally, we determine that cusps often become topologically closed due to reconnection with open magnetic fields in the Martian magnetotail, creating large closed loops that connect the dayside and nightside of Mars.

4.1 Introduction

The flow of charged particles in and out of the Martian ionosphere is in many areas controlled by the presence of crustal magnetic fields (Acuna et al., 1998), regions of remanent magnetization that are scattered non-uniformly across the planet's surface (See Figure 4.1a). As these crustal fields interact and reconnect with the interplanetary magnetic field (IMF), they create a complex and dynamic magnetic system that controls both solar wind energy input and low energy ion outflow from the planet. Energetic electrons from the solar wind precipitate along these magnetic fields, depositing their energy into the planet's atmosphere (Dubinin et al., 008a; Lillis et al., 2009; Lillis and Brain, 2013; Xu et al., 2014a; Lillis et al., 2018). This deposition is second only to solar photon absorption as an atmospheric energy source (Fox et al., 1993), and leads to local heating (Fox and Dalgarno, 1979; Krymskii et al., 2004; Sakai et al., 2016), impact ionization (Fillingim et al., 2007, 2010; Němec et al., 2011; Lillis et al., 2011; Lillis and Fang, 2015), and the production of aurora (Haider et al., 1992; Brain et al., 2006a; Leblanc et al., 2008). Magnetic fields also constrain the movement of escaping low energy ions, regulating the ion outflow processes that may have contributed to substantial atmospheric loss over time (Harnett and Winglee, 2006; Nilsson et al., 2011; Ma et al., 2014; Collinson et al., 2015; Ergun et al., 2016; Ramstad et al., 2016; Jakosky et al., 2018).

It is therefore useful for us to evaluate where and when magnetic fields allow for direct connection between the solar wind and the ionosphere, an area of study referred to as magnetic topology. In analyzing topology we differentiate between cases when magnetic field lines are (1) connected only to Mars (closed), (2) connected only to the solar wind (draped), or (3) connected to both Mars and the solar wind (open). These distinctions inform us of which locations at Mars are exposed to solar wind energy input, and reveal where and how ion outflow is likely to occur. As such, magnetic topology has been the subject of a large number of studies at Mars, including statistical analyses of magnetic topology across the planet (Brain et al., 2007; Luhmann et al., 2015; Xu et al., 2017a; Weber et al., 2017; Xu et al., 2019), as well as many studies that used topological

analysis as a baseline for understanding unique phenomena in the Martian space environment (e.g. Mitchell et al., 2001; Frahm et al., 2006a; Leblanc et al., 2006; Dubinin et al., 008b; Liemohn et al., 2007a,b; Eastwood et al., 2008; Brain et al., 2010).

Magnetic topology at Mars is dynamic, evolving constantly as the interaction between the planet and the solar wind changes. As crustal magnetic fields rotate with the planet, they are frequently exposed to new lines of draped IMF that may be favorable for reconnection. This means that individual crustal field loops are likely to vary between open and closed topology on the timescale of Mars's rotation. Meanwhile, upstream solar wind parameters can also change substantially on an hourly timescale, affecting the entire Martian system as they do. Variations in solar wind dynamic pressure are seen to influence the overall structure of the planet's magnetosphere (Verigin et al., 1993; Ma et al., 2002), and were shown recently to drive planet-wide changes in the topology of Martian crustal fields (Weber et al., 2019). Similarly, IMF direction has been demonstrated to control the morphology and topology of the Martian magnetotail (DiBraccio et al., 2018). However, there has not yet been a direct analysis of how topology in Martian crustal field regions is influenced by upstream IMF direction. Here we present an analysis of this kind, using measurements of electron flux and magnetic field to investigate how the direction of the IMF influences whether crustal magnetic fields are open or closed to the solar wind. To accomplish this, we use data from both the Mars Global Surveyor (MGS) and Mars Atmosphere and Volatile Evolution (MAVEN) spacecraft, making use of the high data density of the former as well as the large parameter space of the latter.

In section 2 of this study we present results using MGS data, including a description of our methodology and an explanation for the trends we observe. In section 3 we evaluate these results further using MAVEN data, verifying our proposed explanation. And in section 4 we discuss the the broader implications of our findings and suggest future avenues of investigation.

4.2 Mars Global Surveyor Analysis

4.2.1 Instruments and Data Collection

The analysis of MGS data conducted here is based directly on that of Brain et al. (2007), and uses the same method of topology analysis as was presented in that study. This involves the identification of characteristic electron pitch-angle distributions (PADs), as measured by the MGS Magnetometer and Electron Reflectometer (MAG/ER). ER was a top hat electrostatic analyzer designed to measure directional electron energy fluxes across a range of energies from 10 eV to 20 keV, and these directional fluxes are then coupled with vector magnetic field measurements from MAG to produce electron PADs (Mitchell et al., 2001). Following the method of Brain et al. (2007), we use PADs calculated from the energy channel that spans from 95 ev to 148 ev, as these energies provide the highest signal-to-noise for the purpose of this analysis. By analyzing these electron PADs in search of characteristic PAD shapes, we are able to determine whether or not the magnetic field lines that MGS encounters are connected to the Martian atmosphere. In particular, we take any distributions with one-sided loss cones in the return flux to represent open field lines, while two-sided loss cones and electron depletions (sometimes called "voids") are indicative of closed fields. For a full description of the topology identification method, including an explanation of which data were excluded, refer to section 2 of Brain et al. (2007)

4.2.2 Interplanetary Magnetic Field Determination

To study the influence of IMF direction, we organize our data using an IMF proxy that was presented in Brain et al. (2006b). This proxy uses direct measurements of magnetic field direction within a region of the weakly magnetized northern hemisphere of Mars to infer the draping direction of the IMF. The measurements are orbit-averaged, with the assumption that external conditions do not change appreciably during each two hour orbit. While it is unlikely that the IMF actually remained constant during each orbit, the proxy has been shown to perform well on average, and we expect that for the large-scale statistics presented here the orbit-averaged measurements should

still group the data meaningfully.

For each orbit we then calculate an IMF clock angle, and use this to separate our data into periods of "duskward" and "dawnward" IMF. Duskward corresponds to IMF pointing toward the dusk side of the planet (Eastward on the dayside), and dawnward corresponds to clock angles pointing toward dawn (Westward on the dayside), distinctions that are used throughout the rest of this paper.

4.2.3 Results

In Figure 4.1b, adapted from Brain et al. (tted), we use 7 years of MGS PAD measurements to explore how crustal magnetic field topology on the nightside of Mars changes during different IMF configurations. We begin our analysis on the nightside as this is the region most accurately studied by our method (active photoelectron production on the dayside tends to isotropize PADs and drown out any other signatures). Using characteristic PAD shapes, we create a geographic map in which each 1° x 1° bin is colored by the difference in how often closed topology was observed during periods of duskward and dawnward IMF. Regions colored red exhibited closed topology more frequently during duskward IMF, while those colored blue showed closed topology more often during dawnward IMF.

There are several trends of note in this figure. First, as Brain et al. (tted) have pointed out, we can see that the strongest crustal field complexes show little to no variation with changes in IMF direction. Rather, the strongest changes seem to be located in regions of more moderate field strength (e.g. the crustal fields between 240°–300° longitude and -30°–0° latitude). This is a fairly intuitive result, suggesting that at MGS's fixed altitude of 400km the centers of the large crustal field loops are effectively isolated from the influence of any externally imposed fields, while the smaller crustal fields are more susceptible to change at this altitude.

Second, the areas located between the strong crustal field arcades, typically referred to as "cusp" regions, also show a large amount of variation. Cusps have previously been shown to most frequently contain open field lines, allowing for energy transfer and ionospheric outflow, but here we

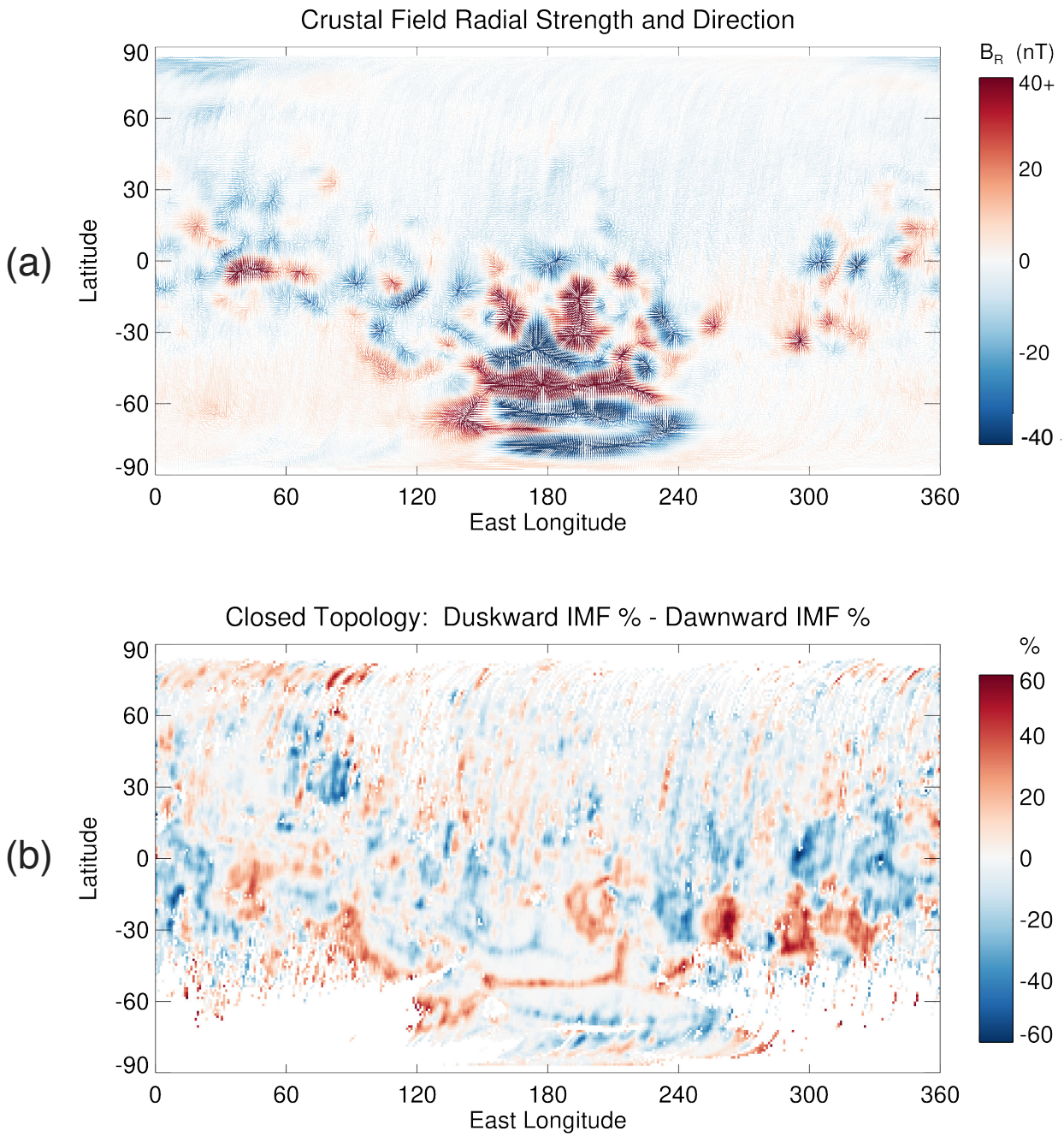

Figure 4.1: (a) This map of the crustal magnetic fields at 400 km altitude is adapted from Brain et al. (2003). Each 1° by 1° bin contains a vector whose length and direction correspond to the median horizontal field component measured in that bin by MGS. These vectors are colored by the median radial field component of that bin, with red signifying fields directed upward and blue signifying fields directed downward. (b) This map shows the difference in how often closed field topology was observed by MGS at 2 AM local time for dawnward and duskward IMF configurations. For each 1° x 1° bin, the color represents the percentage of observations that showed closed topology during duskward IMF minus the percentage that showed closed topology during dawnward IMF.

see that they will also often exhibit closed topology depending on the incoming IMF configuration. In the strongest cusp regions, closed topology observation frequencies vary with IMF direction by as much as 50 percentage points. For some cusps, closed topology occurs more often during duskward IMF, while for others closed topology is more prevalent during duskward IMF, and a comparison with the crustal field map shown in Figure 4.1a reveals that this is correlated with each cusp's radial magnetic field direction. In particular, cusps that are directed radially outward show closed topology more often for duskward IMF (i.e. crustal field regions colored red in Figure 4.1a are also colored red in Figure 4.1b), while those that are directed radially inward are closed more often when the IMF is directed dawnward (i.e. crustal field regions colored blue in Figure 4.1a are also colored blue in Figure 4.1b). Note that this trend does not hold throughout the unmagnetized northern hemisphere, where the smaller magnitude variations should be treated as noise.

The implication here is that IMF direction determines which crustal field cusps are most likely to be closed or open to the solar wind, with a dependence on cusp radial magnetic field direction. We believe that this is due to open cusp fields reconnecting with fields in the magnetotail, a process that inherently depends on the prevailing direction of the draped IMF. We explore this in more detail below, with a simplified schematic of our explanation shown in Figure 4.2.

In interpreting this result, it is important to keep in mind that we are only looking at nightside results, and that nightside data from MGS was all located at 2 AM local time. This fixed local time meant that for a given IMF direction there was a prevailing draped field direction encountered by MGS. Specifically, duskward IMF leads to draped fields near 2 AM primarily pointing toward the planet, while for dawnward IMF they are primarily pointing away from the planet.

With this in mind, we can then note that open cusp field lines extend into these magnetotail lobes, and that those directed opposite the direction of the lobe field are in a favorable orientation to reconnect with tail field lines. This means that cusps directed radially inward may be likely to reconnect with the tail during periods of dawnward IMF, whereas those directed outward would not, remaining as unaffected open field lines. This is illustrated in Figure 2. Outward cusps should therefore have open topology more frequently (and closed topology less frequently) during

dawnward IMF, as we observe in Figure 4.1b. But in order to understand why they often end up closed during periods of duskward IMF, it is helpful to consider the possible outcomes from the reconnection of an individual field line.

When an open field line from a crustal cusp reconnects with a field line in the magnetotail, the resulting topology depends on the initial topology of the tail field line. If the tail field it reconnects with was draped, then the resulting field line coming out of the cusp will still be open, meaning there has been no change in topology. If the tail field it reconnects with was another open field, however, the resulting field line will now be a closed loop. A simplified illustration of this is shown in Figure 4.2. Here one might note that other open fields will not necessarily be oriented in the same direction as the tail lobe, and as such might not be a likely source for frequent reconnection. However, it is important to consider that by "open" we are referring not just to field lines connecting down to crustal magnetic field sources, but also to draped lines of IMF deeply embedded in the Martian ionosphere. These draped field lines connect the exobase to the solar wind, so in the context of atmospheric escape and topology identification they are treated as open fields, but importantly they are oriented in the same direction as the tail lobes. Recent studies have shown that these open and embedded draped fields make up a sizeable portion of the magnetotail, particularly in the inner sections of the tail near the Mars-Sun line (DiBraccio et al., 2018; Xu et al., 2020b).

Because these fields are common throughout the tail, it is expected that oppositely-directed cusps should sometimes reconnect with them, producing loops that connect the dayside and nightside of Mars. Such a situation was observed by Xu et al. (2016), who found the presence of dayside photoelectron signatures deep on the nightside of the planet. The occurrence rate of these loops was investigated further in Xu et al. (2017a), with certain regions in the northern hemisphere showing nightside photoelectron signatures 20-30 % of the time. Here we suggest that day-night closed loops also frequently reach all the way to crustal field cusps on the nightside, throughout the strongest crustal field complexes as well as the more moderate crustal field regions. The observable end result is that cusp fields become topologically closed given the necessary IMF orientation, as shown by

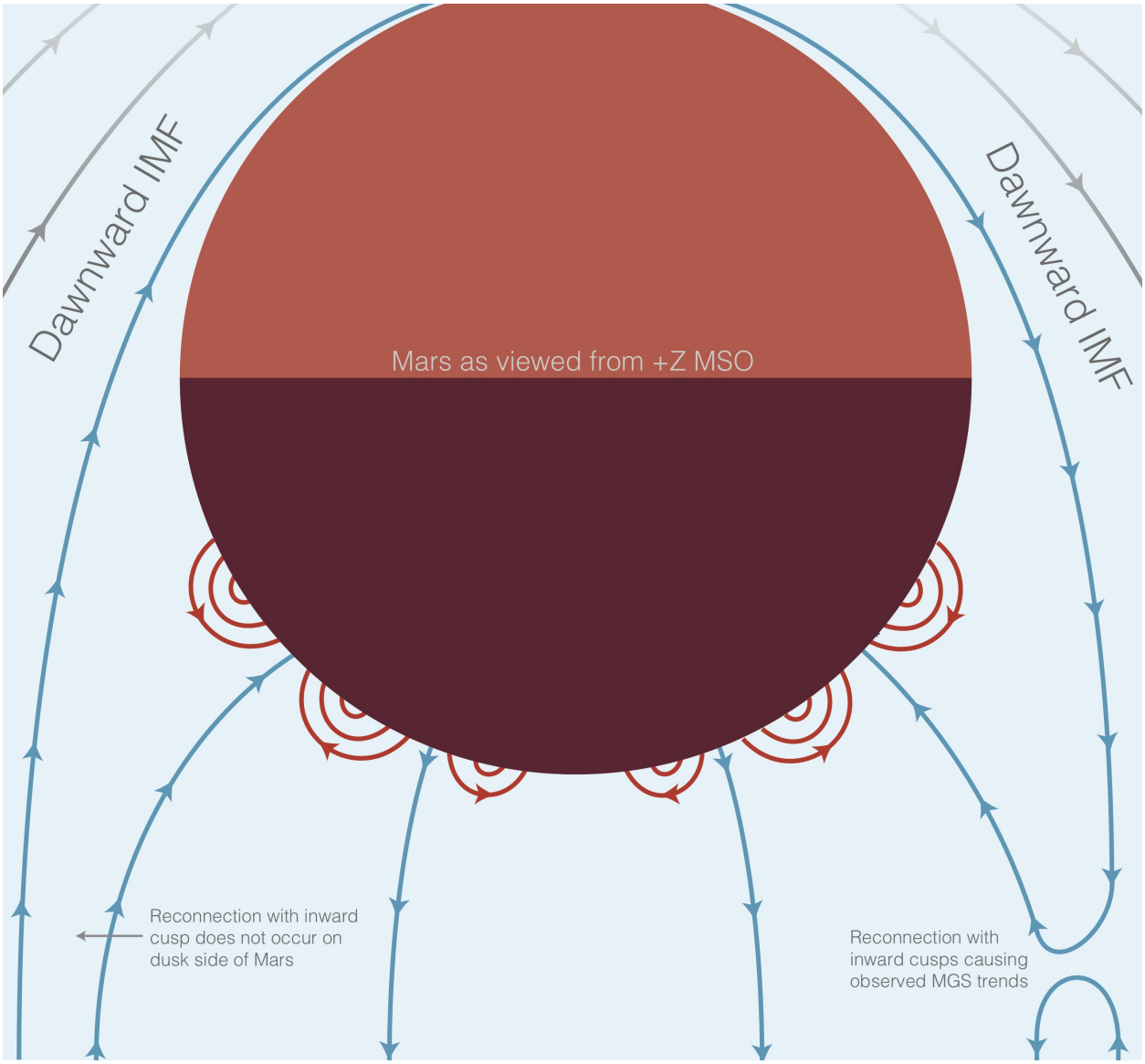

Figure 4.2: An illustration of open field lines from the dayside and nightside of Mars reconnecting to form a large day-to-night closed loop. Many of these dayside open field lines are in reality draped lines of IMF that thread through the ionosphere. These should follow the general draping direction of the IMF, which is represented here by the black lines. Note that the faded black lines at the bottom of the figure are intended to illustrate the draping direction and the three-dimensional nature of the situation, and don't necessarily fall into the same plane as the open field lines in the figure.

the trend in Figure 4.1.

To provide verification for this idea, we can search for other features that our interpretation suggests should be present. First, if these closed fields originating in cusp regions are indeed connected to the dayside of Mars, we should expect to see photoelectron signatures propagating tailward along the field line, as observed in Xu et al. (2016). Second, if the variations in cusp topology are in fact due to reconnection with field lines in the magnetotail, we should expect to observe opposite trends in the two magnetotail lobes. That is, if we believe that MGS is observing upward cusp fields at 2 AM reconnecting with the tail field and becoming closed, we should expect that at 10 PM local time we would instead see downward cusp fields reconnecting, as the direction of the tail field is reversed here. While the mapping orbital configuration of MGS, which was fixed at 400 km altitude and 2 AM / 2 PM local time, prevents us from using it to investigate this possibility, the orbit of the MAVEN spacecraft is not subject to the same constraints. In the next section, we use measurements from the MAVEN spacecraft to explore these predictions, and are able to identify both of the features described here.

4.3 MAVEN Analysis

4.3.1 Identifying Topology with MAVEN

To identify magnetic topology with MAVEN, we use a technique presented in Xu et al. (2019). This method combines two different strategies for topology analysis at Mars, effectively capturing the strengths of each. One approach is that of identifying characteristic PAD shapes to determine whether electron fluxes have interacted with the Martian atmosphere. This is the same approach that was used for the MGS data analysis in this study, and has also been used to map magnetic topology at Mars using MAVEN data (Weber et al., 2017). This method is very effective on the nightside of the planet, but is less robust on the dayside of Mars, where the active isotropic production of photoelectrons tends to drown out the PAD shape signal. Fortunately, the dayside of the planet is the region that is most accurately studied by the second method, which uses

characteristic electron energy spectra to identify whether MAVEN is encountering photoelectrons, solar wind electrons, or both. By studying the directional fluxes of these different populations, we are able to accurately determine magnetic topology across the dayside of Mars, as demonstrated in Xu et al. (2017a). The combined method therefore employs these two strategies in parallel, using both sets of information to determine magnetic topology throughout the entire Martian system. A more complete description of this system of topology identification can be found in section 2.3 of Xu et al. (2019)

4.3.2 Instruments and Data Collection

The electron energy spectra and pitch angle distributions used in this section of the study were measured using the Solar Wind Electron Analyzer (SWEA) and Magnetomenter (MAG) instruments aboard MAVEN (Jakosky et al., 2015a; Connerney et al., 2015; Mitchell et al., 2016). SWEA is a hemispheric electrostatic analyzer designed to measure electron fluxes for energies ranging from 3 ev to 4.6 keV, such that it captures both ionospheric photoelectrons and solar wind electrons. These fluxes are paired with magnetic field data supplied by MAG to produce pitch angle distributions and directional energy distributions, and SWEA's 360° by 120° field of view generally samples the complete range of pitch angles. Three-dimensional magnetic field measurements are provided at 32 Hz by MAG, which uses two triaxal fluxgate sensors.

Four years of MAVEN data are used in this study, from 01 December 2014 through 01 January 2019. During this time, MAVEN's precessing elliptical orbit allowed for data coverage across a wide range of local times, altitudes, crustal field strengths, and solar wind conditions. As this study is focused on the behavior of magnetic fields within the Martian ionosphere, we only use data measured below 500 km altitude. We also impose a lower limit of 200 km altitude to ensure that we generally stay above the electron exobase, where our method of identifying topology breaks down. Additionally, we only use data for which the electron pitch angle distribution had some data coverage within thirty degrees parallel and antiparallel to the field, as these field-aligned fluxes are a primary component of our method of topology identification.

4.3.3 Interplanetary Magnetic Field Measurements

As with the MGS results, we separate our MAVEN data into periods of duskward and dawnward IMF. We sort the data based on orbit-averaged measurements of the IMF, using data sampled by MAG for all times when MAVEN was located outside of the sheath. Orbits during which MAVEN did not directly sample the solar wind are excluded from this study. From these orbit-averaged measurements, we calculate IMF clock angles, where a clock angle of 0° corresponds to the +Z direction and 90° corresponds to the +Y direction in the MSO frame. We classify the IMF direction as duskward when the clock angle falls between 10° and 170° and dawnward when the clock angle falls between 190° and 350°.

4.3.4 Results

With this set of analysis tools from MAVEN, we can investigate our explanation for the results we observed with MGS. To explore our prediction that there should be reversed trends on opposite sides of the current sheet, we present Figure 4.3a, which studies cusp response to IMF direction as a function of local time. Because we are specifically investigating crustal field variations here, we prune our data to only include measurements where the modeled crustal field strength was greater than 15 nT at MAVEN's location. In order to make a direct comparison to our MGS results, we plot the same quantity here as in Figure 4.1b. However, MAVEN's data coverage isn't yet sufficient at all geographic locations for us to produce a comparable map, so we instead plot this as a function of crustal field elevation angle. The behavior of cusps directed outward can therefore be found on the right half of the plot, and that of cusps directed inward on the left half of the plot.

The results are then divided into two local time segments, corresponding to rough boundaries for the two lobes of the magnetosphere. The blue line (local time 0-6) represents the same region of space as was sampled by MGS, and it shows the same trend. Outward cusps are closed more often during periods of duskward IMF, while inward cusps are closed more often during periods of dawnward IMF. For the orange line (local time 18-24), which represents the opposite side of the

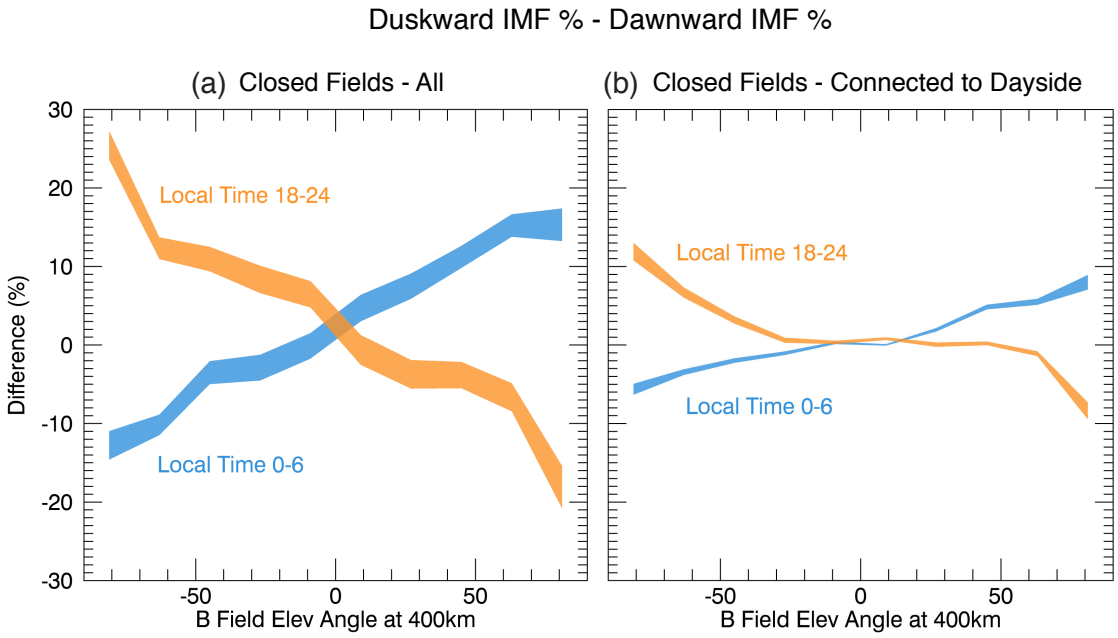

Figure 4.3: (a) The difference in how often closed topology was observed during periods of duskward and dawnward IMF (the same quantity as in Figure 4.1b), plotted as a function of crustal field elevation angle. (b) The same quantity, but only considering closed fields that are connected to the dayside of Mars, as determined by the presence of photoelectron signatures.

current sheet from MGS, this trend is reversed. Outward cusps are closed more often during periods of dawnward IMF, and inward cusps are closed more often during periods of duskward IMF. This dependence on magnetotail direction is consistent with our hypothesis that the cusp phenomenon observed involves reconnection with tail fields.

We next investigate our suggestion that these reconnecting fields should frequently end up connected to the dayside of the planet. To verify this, we make use of the fact that our method for identifying topology uses photoelectron energy signatures to determine whether a field line is connected to the dayside ionosphere. This allows us to distinguish between closed field lines on the dayside and nightside, and here allows us to determine whether these cusp fields are connected to the dayside of Mars. In Figure 4.3b, we use the same format and same set of data as in Figure 4.3a, but this time only labeling fields as "closed" if they connect to the dayside of Mars. The trend we are investigating remains clearly visible, with the variations being slightly reduced in size. This suggests that a sizeable fraction of the variations we observe are due to field lines reconnecting to the dayside of the planet. For example, we see in Figure 4.3a that during duskward IMF, cusps directed vertically inward at local time 18-24 are closed 20 percentage points more often than during dawnward IMF. By comparison to panel b we can see that half of this variation (10 percentage points) is due to connections to the dayside of Mars. The remaining half of the variation is therefore due to closed loops forming that are connected solely to the nightside.

4.4 Discussion and Conclusion

The results shown in this paper hold several implications worth noting. First, incoming IMF direction directly influences which crustal field cusps are open or closed to the solar wind. While we would expect that the IMF should interact with crustal fields regularly, the fact that cusps on the nightside are also greatly influenced by IMF direction is a reminder that the entire Martian system is extremely susceptible to changes in upstream conditions, and that these crustal magnetic sources are malleable at all locations around the planet. The relationship we demonstrate between IMF direction and cusp topology could also help inform modeling efforts at Mars, particularly any

that are interested in mapping plasma flows all the way down to the planet's ionosphere.

Second, because cusp topology appears to depend on magnetotail field direction, it is likely that many cusps transition between closed and open as they rotate through the nightside and encounter both tail lobes. This suggests that cusp regions are dynamic on a daily or hourly timescale, potentially experiencing a convective cycle of sorts. The current sheet in particular would be a region where many topological changes might occur, as it represents the transition between the tail lobes. This could potentially lead to energetic processes and enhanced particle outflow in this area.

Third, crustal field cusps on the nightside are frequently connected to the dayside via large-scale closed loops. This adds another dimension to the results found in the weakly magnetized northern hemisphere by Xu et al. (2016). As discussed in that paper, magnetic connections to the dayside ionosphere act as source of localized energy input in the form of precipitating electrons. This should lead to increases in particle ionization rates and temperatures, and could be a source for the low energy discrete aurora observed by Mars Express (Leblanc et al., 2006), all of which could potentially drive ion outflow. Cusp regions in particular, more than weakly magnetized regions, should channel energy input from the dayside into small areas, while also containing the vertically oriented magnetic fields that are particularly conducive to particle escape (e.g Ergun et al., 2016). It is also important to note here that although these field lines are topologically closed in the context of electron transfer, most ions are not expected to be constrained in the same way. Those that travel into these large closed loops, either from the dayside or the nightside, will likely have gyroradii on the order of tens of kilometers, and could easily drift onto other field lines that may or may not lead back into the Martian ionosphere.

Finally, in this paper we only considered crustal fields on the nightside of Mars, but we expect that those on the dayside should also respond significantly to IMF variations. This response should be very different, however, as the dayside interaction with the IMF is a situation unlike that on the nightside. Draped lines of IMF are pressed down to low altitudes, interacting directly with the loop tops of closed crustal fields. Reconnection between draped fields and these loop tops is

expected to occur frequently, and could lead to variations in crustal field size and location. We also note that throughout much of the strong crustal field anomaly, these loop tops have a north-south orientation. This means that it may be the north/south component of the IMF (rather than the duskward/dawnward component) that has the largest influence on dayside crustal field topology, a prediction that could be examined through future data analysis and modeling studies.

Chapter 5

Ion escape from crustal fields

5.1 Analyzing ion escape at Mars

As discussed in section 1.4, ion escape from Mars can occur through a variety of different channels and processes. Broadly speaking, all forms of ion escape involve the completion of three conditions. First, the presence of ions is required (an obvious detail, but an important one). Second, these ions need to be energized such that they reach escape energy. Third, the escaping ions must have a viable, unhindered path through which they can leave the system. In other words, the **supply**, **energization**, and **transport** of ions each play an important role in driving ion escape at Mars. Each of these steps could represent a bottleneck for escape under certain conditions. If the supply of ions through ionization is low, then escape rates will be low regardless of how much energy is delivered to the system. If many ions are created but energy input is low, then few will reach the velocities necessary to leave the planet. And even if many ions are brought to escape energy, they still might fail to be transported out of the system, perhaps due to the loss of energy through collisions or the presence of magnetic fields hindering their escape.

In this study, we use this three-step framework to analyze ion escape at Mars. Using data from the MAVEN spacecraft, we analyze the supply, energization, and transport of ions in the Martian system. We interpret this information specifically in the context of understanding how these processes are affected by the presence of crustal magnetic fields. We then use our understanding

to estimate the extent to which crustal magnetic fields influence ion escape at Mars, reaching an initial result for what was the primary motivation behind the work in this thesis.

In section 5.2, we discuss the data products and instruments used in this study. In section 5.3, we present results regarding the supply, energization, and transport of ions on the dayside of mars. In section 5.4 we present comparable results for the Martian nightside. In section 5.5 we link our dayside and nightside analyses together through a study of variations with solar zenith angle. In section 5.6, we calculate the effective magnetization of ions at Mars, so as to determine the applicability of our topology analysis. In section 5.7 we provide a condensed summary of our results thus far. In section 5.8, we use the previous results to formulate estimates of crustal field influence on Martian ion escape. And in section 5.9 we summarize our findings and discuss their associated implications.

5.2 Data and instrumentation

The ion densities and fluxes used in this work were measured by the Suprathermal and Thermal Ion Composition (STATIC) instrument aboard MAVEN. STATIC is an electrostatic analyzer that also makes use of time-of-flight analysis to measure ion fluxes across a range of masses (1 - 70 amu), energies (0.1 eV - 20 keV), and look directions (360° by 90°). Here we use measurements from the instrument's D1 mode of operation, which samples particle distributions across 32 energy bins, 8 mass bins, and 64 directional bins. Our analysis uses three and a half years of data, spanning from April 14, 2016 through Sept 2, 2019. Data sampled below 200 km altitude are excluded from this study due to ion suppression issues that cause unreliable measurements in that region. Each individual measurement represents an instantaneous ion distribution function that is then corrected for both spacecraft velocity and spacecraft potential, with measurements of spacecraft potential coming from a combined routine that uses information from the SWEA, STATIC, and LPW instruments. Moments of the distibution are then taken to obtain ion densities and fluxes.

In this study we also use vector magnetic field measurements from the Magnetomenter (MAG) instrument, as well as calculations of magnetic topology that were made using data from both

MAG and the Solar Wind Electron Analyzer (SWEA) instrument. A description of our method for identifying magnetic topology, as well as descriptions of the instruments involved, can be found in section 3.2.

5.3 Dayside Results

We begin our analysis on the dayside of Mars, using measurements taken between 0° and 90° solar zenith angle.

5.3.1 Supply

In Figure 5.1 are shown geographic maps of O_2^+ density on the dayside of Mars. The altitude range included in each panel increases linearly from 200 km altitude in the upper left to 900 km altitude in the lower right. As one would expect from a typical ionospheric profile, the density of O_2^+ decreases with altitude, and we can also see that at higher altitudes there are geographic variations in density that appear to correspond to crustal field locations. In the lowest altitude bin (200 - 288 km), O_2^+ densities are fairly uniform across the planet, but at the higher altitudes we see that densities are largest in the strong crustal field regions.

Unfortunately, these maps suffer from relatively low data density. Many of the longitude-latitude bins contain only 10-20 points, and statistical noise seems fairly prevalent. In the context of this study, however, we are less interested in distinguishing between specific crustal field structures than we are in understanding the general trends that separate magnetized and unmagnetized regions of Mars. To that end, Figure 5.2 contains plots of ion density as a function of altitude, crustal magnetic field strength, and magnetic elevation angle. In Panels (a) and (b) are shown O_2^+ densities, while in (c) and (d) are O^+ densities. For both ion species, we observe the same trend seen in Figure 5.1. At low altitudes (near 200 km), ion densities of $\sim 10^4$ cm^{-3} are observed consistently across all magnetic field strengths. This is to be expected, as these ions are primarily created through photoionization, a process that is unaffected by local magnetic fields. Moving to higher altitudes, we can see O_2^+ densities decrease, and that this decrease is more gradual in regions

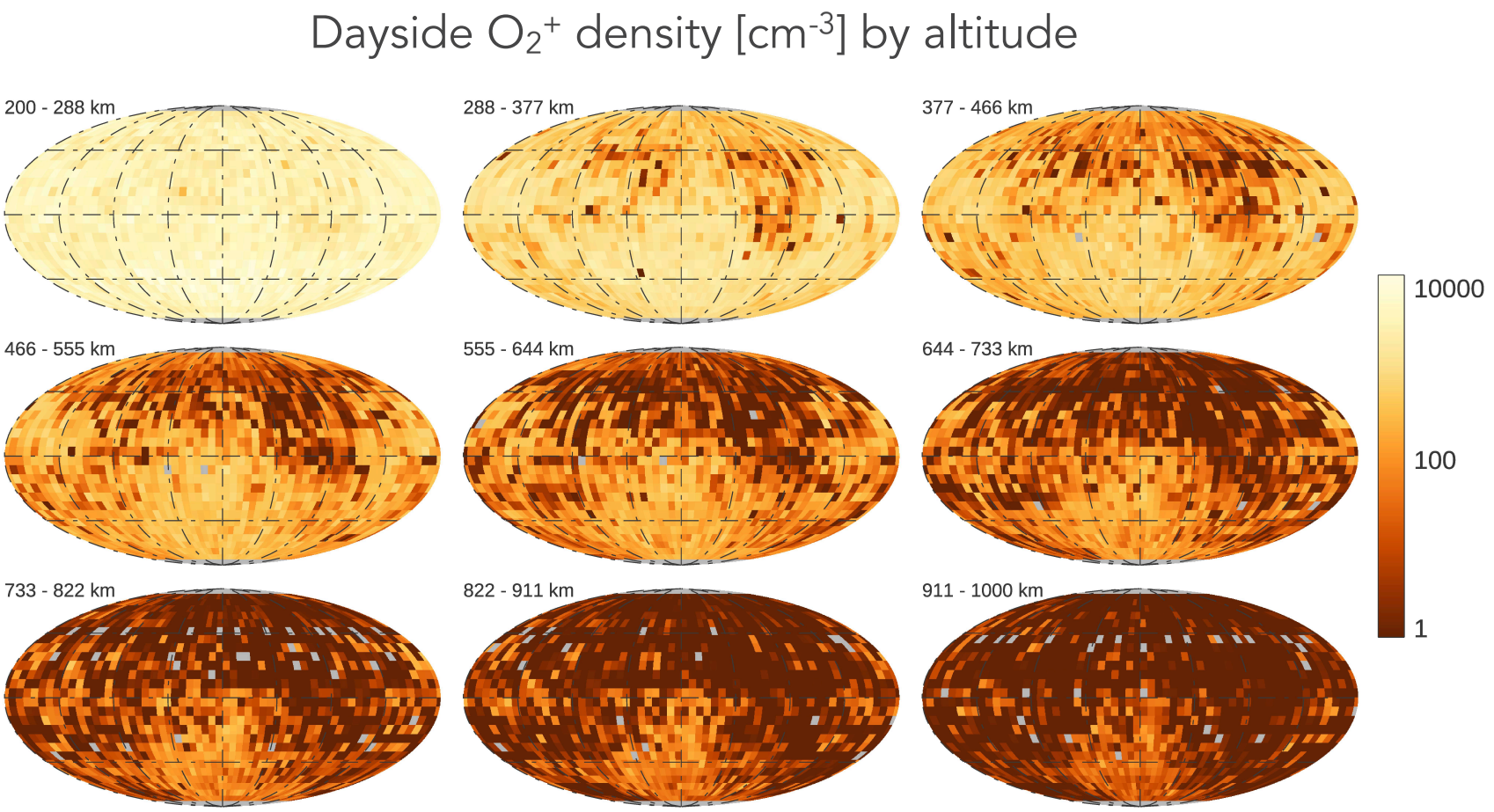

Figure 5.1: Geographic maps of O_2^+ density on the dayside of Mars at nine different altitudes. Each panel has an x-axis of east longitude and a y-axis of latitude. The altitude steps are linearly spaced between 200 and 1000 km. Bins with fewer than 10 points are colored gray.

of strong magnetic field. As a result, at any given altitude above 300 km we observe higher ionospheric densities in crustal field regions than we do in unmagnetized regions of Mars. This result was previously observed using MARSIS radar soundings by Andrews et al. (2015), though that study was unable to make measurements below 350 km altitude. They suggested that the vertical fields associated with crustal field structures allow for increased transport of particles to the upper ionosphere, whereas ions in unmagnetized regions are constrained to low altitudes by horizontal induced magnetic fields. Here we support this interpretation, and suggest that in addition to transporting ionospheric plasma up to high altitudes, strong crustal fields are also likely able to effectively trap and recycle ions. Since collisions are unlikely above the exobase, many ions at this altitude will mirror within the field, remaining trapped in the crustal field structure until they are scattered into the loss cone or diffuse to high enough altitudes to encounter the solar wind. This leads to a build-up in density, as was reported by Lundin et al. (2011) and Nilsson et al. (2011). These authors used Mars Express observations to make global maps of ion densities and fluxes, respectively, at Mars.

In panels (a) and (c) of Figure 5.2 we can also see a particularly steep drop off in ion density that occurs at $\sim 500 - 600$ km altitude in weakly magnetized regions, rising up to ~ 1000 km altitude in strongly magnetized regions. This drop off represents the transition region between the Martian ionosphere and the solar wind. Over years of study, this boundary has been referred to by a bevy of different names, each relating in some way to the physical transitions occurring at this location. Below this boundary lie ionospheric plasma and induced magnetic fields, while above it we primarily find shocked solar wind protons and a pileup of interplanetary magnetic field. As such, it is sometimes referred to as the ion composition boundary or the magnetic pileup boundary (see Espley, 2018, for a full discussion of terminology). In this work we will refer to it by the catch-all term "induced magnetosphere boundary" (IMB), as it was labeled in Figure 1.5b.

In Figure 5.2 we can see how crustal fields affect the altitude of the IMB. Strong crustal fields deflect incoming sheath plasma at high altitudes, pushing the boundary further from Mars and allowing ionospheric plasma to extend up to 1000 km altitude. This finding is in agreement with

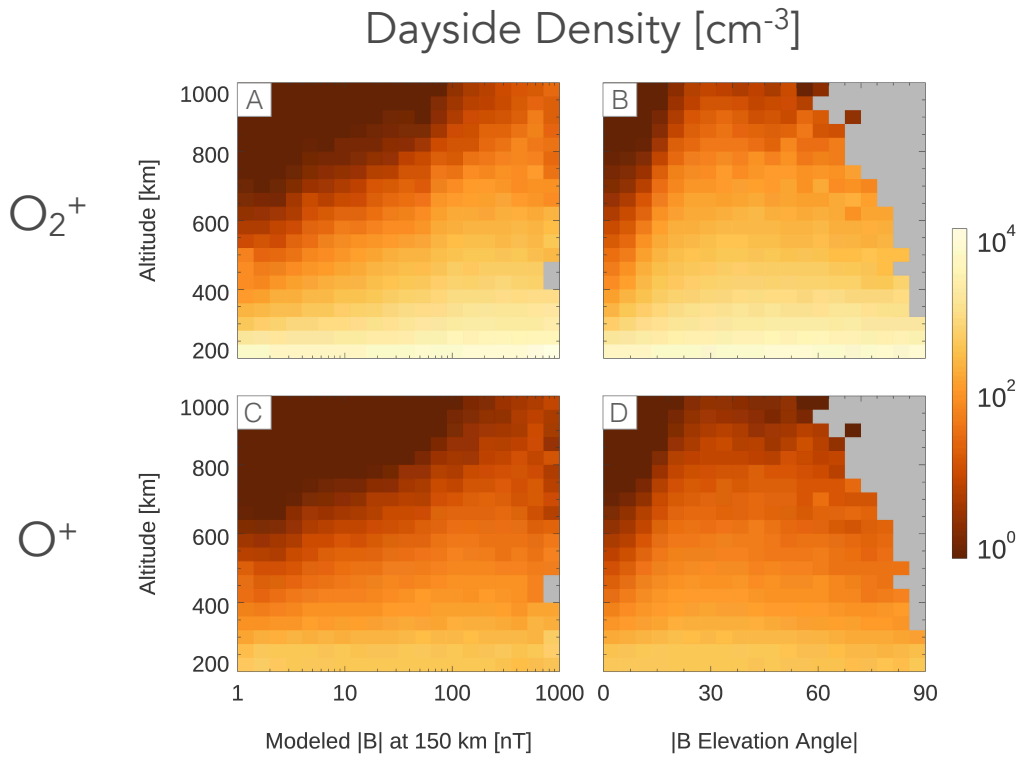

Figure 5.2: Density of O_2^+ (top row) and O^+ ions (bottom row) on the dayside of Mars. In the left column, plots are a function of altitude and crustal magnetic field strength as modeled at a reference altitude of 150 km by the Morschhauser model (Morschhauser et al., 2014). In the right column, plots are a function of altitude and magnetic elevation angle, with the latter running from 0° (horizontal fields) to 90° (vertical fields). Bins with fewer than 50 points are colored gray.

previous studies, several of which have found large asymmetries in the altitude of the IMB between the strongly magnetized Southern hemisphere and the weakly magnetized Northern hemisphere (Fang et al., 2017; Matsunaga et al., 2017). A similar result was also reported by Brain et al. (2003), who showed that these variations also occur on a local scale around crustal field structures.

5.3.2 Energy

To study where ions at Mars gain enough energy to escape the planet, we present Figure 5.3. Using the same axes and organization as Figure 5.2, this figure contains plots of the flux of ions traveling upward with escape energy on the dayside of Mars. Here we once again see the effects of IMB in the top left of each of the four panels. Fluxes of ionospheric particles are primarily found below the IMB, as the sheath plasma located above is composed primarily of protons. If we compare the IMB as mapped out in Figure 5.2 to what we see in Figure 5.3, we find small fluxes of energetic ions extending out past the boundary. Ions that make it to these altitudes are a primary source for ion pickup (see section 1.4.6), and are all likely to escape the planet provided that they do not collide with the planet as they are carried away by the solar wind.

Below the IMB, we find high fluxes of energetic ions, and here we observe differences in the energization of O^+ and $O_2{}^+$. O^+ ions reach escape energy fairly uniformly across all crustal field strengths, and appear to typically be sufficiently energized even at our lowest sampled altitude of 200 km. This means that very quickly upon reaching the exobase, O^+ is accelerated to escape energy. Here we do not identify a definite source for this energization, but suggest that much of it is likely due to field-aligned electric potentials, which have been measured throughout the Martian ionosphere. Xu et al. (2018b) and Collinson et al. (2019) used electron energy spectra measured by MAVEN to infer the magnitude of field-aligned potentials at Mars, determining that potential drops on the order of -1.0 V to -1.5 V exist around the planet. The authors of those studies did not distinguish between source mechanisms, but suggested that ambipolar electric fields are likely the primary driver. The field-aligned potentials were also found to be strongest near the ion exobase, where they could play a role in pulling ions out of the collisional atmosphere and toward escape.

Here we potentially see the result of this process, with O^+ traveling upwards at escape energy across the planet.

O_2^+ ions, however, only acquire escape energy upon reaching higher altitudes, as shown in panels (a) and (b). At 200 km altitude, outward fluxes of O_2^+ ions with escape energy are comparatively low. Only upon reaching ∼300-400 km altitude do the ions begin reaching escape energy. It makes intuitive sense that O_2^+ ions would need to be accelerated over a larger distance than O^+ ions to reach escape energy, as their escape energy is twice as large. Moreso, a 1.5 V field-aligned potential drop alone is unable to provide the ∼4 eV required for O_2^+ escape. However, even a moderate potential drop of ∼0.5 eV is able to loft ions upward past the exobase to higher altitudes where they can gain energy through plasma waves and other heating mechanisms, as was suggested by Ergun et al. (2016). We suggest that such a process is likely happening here, and that these heating mechanisms are able to bring O^+ to escape energy more quickly than O_2^+ upon their motion to higher altitudes.

In Figure 5.3a we also find that O_2^+ fluxes vary substantially with crustal field strength. Specifically, fluxes in crustal field regions (>20 nT) are higher than those in the unmagnetized regions, and the altitude at which this flux enhancement occurs moves upward with increased crustal field strength. In the strongest crustal field regions (500 - 1000 nT), peak energetic O_2^+ fluxes are found near 1000 km altitude, just below where these crustal fields stand off with the solar wind. For the more middling strength crustal fields (∼50 nT), peak fluxes are found at 500 km altitude, once again just below where these fields interface with the IMB. In general, we see here that the loop-tops and outer edges of crustal field structures show enhanced ion fluxes, while the inner, low-altitude sections of crustal field structures remain relatively unenergized.

The resulting situation looks somewhat similar to that of electrons trapped in crustal fields on the nightside of Mars. In that circumstance, the outer edges of crustal field structures are filled with mirroring energetic electrons, while the inner sections are severely depleted of particles. In the case we observe here, a strong supply of ions exists throughout the entire crustal field structure (as seen in figure 5.2), but on the outer edges the particles are much more energetic and more likely to

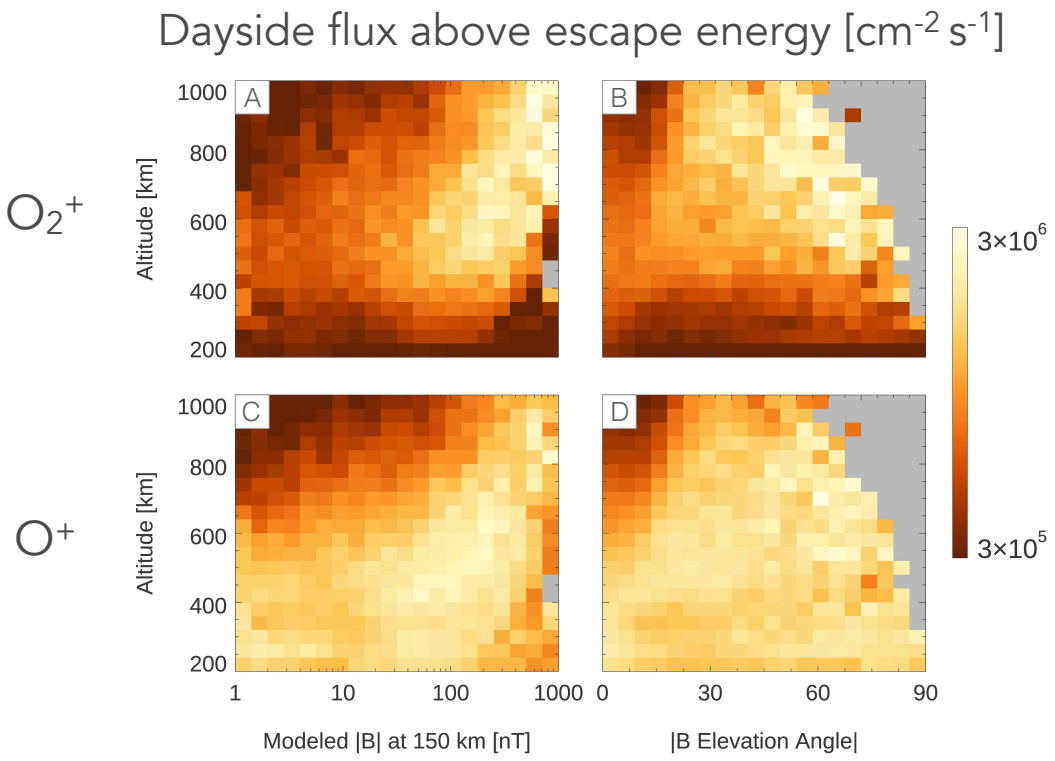

Figure 5.3: Flux of ions traveling upward on the dayside of Mars with energy in excess of the local escape energy. Plots are organized in the same manner as in Figure 5.2.

reach escape energy. We suggest two possible causes for this trend. First, it may be that only the high energy tail of particles found within the crustal fields are able to diffuse upward to the outer edges, while low energy ions bound to the central loops of a field structure are confined to stay there. Second, particles that reach the outer edges of crustal field structures are more likely to absorb energy from the incoming solar wind. That is, crustal field loop-tops interface directly with shocked solar wind plasma, and particles located at these loop tops may be susceptible to energization via plasma waves (e.g Ergun et al., 2006), magnetic pumping (e.g. Lundin and Hultqvist, 1989), or other such heating mechanisms. The true cause may, of course, be a combination of these two hypotheses. Upon close inspection, a similar enhancement can be seen in the O^+ fluxes in panel c, though it is less exaggerated due to the generally higher fluxes exhibited by that particle species.

In addition to the heating mechanisms mentioned above, some fraction of the flux we observe in strong crustal field regions was likely accelerated by the large field-aligned potentials that have been observed in crustal field cusps. Xu et al. (2020a) provided case studies of field-aligned potential drops in excess of 200 V that were associated with observations of discrete aurora. Potential drops of similar magnitude in crustal field cusps were estimated by (Dubinin et al., 2008). These potential structures should be able to bring oxygen ions far above escape energy, driving large fluxes as they do. However, it is currently unclear how frequently potentials of this magnitude occur at Mars, so we do not speculate here on the extent to which they are responsible for the ion fluxes shown in Figure 5.3. We can posit, however, that most of the escape flux driven in this way would be located on more vertically oriented crustal fields, and thus may be responsible for the flux enhancement we observe at high altitudes and high elevation angles in the upper right of Figure 5.3b. This section of the parameter space contains some of the highest $O_2{}^+$ fluxes we observe on the dayside, despite hosting comparatively low $O_2{}^+$ densities in Figure 5.2. This suggests that the particles traveling through this region are very highly energized.

5.3.3 Transport

With maps of energetic ion fluxes in hand, we can now use our previous studies of magnetic topology to analyze whether these particles are likely to escape. Figure 5.4 contains plots of the frequency of observing specified field topologies on the dayside of Mars. Plots are organized using the same axes and layout as in the previous two figures, but in this case the rows correspond to closed and open topology, rather than to different particle species. Note that the plots of closed and open field frequencies use different colorbars. The method of topological analysis used here is the same as in Chapters 3 and 4, and is described in full detail in Xu et al. (2019).

On the dayside, closed fields are more common at low altitudes and in strong crustal field regions. In fact, at our lowest studied altitude of 200 km, fields are almost uniformly closed across the dayside. This is a somewhat surprising result that was initially outlined by Xu et al. (2017a). In interpreting this finding, it may be imporant to recall that our method of identifying topology determines whether field lines are connected to the collisional atmosphere, rather than to crustal field sources locked the planet's surface. This means that many of the closed fields we observe at 200 km may truly be draped or induced field lines that thread through the collisional atmosphere multiple times. When we sample a field line of this kind while between its two points of connectivity, we observe a field that is closed in the context of electron transport. At higher altitudes, we would expect that it would become more common for these draped and induced fields to only thread through the atmosphere once, causing an increase in open field topology. We can see this feature in Figures 5.4a and 5.4c, where we find transition region located between 300 and 600 km where open field topology becomes more common. The altitude at which this transition occurs increases with increasing field strength, and by comparing this to our previous analysis of the IMB location we can see that open field lines are found predominantly in an altitude band located between the IMB and low-altitude closed fields. This transition region is also where oxygen ion fluxes reach their peak values in Figure 5.3.

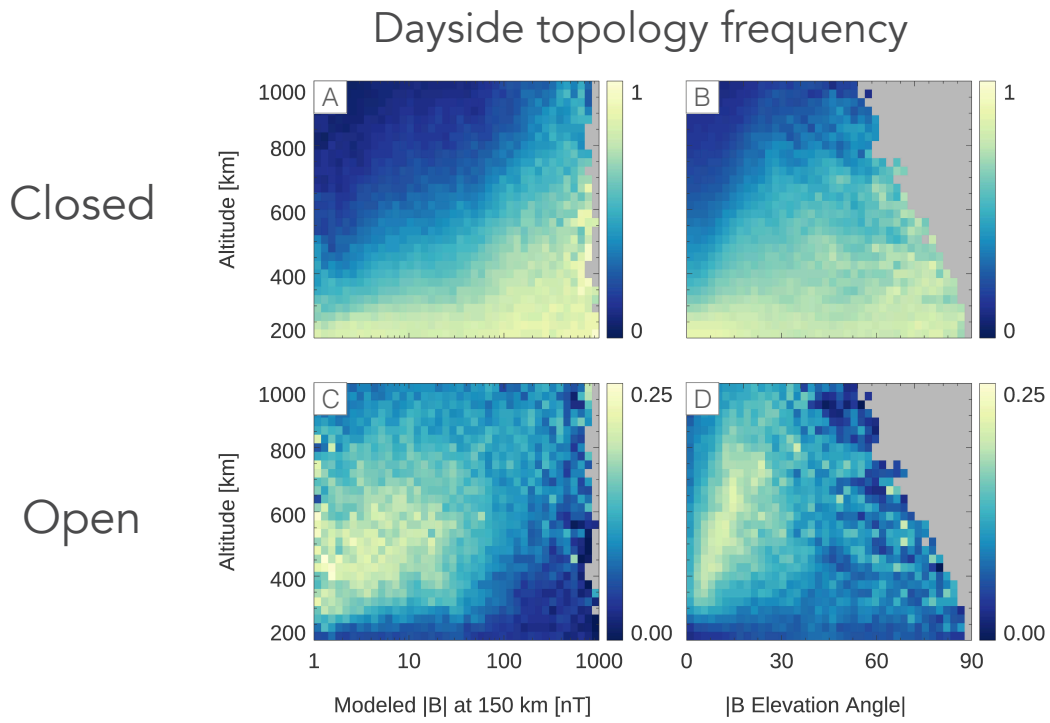

Figure 5.4: Frequency of observing specified topologies on the dayside of Mars. Plots are organized in the same manner as in Figure 5.2

5.4 Nightside Results

Turning to the nightside of Mars, we next present three figures using the same format as Figures 5.2 - 5.4. Once again we analyze density, flux, and topology, but this time only using data sample at solar zenith angles greater than 120°.

5.4.1 Supply

In Figure 5.5 we plot O^+ and $O_2{}^+$ densities on the nightside of Mars, where the supply of ions has a very different structure than on the dayside. Note that the these plots use a different color scale than those investigating the dayside in Figure 5.2; plasma densities are several orders of magnitude lower on the nightside. Immediately we can see that these plots show a much weaker dependence on altitude. Across the full altitude range, nightside densities vary only from ∼10 - 60 cm^{-3} for $O_2{}^+$ and from ∼1 - 5 cm^{-3} for O^+, as compared to the several orders of magnitude variation observed on the dayside. This ionospheric structure is in agreement with Fowler et al. (2015), who showed that above 200 km nightside electron densities measured by LPW are roughly constant with altitude. That study also showed that a modest nightside ionosphere is sustained at low altitudes (<200km) by precipitating electrons. Though our observations are unable to extend to such low altitudes, we can see the edge of this feature at the bottom of our $O_2{}^+$ plots. Near 200 km in panels (a) and (b) we see a slight enhancement in $O_2{}^+$ density, and from panel (b) it seems that this enhancement is most prominent on vertically oriented fields. These fields (particularly those associated with crustal field cusp regions) are the most likely to facilitate precipitation of electrons into the nightside atmosphere, and here we see traces of the resulting production of ions through impact ionization.

Figure 5.5 illustrates that the nightside of Mars has a sparse and tenuous ion population, with low densities of ions flowing away from the planet fairly uniformly. The lack of any incoming solar wind pressure on this side of the planet means that particles are not compressed down to low altitudes as severely as on the dayside. The relatively weak ionization source, however, means that

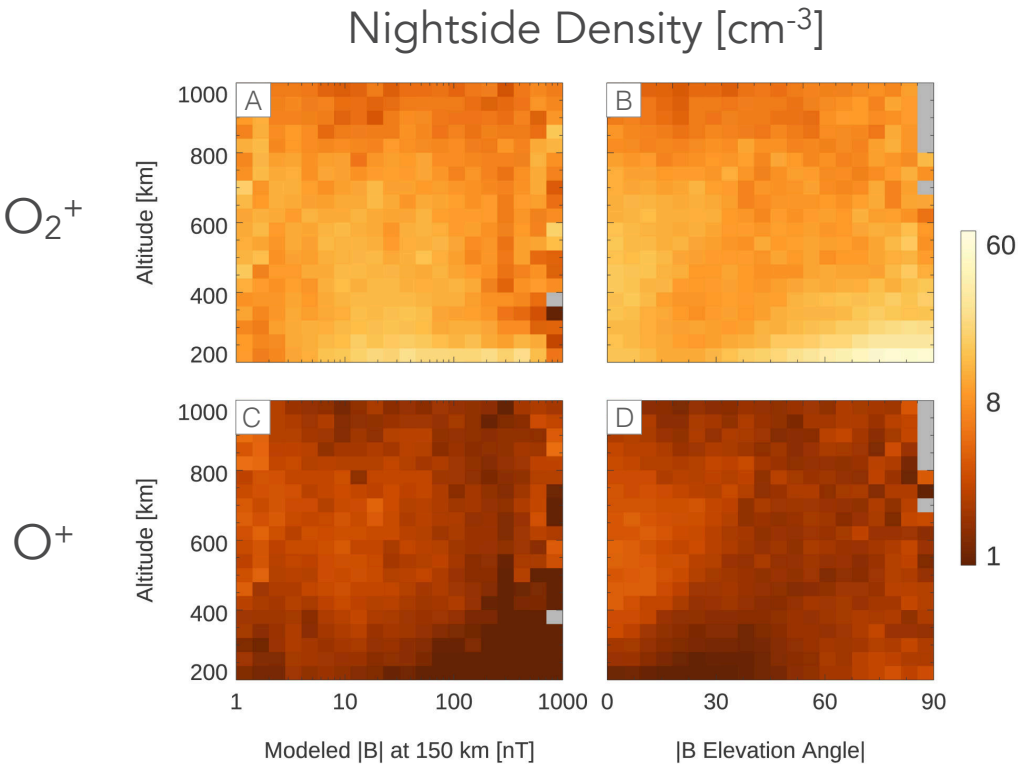

Figure 5.5: Density of O_2^+ and O^+ ions on the nightside of Mars. Plots are organized in the same manner as in Figure 5.2.

ion densities remain low across all altitudes, particularly above the exobase.

Here we should also note that although these observations are taken on the nightside of Mars, the ions that we measure at high altitudes did not necessarily originate in the nightside ionosphere. As ions flow away from Mars, they are pushed in the antisolar direction by the solar wind. Particles from the dayside frequently flow around Mars and into the nightside magnetotail, where they are measured as nightside ions. We can see signatures of this flow in Figure 5.5 particularly in panels (b) and (d). While the lower right corners of these plots show enhanced densities due to electron precipitation along vertical fields, there is a separate slight enhancement found along the left sides of these plots. Moving to higher altitudes, this enhancement can be found at steeper and steeper elevation angles. This corresponds to magnetic fields that drape around the planet and extend directly down the magnetotail, many of which carry ions flowing from the dayside. At low altitudes near the terminator, draped fields are nearly horizontal to the planet, but as they extend downtail they become increasingly vertical relative to the surface below them. Ion densities on these field lines do not appear to be appreciably larger than they are throughout the rest of the nightside, but ion density alone does not provide us information on particle escape. We therefore next analyze the energy and flux of these particles.

5.4.2 Energy

As shown in Figure 5.6, fluxes of O^+ and $O_2{}^+$ ions on the nightside of Mars display very similar behavior. At low altitudes, fluxes at escape energy are low, despite the $O_2{}^+$ density enhancement due to precipitating electrons that was observed in Figure 5.5. Moving to higher altitudes, particles are eventually accelerated to escape energy, and by 300-400 km altitude we see an increase in escaping fluxes at all crustal field strengths. In strong crustal field regions, appreciable $O_2{}^+$ escape fluxes are observed at a lower altitude than in the non-crustal field regions, likely due to the aforementioned higher supply found in those locations.

As on the dayside, many escaping oxygen ions are likely accelerated via field-aligned potentials. Since there is no standoff with the solar wind on this side of the planet, upward traveling ions

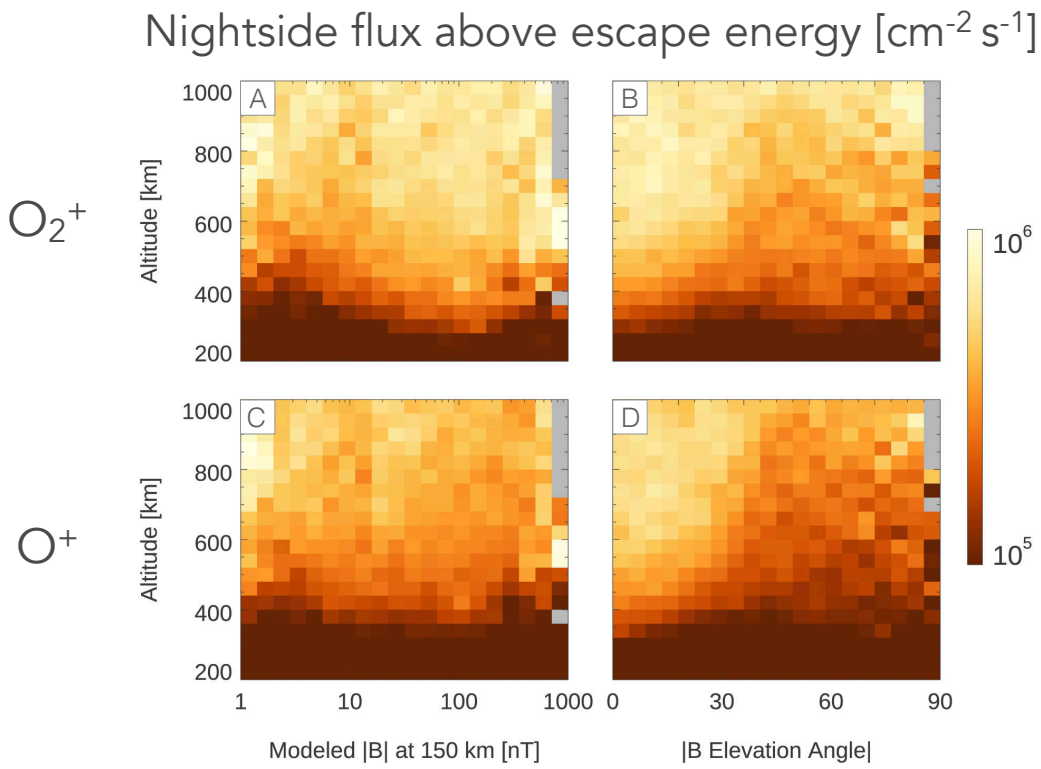

Figure 5.6: Flux of ions traveling upward on the nightside of Mars with energy in excess of the local escape energy. Plots are organized in the same manner as in Figure 5.2.

that reach escape energy are able to flow downtail unimpeded, creating a steady flow of ions up through our highest analyzed altitude of 1000 km. Just as in our plots of nightside ion density (Figure 5.5), little variation is seen with crustal field strength. We can however, see the same signature of dayside ion fluxes flowing tailward through the nightside that was noted previously. On the left hand side of Figures 5.6b and 5.6d, we see an enhancement of flux that moves to higher elevation angles as it reaches higher altitudes. These fluxes are carried on magnetic field lines connected to the dayside ionosphere that stretch directly downtail. Modeling studies have suggested that this may be an important pathway for ion escape (Liemohn et al., 2007b). By comparing the left and right sides of Figure 5.6b, we can make a direct comparison between fluxes sourced from the dayside and the nightside of Mars, respectively. For both O^+ and $O_2{}^+$, the fluxes coming from the dayside appear to be stronger by roughly half an order of magnitude. This is in agreement with previous maps made using Mars Express measurements of high energy ion fluxes (Nilsson et al., 2011). Our analysis extends this result to include particles that have only just reached escape energy.

5.4.3 Transport

In Figure 5.4 we present plots of the frequency of observing specified field topologies on the nightside of Mars. Here we find somewhat similar trends to those we observed on the dayside. Closed fields are found most frequently at low altitudes and in strong crustal field regions, while open fields are more common in weakly magnetized regions and at higher altitudes. Unlike on the dayside, open fields are found down through the exobase, particularly in weakly magnetized regions, and they also freely extend out through 1000 km altitude. Additionally, Figure 5.7 allows us to identify two separate populations of open field lines. At low altitudes, we can see one grouping of open field lines found with mostly horizontal elevation angles (0°), and a separate grouping of open field lines found at near vertical elevation angles (90°). As discussed in the previous two sections, these correspond to open fields connected to the dayside and the nightside of the planet, respectively. The fluxes observed for these two populations in Figure 5.6d appear to correlate well with open field line locations found throughout the nightside.

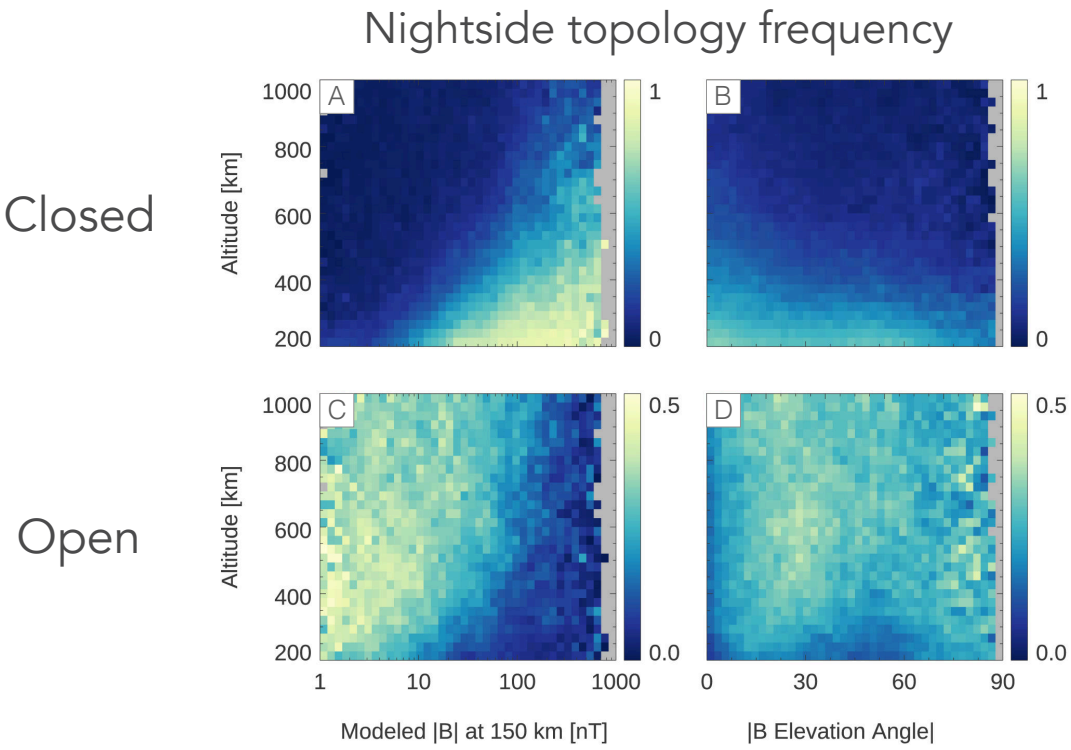

Figure 5.7: Frequency of observing specified topologies on the Martian nightside. Plots are organized in the same manner as in Figures 5.2

5.5 Trends with solar zenith angle

In order to link together our dayside and nightside analyses, we next present a set of plots that describe the supply, energization, and transport of oxygen ions as a function of altitude and solar zenith angle. This is shown in Figure 5.8. Here we observe a few noteworthy features. Densities and Fluxes on the dayside (0-90° SZA) are stronger than on the nightside (90-180° SZA) by an order of magnitude or more. The IMB is once again very visible, this time across a different set of axes. As has been documented in previous works, the IMB is closest to the planet at the subsolar point, flaring out at the planet's flanks. As in our dayside analysis, we find that just below this boundary lies a region of increased flux and open field lines that could potentially facilitate escape. Finally, we can once again see that densities, fluxes, and open field lines on the nightside all extend through the entirety of our sampled altitude range. This includes a band of enhanced ion density and flux that begins at 90° SZA and 200 km altitude, curving upwards and reaching 1000 km altitude at $\sim$ 120° SZA. This maps very closely to the path made by a line that extends directly tailward from the planet's terminator. We can interpret this band as representing dayside ions flowing around the planet and downtail on the nightside, tracing out the edge of Mars's geometric shadow.

5.6 Ion magnetization

In our analysis thus far, we have used information on magnetic topology to guide our interpretation of ion transport and escape. For example, we saw in Figures 5.3a and 5.3c that the highest ion fluxes on the dayside of Mars occur above strong crustal field regions. We find it unlikely that all of this flux is escaping, as closed topology is still found on 50% or more of the field lines measured in this region. These calculations of topology were made using electrons, however, and will not apply to energetic ion fluxes in all situations. We therefore find it necessary to analyze how well our definitions of "closed" and "open" truly apply to ions at this energy. Depending on the extent to which ion fluxes we measure are frozen onto the local magnetic field, the fraction of ions that are escaping could vary substantially.

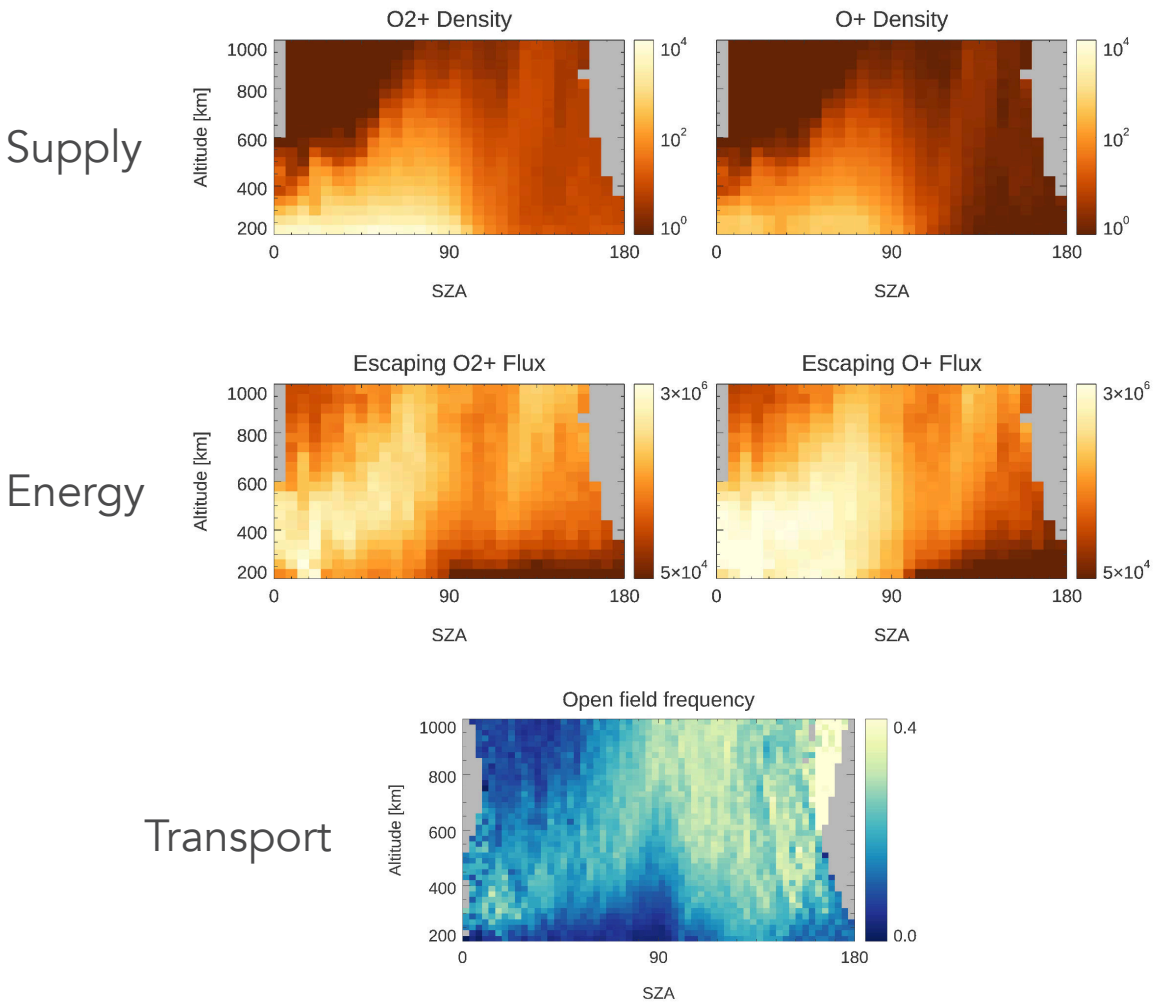

Figure 5.8: As a function of altitude and solar zenith angle, the supply, energization, and transport of O_2^+ and O^+ ions at Mars. This three-step framework for analyzing escape is discussed throughout this chapter. The top row contains plots of ion density. The middle row contains plots of ion fluxes traveling upward with escape energy. The bottom plot is shows the observation frequency of open field topology around Mars.

To determine whether gyrating charged particles are effectively bound to a magnetic field, we take a commonly used comparison between the particle gyroradius and the length-scale of the local magnetic field field. While there is no standardized definition for a magnetic field length scale, several previous studies have defined it as $L = |B|/|\nabla B|$, where $|B|$ is the magnitude of the magnetic field and $|\nabla B|$ is the magnitude of the *gradient* of the magnetic field (Büchner and Zelenyi, 1989; Zhang et al., 2016). Since $|\nabla B|$ is a tensor quantity, its magnitude is calculated using a norm, typically the L2 norm. In essence, the quantity L is therefore telling us what distance we would have to travel for the local magnetic field to change in magnitude by 100%, assuming its current rate of change remained constant. To estimate how effectively a particle is bound, we can then calculate R_g/L, where R_g is the particle's gyroradius ($mv_\perp/|q|B$).

To make this calculation, we use magnetic field data sampled by MAVEN throughout the Martian ionosphere across five years of observations (the same dataset as in Figure 1.6). This data was averaged into 2° longitude by 2° latitude by 80 km altitude bins, which were then used to calculate a 3-D vector gradient of the magnetic field. The L2 norm of this gradient was calculated for each bin to estimate the local length scale of the magnetic field. Next, we used the magnetic field magnitude in each bin to calculate the local gyroradius of an $O_2{}^+$ ion at escape energy (∼4 eV). This calculation assumed an average particle pitch angle of 45°. We then estimate particle magnetization as R_g/L. Values much less than 1 suggest that a particle is likely to follow magnetic field lines closely, often referred to as "magnetized", while values much greater than 1 suggest a particle is only weakly bound to the magnetic field, or "unmagnetized".

Here we note that by taking the ratio R_g/L, we are more specifically calculating the quantity

$$\frac{R_g}{L} = \frac{mv/qB}{B/\nabla B} = mv/q\frac{|\nabla B|}{|B|^2} \tag{5.1}$$

Since, m,v,and q are treated as constants in our calculations, we are essentially analyzing how $\frac{|\nabla B|}{|B|^2}$ varies throughout the Martian ionosphere. This quantity has a similar magnitude to the Grad-B drift of particles across magnetic field lines. Driven by gradients in the magnetic field, this

guiding-center drift moves with a velocity of

$$\vec{v}_{\nabla B} = \frac{1/2mv^2}{qB}\frac{\vec{B}\times\nabla B}{B^2} \tag{5.2}$$

It makes some intuitive sense that our estimate of particle magnetization would be reminiscent of this guiding center drift. After all, we are estimating the strength with which changes in magnetic field strength and direction cause particle trajectories to deviate from the path of a magnetic field line, the very situation that is described by Grad-B drift.

In Figure 5.9 we present geographic maps of $O_2{}^+$ magnetization, using a similar format as in Figure 5.1. At low altitudes, particles in strong crustal field regions appear to be highly magnetized, while outside of these regions particles are unmagnetized. Outlining the edges of the crustal field regions we can see the transition from magnetized to unmagnetized at $R_g/L = 1$, shown in white on this colorbar. At high altitudes (>800 km), $O_2{}^+$ particles at this energy are unmagnetized almost everywhere, with only the very strongest crustal field arcades showing some remaining traces of magnetization. In Figure 5.10, this data is instead presented as a function of altitude, magnetic field strength, and magnetic elevation angle.

Before comparing these plots to those made in previous sections, we should first address several caveats associated with this calculation. First, our analysis has only accounted for spatial variations in magnetic fields. Magnetic fields also vary in time, potentially quickly enough that any trapped ion might encounter different field topologies over the course of one 10 - 50 second bounce period. Second, we did not account for electric fields at all in this analysis, which in many circumstances are just as important if not more important than magnetic fields in the context of driving ion motion at Mars. Third, our calculation of gyroradius assumed the particles to have exactly escape energy, when in reality many of the fluxes we've observed were of higher energy than this by at least a factor of 2. Each of these three caveats has the effect of making particles less magnetized than we calculate here. This means that we should treat these plots as representing a lower bound to R_g/L (or as an upper bound to the extent to which these ions are magnetized).

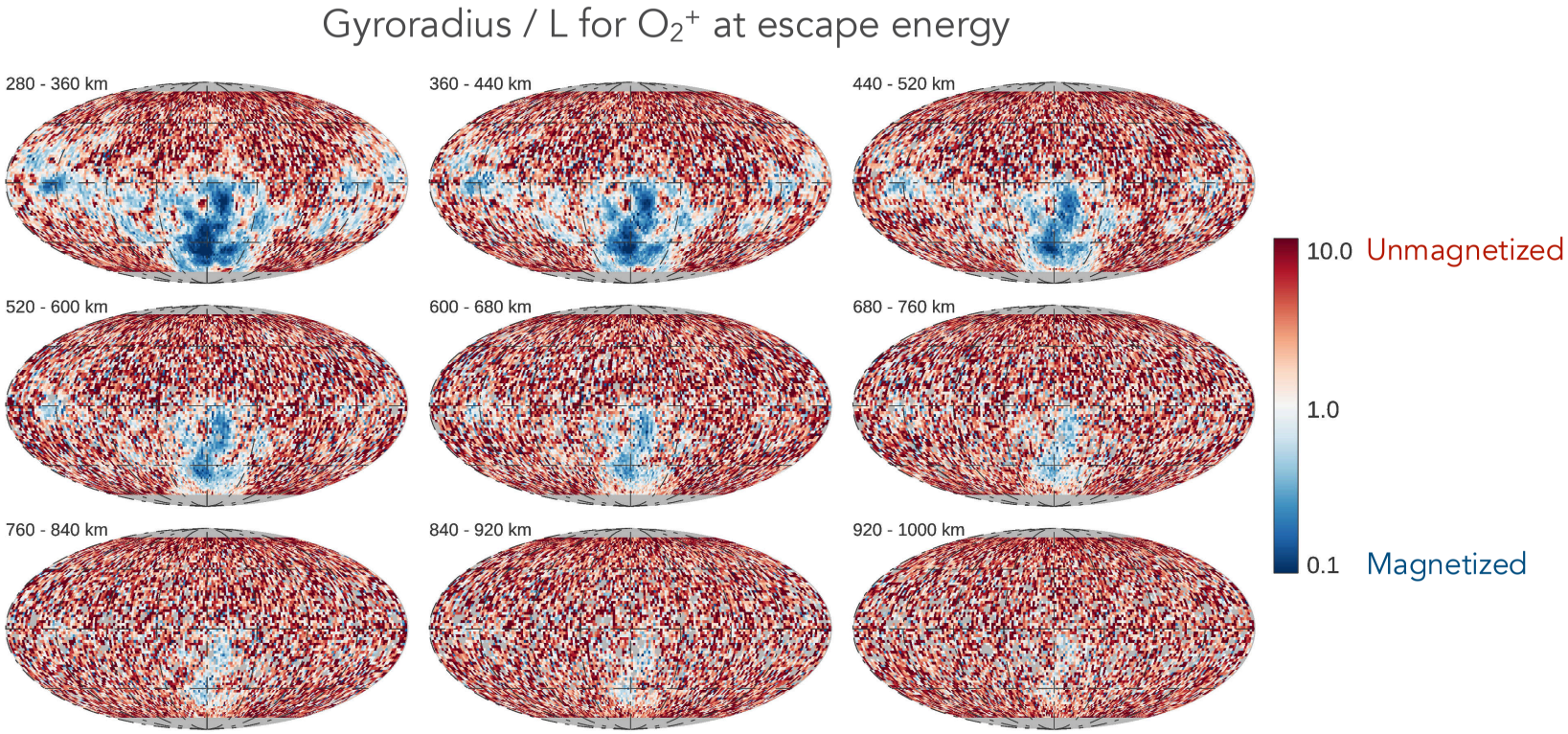

Figure 5.9: Magnetization of escaping O_2^+ ions at Mars, calculated through a comparison between ion gyroradius and the length scale of the local magnetic field. The gyroradius is calculated assuming that all of the ion's motion is directed perpendicular to the field. The length scale used here is the L2 norm of the vector gradient of the magnetic field, calculated using mission-averaged magnetic field maps measured by MAVEN (similar to those shown in Figure 1.6). Maps of magnetization are presented at nine different altitudes, linearly spaced between 200 and 1000 km. Bins with fewer than 10 points are colored gray.

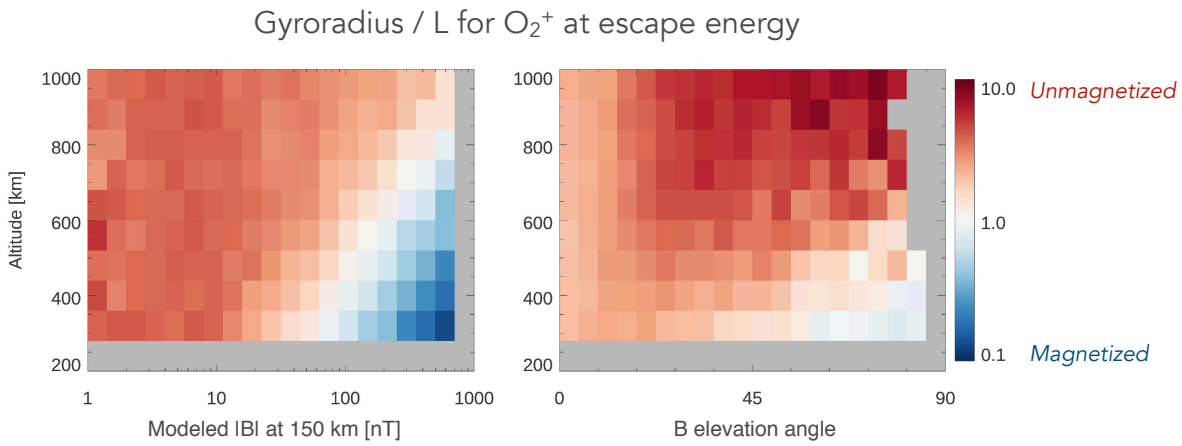

Figure 5.10: Magnetization of O_2^+ ions at escape energy, calculated through a comparison between ion gyroradius and the length scale of the local magnetic field. The figure on the left plots magnetization as a function of altitude an modeled magnetic field strength. The figure on the right plots magnetization as a function of altitude and local elevation angle, from 0° (horizontal fields) to 90° (vertical fields). Bins with fewer than 50 points are shaded gray.

With this in mind, Figure 5.10 illustrates that only in the strongest crustal field regions and at low altitudes are O_2^+ particles at escape energy effectively magnetized. This means that much of the flux that we analyzed in Figures 5.3 and 5.6 may be able to escape Mars, even if found on a topologically closed field line. This is not to say that field topology makes no difference – closed field lines are still likely to disrupt ion flows and impede escape – but particles are only truly frozen onto their local magnetic field in the center of strong crustal field structures. At the tops of these structures, the magnetic field becomes weak enough that particles are only slightly magnetized, if at all. More specifically, the band of white extending from 100 nT and 300 km altitude to 1000 nT and 800 km altitude signifies the transition to unmagnetized particles.

5.7 Interpretation

The slew of information provided in the preceding sections is summarized in the following main points:

(1) At low altitudes on the dayside, ion densities are uniformly high. Crustal field regions allow for the transport of these particles to higher altitudes, leading to local enhancements in density and flux. The escape of ions on the dayside therefore appears to be limited by energization and transport, rather than by supply.

(2) Just below the IMB and at the tops of crustal field structures, there is an interaction region where dayside ions readily gain escape energy. This region also marks a transition to increased open magnetic field topology.

(3) On the nightside, particles flow away from the planet more freely than on the dayside, with escape fluxes appearing wherever there are notable ion densities. This suggests that the escape of ions on the nightside is limited by supply, rather than by transport.

(4) Overall, escape fluxes from the nightside ionosphere appear to be significantly lower than those from the dayside ionosphere.

(5) Oxygen ions at escape energy are only strongly magnetized in strong crustal field regions at low altitudes. In regions of Mars containing no crustal fields, oxygen ions are only weakly affected by local field topology.

5.8 Estimates of crustal field contribution to ion escape

An overarching goal of the work in this thesis has been to use Martian crustal magnetic fields to estimate how strongly planetary magnetic fields influence ion escape. Here we present two calculations toward that end. The first is an estimate of the net effect that crustal magnetic fields have on global ion escape at Mars. The second is an estimate of the net effect caused by a single crustal field structure on ion escape in its local environment.

5.8.1 Global effect on ion escape of crustal magnetic fields

In Figure 5.3 we showed measurements of upward traveling ion flux above escape energy. Combining these measurements with our knowledge of topology and particle magnetization, we can construct a rough estimate of how crustal fields influence ion escape at Mars. For the purposes of this calculation, we divide the crustal magnetic fields of Mars into three groupings: weak fields (0 - 20 nT), medium fields (20 - 100 nT), and strong fields (100-1000 nT), where the nT values given here correspond to modeled field strength at 150 km (the x-axis in Figure 5.3a). For each of these groupings, we will calculate an estimate of ion outflow using measurements of fluxes, topology, magnetization, and the total surface area covered by that strength field.

From Figure 5.10, we can see that energetic ions found in weak field regions are substantially unmagnetized. We therefore take all of the upward flux measured at escape energy in those regions as successfully escaping the planet. Focusing on O_2^+ initially, we use fluxes measured between 400 and 600 km altitude for weak field regions, as this is the altitude range at which we observe ions typically reaching escape energy in Figure 5.3a. We find typical O_2^+ fluxes for weak field regions to be $\sim 6.5 \times 10^5$ cm^{-2} s^{-1}. For medium and strong field regions, we assume that particle escape is occurring near the top of crustal field structures, in the region of peak energization and increased

open topology that we discussed in previous sections. For medium strength fields, this corresponds to an altitude of 400-700 km, while for strong fields it corresponds to an altitude of 600-1000 km. In each of these regions, we assume that any upward flux measured at escape energy on an open field line is escaping. Flux measured at this energy on a closed field line, however, we take to only potentially be escaping, as Figure 5.10 suggests that these particles are still partially magnetized. To account for this, we assign each region a scale factor representing the fraction of escape energy flux on closed field lines that succeeds in escaping the planet. Combining the crustal field groupings, we then calculate total escape as:

$$\begin{aligned} Outflow =& F_1 A_1 \\ &+ F_2(open)A_2(open) + \alpha F_2(closed)A_2(closed) \\ &+ F_3(open)A_3(open) + \beta F_3(closed)A_3(closed) \end{aligned} \tag{5.3}$$

Here, the subscripts 1, 2, and 3 correspond to weak, medium and strong fields, respectively. ($Open$) and ($Closed$) specify the measured field topology. F represents ion flux, and A represents the area covered by fields of the specified strength. For example, $A_2(open)$ represents the area covered by medium strength fields with open topology, while $A_3(closed)$ represents the area covered by strong fields with closed topology. Finally, α and β are the factors that determine what fraction of flux found on closed topology escapes in medium and strong fields, respectively.

Results of this calculation are shown in Figure 5.11a, which provides $O_2{}^+$ escape rates as a function of α and β. We can see in this figure that even with $\alpha = 0$ and $\beta = 0$, we find an ion escape rate of $7 \times 10^{23}\,\mathrm{s}^{-1}$. This encompasses all escape occurring in weak field regions and on open field lines in medium and strong field regions. If we increase α from 0 to 1, effectively assuming that all ion flux at escape energy in medium strength field regions will escape, this raises the ion escape by a factor of 1.5 to $1.1 \times 10^{24}\,\mathrm{s}^{-1}$. From here, increasing β from 0 to 1 (assuming that all flux at escape energy in strong field regions escapes the planet) raises the total ion escape to $1.3 \times 10^{24}\,\mathrm{s}^{-1}$, a factor of 1.2 increase. This last increase in particular is a relatively small effect.

This is due to the fact that strong crustal fields as they are defined here only make up ∼10% of the Martian surface.

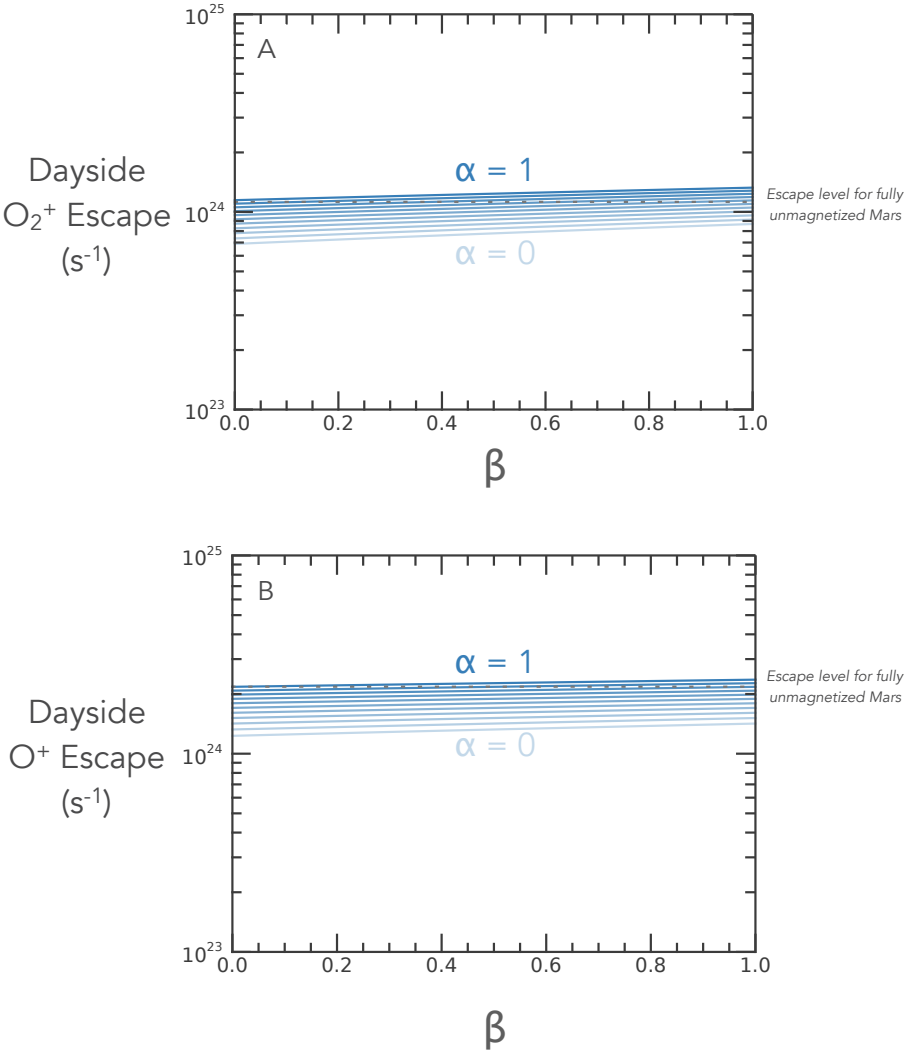

Figure 5.11: Dayside ion escape at Mars calculated through Equation 5.3. α represents the fraction of flux on medium strength closed fields that escapes, while β represents the fraction of flux on high strength closed fields that escapes. The horizontal dotted lines correspond to the escape rates that result from applying fluxes found in the low-strength field regions to the total area of Mars.

To estimate the net effect of crustal magnetic fields, we can now compare these results to the escape rate that would result if the entire planet was covered in low-strength fields. That is, we calculate $F_1 A_{total}$, a quantity that is plotted in Figure 5.11 as a horizontal dashed line. In this estimation, we see that ion escape is only increased by the presence of crustal fields if α and β are

both close to one. This seems unlikely, as this would mean that magnetic fields present virtually no obstacle to escaping ions at Mars. If we were to assume more conservative (though arbitrary) values of $\alpha = 0.5$ and $\beta = 0.2$, we would find an $O_2{}^+$ escape rate of $\sim 9 \times 10^{23}\,s^{-1}$, a 20% decrease in outflow from that of an unmagnetized Mars. This estimate agrees with previous modeling studies of the effects of crustal magnetic fields on Martian ion escape (Fang et al., 2010b; Ma et al., 2014; Fang et al., 2015).

Repeating the process described above for O^+ escape results in Figure 5.11b. The trends exhibited are almost identical, but with escape rates that are uniformly higher by a factor of $\sim$2. Once again, escape is only raised above that of an unmagnetized Mars if α and β are both close to one. In the case used above of $\alpha = 0.5$, $\beta = 0.2$, escape is decreased by 30% from the unmagnetized case. Note that in this calculation we have only considered escape from the dayside of Mars. Because nightside fluxes are a factor of 5-10 lower and are fairly uniform with magnetic field strength (see Figures 5.6a and 5.6c), they should have little effect on the estimations of total outflow made here.

5.8.2 Effect of a crustal field structure on local ion escape

Using a similar framework as in the previous estimate, we now calculate the net effect that a crustal field structure has on local ion flux. This amounts to a simple comparison of the escape fluxes calculated in weak, medium, and strong field regions, without accounting for the total area of Mars covered by these fields. In weak field regions, the total escape flux of $O_2{}^+$ and O^+ has a median value of $1.9 \times 10^6\ cm^{-2}\ s^{-1}$. In medium-strength field regions, escape flux varies with our assumed value of α from $0.4 \times 10^6\ cm^{-2}\ s^{-1}$ ($\alpha = 0$) to $2.8 \times 10^6\ cm^{-2}\ s^{-1}$ ($\alpha = 1$). For a medium-strength crustal field region to have the same escape flux as a weak crustal field region, an α value of 0.65 would be required, implying that 65% of all flux on closed field lines would need to escape the planet. In high-strength crustal field regions, escape fluxes range from $0.3 \times 10^6\,cm^{-2}\,s^{-1}$ ($\beta = 0$) to $2.9 \times 10^6\ cm^{-2}\ s^{-1}$ ($\beta = 1$). To achieve the same escape flux as a weak field region, 60% of the flux measured on closed field lines would need to escape the planet ($\beta = 0.6$).

5.9 Summary and discussion

In this study we used data from the MAVEN spacecraft to investigate the effects of crustal magnetic fields on ion escape at Mars. We analyzed the supply of ions using maps of ion density, the energization of ions using maps of ion fluxes at escape energy, and the possible transport of ions using maps of magnetic field topology. We then used magnetic field data from MAVEN to make maps of particle magnetization in crustal magnetic fields, allowing us to interpret the extent to which escaping ions are affected by magnetic topology.

Together, these works provided us with a broad understanding of ion escape at Mars that we then used to estimate the net effect that crustal magnetic fields have on Martian Ion escape. The results of this estimate are shown in Figure 5.11, where we determined that the presence of crustal fields affects global ion escape by less than a factor of 2. Depending on the assumptions one makes regarding how effectively particles can escape from closed field lines, the influence of crustal magnetic fields could range from a net decrease in escape of 40% to a net increase of 20%. Under fairly typical assumptions, it seems likely that crustal fields currently decrease global ion escape by 20-30%, a finding that is in agreement with previous modeling results.

In this calculation, we did not account at all for the effects of upstream drivers, but it is likely that escape from crustal field regions is significantly impacted by solar wind conditions. In Chapter 3, for example, we showed that increased solar wind pressure tends to compress crustal fields on the dayside of Mars, leaving the ionosphere more exposed. If solar wind variations occur on a fast enough timescale, it is possible that this could leave the high ion densities found in crustal field regions suddenly exposed to the solar wind, leading to a large increase in ion outflow. This may contribute to the 10x enhancement in ion escape that Jakosky et al. (2015b) observed during the impact of an interplanetary coronal mass ejection at Mars.

Finally, we estimated the effect that crustal field structures have on local ion escape, ignoring the global distribution of fields. We found that both medium-strength and strong crustal field regions could potentially increase local ion escape, but only if the ions were sufficiently unmagnetized

that over 60% of ions found on closed magnetic fields with escape energy succede in escaping. If ions with escape energy are not unmagnetized to this degree, then crustal fields should be taken to decrease local escape. In the future, the use of numerical models could help refine this result further. Test-particle models, for example, could provide a more exact determination particle magnetization in the Martian crustal magnetic fields, allowing us to make more precise calculations of ion escape.

The results shown here may hold implications toward the broader question of whether global magnetic dynamos are important for planetary habitability. In the context of planetary evolution, global magnetic fields are often described as critical for the retention of a planet's atmosphere, but it is currently unclear whether this is the case. We may be able to treat crustal fields as a microcosm through which we can characterize the effects of global-scale fields, and investigations of the kind presented here represent a significant step toward that goal. This will be discussed further in the next and final chapter of this thesis, wherein we describe the broader implications of our results and discuss what work lies ahead.

Chapter 6

Perspectives

"There is no real ending. It's just the place where you stop the story."

-Frank Herbert

6.1 Main conclusions

The primary conclusions of the work presented in this thesis are as follows:

(1) Using the MAVEN spacecraft, we can effectively map and analyze magnetic topology at Mars across all local times and all altitudes above the exobase (Chapter 2).

(2) High solar wind pressure causes the Martian ionosphere to become more topologically exposed to the solar wind. This could lead to increased particle escape (Chapter 3).

(3) Changes in IMF direction drive regular changes in topology at Mars, with crustal magnetic field structures varying between open and closed on hourly timescales (Chapter 4).

(4) Crustal magnetic fields have a minor effect on global ion escape, likely decreasing outflow by $\sim$20% (Section 5.8.1).

(5) Only with significantly unmagnetized ions would crustal fields increase local ion escape (Section 5.8.2).

6.2 Magnetic Fields at Mars

Over the course of time spend working on this thesis, our understanding of magnetic fields at Mars has evolved dramatically. With each new result from the MAVEN mission, we gain an ever-increasing appreciation of the complexity of the Martian magnetosphere. Near the planet, modeling results and spacecraft observations find a tangled mess of magnetic field lines threading through the ionosphere, establishing a complex, layered network of magnetic topologies (Weber et al., 2017; Xu et al., 2017a; Ma et al., 2018; Fang et al., 2018). Field lines reconnect frequently, causing the system to vary topologically on a daily timescale (Weber et al., 2020; Harada et al., 2018). As a result of this reconnection, large closed loops of magnetic field are created, connecting the dayside and nightside of Mars to form a system that looks very unlike our typical picture of an induced magnetosphere (Weber et al., 2020; Xu et al., 2018c). Downstream from the planet, the magnetospheric tail lobes exhibit a twisted configuration that results from the interaction with the crustal fields (DiBraccio et al., 2018; Xu et al., 2020b). And this entire magnetic system changes dynamically with the incoming solar wind pressure (Weber et al., 2019), upstream IMF direction (Weber et al., 2020), current dust storm activity (Xu et al., 2014b), space weather activity (Xu et al., 2018a), and EUV flux (Brain et al., 2020). At the same time, the Insight mission has begun returning our first measurements of magnetic fields on the surface of Mars (Johnson et al., 2020), finding the surface fields to be ten times stronger than predicted by crustal field models.

Together, these studies have brought us a more complete understanding of the magnetic environment of Mars than ever before. Much work remains to be done, however, particularly in the context of analyzing how magnetic fields have evolved at Mars over time. For example, though we have determined roughly when the Martian dynamo shut off (Lillis et al., 2013), we know relatively about how this occurred. Likewise, the associated creation and evolution of crustal magnetic fields is mostly unconstrained; crustal fields are expected to have been stronger on ancient Mars, but by how much is unknown. Furthermore, our current observations of how the Martian magnetosphere responds to solar storm events has been limited to only a few case studies. To

understand how magnetic fields have evolved at Mars over time, repeated observations across a wide range of solar wind conditions are needed. The solar wind is expected to have been much stronger and more dynamic in the early solar system, meaning that the observations we make during solar storms today may prove essential toward understanding the behavior of magnetic fields throughout Martian history.

6.3 Do magnetic fields matter?

At the outset of this thesis we posed the question of whether planetary magnetic fields matter in the context of habitability. Here at the end of our discussion, the answer remains a resounding "maybe". Our understanding of the many factors contributing to that answer, however, continues to grow. Recent modeling studies by Egan et al. (2019) and Sakata et al. (2020) showed that for Mars-sized planets, strong magnetic dipoles tend to decrease global ion escape, while weak magnetic dipoles can actually increase global ion escape (as compared to a planet with no dipole at all). These studies found that peak ion escape occurs when a dipole field exists but is not able to balance the incoming pressure of the solar wind. Such a situation results in an ionosphere that is still exposed to the solar wind, but with enhanced cusp outflow facilitated by the presence of vertical magnetic fields. A figure from the Egan et al. study is adapted here in Figure 6.1a. Alongside it we present Figure 6.1b, which displays fluxes measured near the exobase on the dayside of Mars as a function of crustal magnetic field strength. This plot was produced using the same method of analysis that was described in Chapter 5. Interestingly, the two results show very similar trends, with peak escape fluxes are found among middling strength magnetic fields for both O^+ and $O_2{}^+$ ions. This comparison, of course, is not particularly robust. One plot is showing global ion escape while the other is showing local ion fluxes, and it is unclear how much of the flux shown in Figure 6.1b will actually escape the planet (as discussed in Chapter 5). We simply note here that a similar trend is observed, and that we may continue to find it useful to study the Martian crustal magnetic fields as a proxy for understanding the effects of global planetary magnetic fields.

Comparisons between Martian crustal fields and global dynamos will always be imperfect,

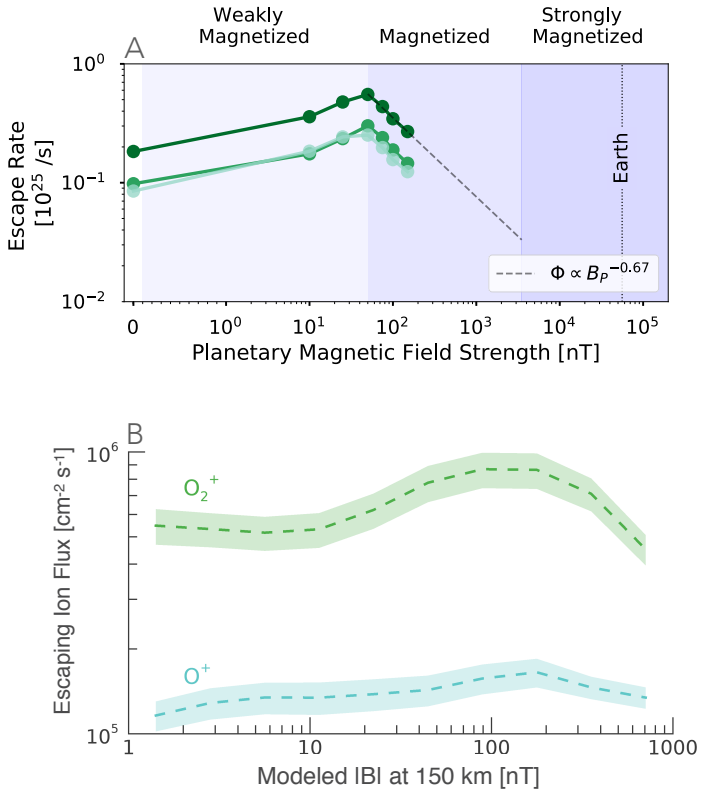

Figure 6.1: (A) Modeled ion escape rates across a range of input planetary magnetic field strengths, adapted from Egan et al. (2019). (B) Escaping ion fluxes between 250 and 500 km on the dayside of Mars. Data is binned by modeled magnetic field strength into in evenly log-spaced bins. The shading around each line represents the standard deviation of fluxes measured in that bin.

however, due both to the large difference in scale and the limited set of conditions that can be found at Mars. To truly decipher the importance of planetary magnetic fields, sophisticated comparisons using observations from multiple planets will be necessary.

Studies using data from Venus could be particularly illuminating. As an example of an unmagnetized planet that has retained a significant atmosphere, Venus represents an important end-member in the spectrum of planetary evolution. Determining how Venus has evolved to its current state will be difficult, and may require further spacecraft missions to the planet. Currently, there are significant gaps in our understanding of both the atmospheric escape processes operating at Venus and the geologic processes that replenish the atmosphere over time. The gaps in our knowledge of escape could be addressed in part through dedicated studies using Venus Express data, as well as through a future spacecraft mission designed specifically to address atmospheric evolution. Understanding of Venusian geology may need to continue to come from numerical models, as the prospects of a rover on the planet's surface remain slim for now.

The true test of whether magnetic fields are important for habitability will come from future observations of exoplanets. As we invent more sophisticated means for detecting, observing, and analyzing exoplanets, we may soon be able to catalog a large number of extrasolar planets, complete with information on their planetary dynamos and atmospheric parameters. Given a large enough sample size, statistical analysis of such a dataset would represent a significant step forward in our understanding of the factors driving atmospheric evolution.

For now, we continue to make incremental steps toward characterizing how planetary evolution can lead to the myriad of different worlds we observe in our solar system today. Studies using spacecraft data gathered at our planetary neighbors, though often small in scope, represent in the truest sense a gateway toward understanding the broader universe. And though our current set of accessible worlds is small (and our current set of life-bearing worlds even smaller), the insights we obtain through these efforts may help set the stage for future discoveries throughout the cosmos.

To that end, we face forward, move slow, and forge ahead.

Bibliography

Abel, B. and Thorne, R. M. (1998). Electron scattering loss in earth's inner magnetosphere: 1. dominant physical processes. Journal of Geophysical Research: Space Physics, 103(A2):2385–2396.

Acuna, M., Connerney, J., Lin, R., Mitchell, D., Carlson, C., McFadden, J., Anderson, K., Rème, H., Mazelle, C., Vignes, D., et al. (1999). Global distribution of crustal magnetization discovered by the mars global surveyor mag/er experiment. Science, 284(5415):790–793.

Acuna, M., Connerney, J., and Ness, N. (1981). Topology of saturn's main magnetic field. Nature, 292(5825):721–724.

Acuna, M., Connerney, J., Wasilewski, P. a., Lin, R., Anderson, K., Carlson, C., McFadden, J., Curtis, D., Mitchell, D., Reme, H., et al. (1998). Magnetic field and plasma observations at mars: Initial results of the mars global surveyor mission. Science, 279(5357):1676–1680.

Adams, D., Xu, S., Mitchell, D., Lillis, R., Fillingim, M., Andersson, L., Fowler, C., Connerney, J., Espley, J., and Mazelle, C. (2018). Using magnetic topology to probe the sources of mars' nightside ionosphere. Geophysical Research Letters, 45(22):12–190.

Andersson, L., Ergun, R., and Stewart, A. (2010). The combined atmospheric photochemistry and ion tracing code: Reproducing the viking lander results and initial outflow results. Icarus, 206(1):120–129.

Andrews, D., Edberg, N. J., Eriksson, A. I., Gurnett, D., Morgan, D., Němec, F., and Opgenoorth, H. J. (2015). Control of the topside martian ionosphere by crustal magnetic fields. Journal of Geophysical Research: Space Physics, 120(4):3042–3058.

Arkani-Hamed, J. (2001). Paleomagnetic pole positions and pole reversals of mars. Geophysical research letters, 28(17):3409–3412.

Bagenal, F., Horányi, M., McComas, D., McNutt, R., Elliott, H., Hill, M., Brown, L., Delamere, P., Kollmann, P., Krimigis, S., et al. (2016). Pluto's interaction with its space environment: Solar wind, energetic particles, and dust. Science, 351(6279):aad9045.

Bandfield, J. L., Glotch, T. D., and Christensen, P. R. (2003). Spectroscopic identification of carbonate minerals in the martian dust. Science, 301(5636):1084–1087.

Benna, M., Mahaffy, P., Grebowsky, J., Fox, J. L., Yelle, R. V., and Jakosky, B. M. (2015). First measurements of composition and dynamics of the martian ionosphere by maven's neutral gas and ion mass spectrometer. Geophysical Research Letters, 42(21):8958–8965.

Bertaux, J.-L., Leblanc, F., Witasse, O., Quemerais, E., Lilensten, J., Stern, S., Sandel, B., and Korablev, O. (2005). Discovery of an aurora on mars. Nature, 435(7043):790–794.

Bertucci, C., Mazelle, C., Crider, D., Vignes, D., Acuña, M., Mitchell, D., Lin, R., Connerney, J., Reme, H., Cloutier, P., et al. (2003). Magnetic field draping enhancement at the martian magnetic pileup boundary from mars global surveyor observations. Geophysical research letters, 30(2).

Bhattacharyya, D., Clarke, J. T., Bertaux, J.-L., Chaufray, J.-Y., and Mayyasi, M. (2015). A strong seasonal dependence in the martian hydrogen exosphere. Geophysical Research Letters, 42(20):8678–8685.

Bogdanov, A. V., Vaisberg, O. L., Kalinin, A. P., and Smirnov, V. (1975). On the gas exchange between the martian upper atmosphere and the solar wind. DoSSR, 225:1284–1287.

Brain, D. (2007). Mars global surveyor measurements of the martian solar wind interaction. In The Mars Plasma Environment, pages 77–112. Springer.

Brain, D., Bagenal, F., Acuña, M., and Connerney, J. (2003). Martian magnetic morphology: Contributions from the solar wind and crust. Journal of Geophysical Research: Space Physics, 108(A12).

Brain, D., Baker, A., Briggs, J., Eastwood, J., Halekas, J., and Phan, T.-D. (2010). Episodic detachment of martian crustal magnetic fields leading to bulk atmospheric plasma escape. Geophysical Research Letters, 37(14).

Brain, D., Halekas, J., Peticolas, L., Lin, R., Luhmann, J., Mitchell, D., Delory, G., Bougher, S., Acuña, M., and Rème, H. (2006a). On the origin of aurorae on mars. Geophysical research letters, 33(1).

Brain, D., Lillis, R., Mitchell, D., Halekas, J., and Lin, R. (2007). Electron pitch angle distributions as indicators of magnetic field topology near mars. Journal of Geophysical Research: Space Physics, 112(A9).

Brain, D., Mitchell, D., and Halekas, J. (2006b). The magnetic field draping direction at mars from april 1999 through august 2004. Icarus, 182(2):464–473.

Brain, D., Weber, T., Xu, S., Mitchell, D., Lillis, R., Halekas, J., Espley, J., and Jakosky, B. (submitted). Variations in night side magnetic field topology at mars. Geophysical Research Letters.

Brain, D. A., Barabash, S., Bougher, S. W., Duru, F., Jakosky, B., and Modolo, R. (2017). Solar wind interaction and atmospheric escape. The Mars Atmosphere, pages 464–496.

Brain, D. A. and Jakosky, B. M. (1998). Atmospheric loss since the onset of the martian geologic record: Combined role of impact erosion and sputtering. Journal of Geophysical Research: Planets, 103(E10):22689–22694.

Brain, D. A., McFadden, J., Halekas, J. S., Connerney, J., Bougher, S. W., Curry, S., Dong, C., Dong, Y., Eparvier, F., Fang, X., et al. (2015). The spatial distribution of planetary ion fluxes near mars observed by maven. Geophysical Research Letters, 42(21):9142–9148.

Brecht, S. H. (1997). Hybrid simulations of the magnetic topology of mars. Journal of Geophysical Research: Space Physics, 102(A3):4743–4750.

Brecht, S. H. and Ledvina, S. A. (2007). The solar wind interaction with the martian ionosphere/atmosphere. In The Mars Plasma Environment, pages 15–38. Springer.

Brecht, S. H. and Ledvina, S. A. (2014). The role of the martian crustal magnetic fields in controlling ionospheric loss. Geophysical Research Letters, 41(15):5340–5346.

Brecht, S. H., Ledvina, S. A., and Bougher, S. W. (2016). Ionospheric loss from mars as predicted by hybrid particle simulations. Journal of Geophysical Research: Space Physics, 121(10):10–190.

Breuer, D. and Spohn, T. (2003). Early plate tectonics versus single-plate tectonics on mars: Evidence from magnetic field history and crust evolution. Journal of Geophysical Research: Planets, 108(E7).

Büchner, J. and Zelenyi, L. M. (1989). Regular and chaotic charged particle motion in magnetotail-like field reversals: 1. basic theory of trapped motion. Journal of Geophysical Research: Space Physics, 94(A9):11821–11842.

Cain, J. C., Ferguson, B. B., and Mozzoni, D. (2003). An n= 90 internal potential function of the martian crustal magnetic field. Journal of Geophysical Research: Planets, 108(E2).

Chaffin, M. S., Chaufray, J.-Y., Stewart, I., Montmessin, F., Schneider, N. M., and Bertaux, J.-L. (2014). Unexpected variability of martian hydrogen escape. Geophysical Research Letters, 41(2):314–320.

Chapman, M. G., Neukum, G., Dumke, A., Michael, G., Van Gasselt, S., Kneissl, T., Zuschneid, W., Hauber, E., Ansan, V., Mangold, N., et al. (2010). Noachian–hesperian geologic history of the echus chasma and kasei valles system on mars: New data and interpretations. Earth and Planetary Science Letters, 294(3-4):256–271.

Collinson, G., Glocer, A., Xu, S., Mitchell, D., Frahm, R. A., Grebowsky, J., Andersson, L., and Jakosky, B. (2019). Ionospheric ambipolar electric fields of mars and venus: Comparisons between theoretical predictions and direct observations of the electric potential drop. Geophysical Research Letters, 46(3):1168–1176.

Collinson, G., Mitchell, D., Glocer, A., Grebowsky, J., Peterson, W., Connerney, J., Andersson, L., Espley, J., Mazelle, C., Sauvaud, J.-A., et al. (2015). Electric mars: The first direct measurement of an upper limit for the martian "polar wind" electric potential. Geophysical Research Letters, 42(21):9128–9134.

Connerney, J., Acuña, M., Ness, N., Kletetschka, G., Mitchell, D., Lin, R., and Reme, H. (2005). Tectonic implications of mars crustal magnetism. Proceedings of the National Academy of Sciences, 102(42):14970–14975.

Connerney, J., Acuna, M., Wasilewski, P., Kletetschka, G., Ness, N., Reme, H., Lin, R., and Mitchell, D. (2001). The global magnetic field of mars and implications for crustal evolution. Geophysical Research Letters, 28(21):4015–4018.

Connerney, J., Espley, J., Lawton, P., Murphy, S., Odom, J., Oliversen, R., and Sheppard, D. (2015). The maven magnetic field investigation. Space Science Reviews, 195(1-4):257–291.

De Niem, D., Kührt, E., Morbidelli, A., and Motschmann, U. (2012). Atmospheric erosion and replenishment induced by impacts upon the earth and mars during a heavy bombardment. Icarus, 221(2):495–507.

Deighan, J., Jain, S., Chaffin, M., Fang, X., Halekas, J. S., Clarke, J. T., Schneider, N., Stewart, A., Chaufray, J.-Y., Evans, J., et al. (2018). Discovery of a proton aurora at mars. Nature Astronomy, 2(10):802–807.

DiBraccio, G. A., Luhmann, J. G., Curry, S. M., Espley, J. R., Xu, S., Mitchell, D. L., Ma, Y., Dong, C., Gruesbeck, J. R., Connerney, J. E., et al. (2018). The twisted configuration of the martian magnetotail: Maven observations. Geophysical Research Letters.

Dobrovolskis, A. and Ingersoll, A. (1975). Carbon dioxide-water clathrate as a reservoir of co2 on mars. Icarus, 26(3):353–357.

Dolginov, S. S., Yeroshenko, Y. G., and Zhuzgov, L. (1976). The magnetic field of mars according to the data from the mars 3 and mars 5. Journal of Geophysical Research, 81(19):3353–3362.

Dong, C., Ma, Y., Bougher, S. W., Toth, G., Nagy, A. F., Halekas, J. S., Dong, Y., Curry, S. M., Luhmann, J. G., Brain, D., et al. (2015a). Multifluid mhd study of the solar wind interaction with mars' upper atmosphere during the 2015 march 8th icme event. Geophysical Research Letters, 42(21):9103–9112.

Dong, Y., Fang, X., Brain, D., McFadden, J., Halekas, J., Connerney, J., Curry, S., Harada, Y., Luhmann, J., and Jakosky, B. (2015b). Strong plume fluxes at mars observed by maven: An important planetary ion escape channel. Geophysical Research Letters, 42(21):8942–8950.

Dubinin, E., Chanteur, G., Fraenz, M., and Woch, J. (2008). Field-aligned currents and parallel electric field potential drops at mars. scaling from the earth'aurora. Planetary and Space Science, 56(6):868–872.

Dubinin, E., Fraenz, M., Woch, J., Roussos, E., Winningham, J., Frahm, R., Coates, A., Leblanc, F., Lundin, R., and Barabash, S. (2008a). Access of solar wind electrons into the martian magnetosphere. In Annales Geophysicae, volume 26, pages 3511–3524. Directory of Open Access Journals.

Dubinin, E., Fraenz, M., Woch, J., Winnigham, J., Frahm, R., Lundin, R., and Barabash, S. (2008b). Suprathermal electron fluxes on the nightside of mars: Aspera-3 observations. Planetary and Space Science, 56(6):846–851.

Dubinin, E., Lundin, R., and Schwingenschuh, K. (1994). Solar wind electrons as tracers of the martian magnetotail topology. Journal of Geophysical Research: Space Physics, 99(A11):21233–21240.

Eastwood, J., Brain, D., Halekas, J., Drake, J., Phan, T., Øieroset, M., Mitchell, D., Lin, R., and Acuña, M. (2008). Evidence for collisionless magnetic reconnection at mars. Geophysical Research Letters, 35(2).

Edberg, N., Nilsson, H., Williams, A., Lester, M., Milan, S., Cowley, S., Fränz, M., Barabash, S., and Futaana, Y. (2010). Pumping out the atmosphere of mars through solar wind pressure pulses. Geophysical Research Letters, 37(3).

Edwards, C. S. and Ehlmann, B. L. (2015). Carbon sequestration on mars. Geology, 43(10):863–866.

Egan, H., Jarvinen, R., Ma, Y., and Brain, D. (2019). Planetary magnetic field control of ion escape from weakly magnetized planets. Monthly Notices of the Royal Astronomical Society, 488(2):2108–2120.

Ehlmann, B. L. and Edwards, C. S. (2014). Mineralogy of the martian surface. Annual Review of Earth and Planetary Sciences, 42.

Ehlmann, B. L., Mustard, J. F., Murchie, S. L., Poulet, F., Bishop, J. L., Brown, A. J., Calvin, W. M., Clark, R. N., Des Marais, D. J., Milliken, R. E., et al. (2008). Orbital identification of carbonate-bearing rocks on mars. Science, 322(5909):1828–1832.

Ergun, R., Andersson, L., Fowler, C., Woodson, A., Weber, T., Delory, G., Andrews, D., Eriksson, A., McEnulty, T., Morooka, M., et al. (2016). Enhanced o2+ loss at mars due to an ambipolar electric field from electron heating. Journal of Geophysical Research: Space Physics.

Ergun, R., Andersson, L., Peterson, W., Brain, D., Delory, G., Mitchell, D., Lin, R., and Yau, A. (2006). Role of plasma waves in mars' atmospheric loss. Geophysical research letters, 33(14).

Espley, J. R. (2018). The martian magnetosphere: Areas of unsettled terminology. Journal of Geophysical Research: Space Physics, 123(6):4521–4525.

Evans, J. E. and Maunder, E. W. (1903). Experiments as to the actuality of the" canals" observed on mars. Monthly Notices of the Royal Astronomical Society, 63:488–499.

Fang, X., Liemohn, M. W., Nagy, A. F., Luhmann, J. G., and Ma, Y. (2010a). Escape probability of martian atmospheric ions: Controlling effects of the electromagnetic fields. Journal of Geophysical Research: Space Physics, 115(A4).

Fang, X., Liemohn, M. W., Nagy, A. F., Luhmann, J. G., and Ma, Y. (2010b). On the effect of the martian crustal magnetic field on atmospheric erosion. Icarus, 206(1):130–138.

Fang, X., Liemohn, M. W., Nagy, A. F., Ma, Y., De Zeeuw, D. L., Kozyra, J. U., and Zurbuchen, T. H. (2008). Pickup oxygen ion velocity space and spatial distribution around mars. Journal of Geophysical Research: Space Physics, 113(A2).

Fang, X., Ma, Y., Brain, D., Dong, Y., and Lillis, R. (2015). Control of mars global atmospheric loss by the continuous rotation of the crustal magnetic field: A time-dependent mhd study. Journal of Geophysical Research: Space Physics, 120(12):10–926.

Fang, X., Ma, Y., Luhmann, J., Dong, Y., Brain, D., Hurley, D., Dong, C., Lee, C. O., and Jakosky, B. (2018). The morphology of the solar wind magnetic field draping on the dayside of mars and its variability. Geophysical Research Letters, 45(8):3356–3365.

Fang, X., Ma, Y., Masunaga, K., Dong, Y., Brain, D., Halekas, J., Lillis, R., Jakosky, B., Connerney, J., Grebowsky, J., et al. (2017). The mars crustal magnetic field control of plasma boundary locations and atmospheric loss: Mhd prediction and comparison with maven. Journal of Geophysical Research: Space Physics, 122(4):4117–4137.

Fillingim, M., Peticolas, L., Lillis, R., Brain, D., Halekas, J., Lummerzheim, D., and Bougher, S. (2010). Localized ionization patches in the nighttime ionosphere of mars and their electrodynamic consequences. Icarus, 206(1):112–119.

Fillingim, M., Peticolas, L., Lillis, R., Brain, D., Halekas, J., Mitchell, D., Lin, R., Lummerzheim, D., Bougher, S., and Kirchner, D. (2007). Model calculations of electron precipitation induced ionization patches on the nightside of mars. Geophysical research letters, 34(12).

Fowler, C., Andersson, L., Ergun, R., Morooka, M., Delory, G., Andrews, D. J., Lillis, R. J., McEnulty, T., Weber, T., Chamandy, T., et al. (2015). The first in situ electron temperature and density measurements of the martian nightside ionosphere. Geophysical Research Letters, 42(21):8854–8861.

Fowler, C., Lee, C., Xu, S., Mitchell, D., Lillis, R., Weber, T., Halekas, J., Andersson, L., Espley, J., Ergun, R., et al. (2019). The penetration of draped magnetic field into the martian upper ionosphere and correlations with upstream solar wind dynamic pressure. Journal of Geophysical Research: Space Physics, 124(4):3021–3035.

Fox, J. L. (1993). On the escape of oxygen and hydrogen from mars. Geophysical research letters, 20(17):1747–1750.

Fox, J. L., Brannon, J., and Porter, H. (1993). Upper limits to the nightside ionosphere of mars. Geophysical research letters, 20(13):1339–1342.

Fox, J. L. and Dalgarno, A. (1979). Ionization, luminosity, and heating of the upper atmosphere of mars. Journal of Geophysical Research: Space Physics, 84(A12):7315–7333.

Fox, J. L. and Hać, A. B. (2009). Photochemical escape of oxygen from mars: A comparison of the exobase approximation to a monte carlo method. Icarus, 204(2):527–544.

Frahm, R., Sharber, J., Winningham, J., Wurz, P., Liemohn, M., Kallio, E., Yamauchi, M., Lundin, R., Barabash, S., Coates, A., et al. (2006a). Locations of atmospheric photoelectron energy peaks within the mars environment. Space science reviews, 126(1-4):389–402.

Frahm, R., Winningham, J., Sharber, J., Scherrer, J., Jeffers, S., Coates, A., Linder, D., Kataria, D., Lundin, R., Barabash, S., et al. (2006b). Carbon dioxide photoelectron energy peaks at mars. Icarus, 182(2):371–382.

Frank, L., Paterson, W., Ackerson, K., and Bolton, S. (1997). Low-energy electron measurements at ganymede with the galileo spacecraft: Probes of the magnetic topology. Geophysical research letters, 24(17):2159–2162.

Fuselier, S., Trattner, K., Petrinec, S., and Lavraud, B. (2012). Dayside magnetic topology at the earth's magnetopause for northward imf. Journal of Geophysical Research: Space Physics, 117(A8).

Gershman, D. J., Raines, J. M., Slavin, J. A., Zurbuchen, T. H., Anderson, B. J., Korth, H., Ho, G. C., Boardsen, S. A., Cassidy, T. A., Walsh, B. M., and Solomon, S. C. (2015). Messenger observations of solar energetic electrons within mercury's magnetosphere. Journal of Geophysical Research: Space Physics, 120(10):8559–8571.

Goertz, C. K., Jones, D., Randall, B., Smith, E., and Thomsen, M. (1976). Evidence for open field lines in jupiter's magnetosphere. Journal of Geophysical Research, 81(19):3393–3398.

Gosling, J., Skoug, R., and Feldman, W. (2001). Solar wind electron halo depletions at 90 pitch angle. Geophysical research letters, 28(22):4155–4158.

Grießmeier, J.-M., Stadelmann, A., Penz, T., Lammer, H., Selsis, F., Ribas, I., Guinan, E., Motschmann, U., Biernat, H., and Weiss, W. (2004). The effect of tidal locking on the magnetospheric and atmospheric evolution of "hot jupiters". Astronomy & Astrophysics, 425(2):753–762.

Griffin, L. and Zimbelman, J. (2009). Geologic mapping of western medusae fossae formation, mars (mc 23-nw): Redefining unit boundaries and features to reveal a history of tectonism, wind erosion, and episodic water flow. LPI, page 1196.

Grotzinger, J., Gupta, S., Malin, M., Rubin, D., Schieber, J., Siebach, K., Sumner, D., Stack, K., Vasavada, A., Arvidson, R., et al. (2015). Deposition, exhumation, and paleoclimate of an ancient lake deposit, gale crater, mars. Science, 350(6257).

Gurnett, D., Kirchner, D., Huff, R., Morgan, D., Persoon, A., Averkamp, T., Duru, F., Nielsen, E., Safaeinili, A., Plaut, J., et al. (2005). Radar soundings of the ionosphere of mars. Science, 310(5756):1929–1933.

Haider, S., Kim, J., Nagy, A., Keller, C., Verigin, M., Gringauz, K., Shutte, N., Szego, K., and Kiraly, P. (1992). Calculated ionization rates, ion densities, and airglow emission rates due to precipitating electrons in the nightside ionosphere of mars. Journal of Geophysical Research: Space Physics, 97(A7):10637–10641.

Halekas, J., Lillis, R., Mitchell, D., Cravens, T., Mazelle, C., Connerney, J., Espley, J., Mahaffy, P., Benna, M., Jakosky, B., et al. (2015b). Maven observations of solar wind hydrogen deposition in the atmosphere of mars. Geophysical Research Letters, 42(21):8901–8909.

Halekas, J., Ruhunusiri, S., Harada, Y., Collinson, G., Mitchell, D., Mazelle, C., McFadden, J., Connerney, J., Espley, J., Eparvier, F., et al. (2016). Structure, dynamics, and seasonal variability of the mars-solar wind interaction: Maven solar wind ion analyzer inflight performance and science results. Journal of Geophysical Research: Space Physics.

Halekas, J., Taylor, E., Dalton, G., Johnson, G., Curtis, D., McFadden, J., Mitchell, D., Lin, R., and Jakosky, B. (2015). The solar wind ion analyzer for maven. Space Science Reviews, 195(1-4):125–151.

Harada, Y., Halekas, J., DiBraccio, G., Xu, S., Espley, J., Mcfadden, J., Mitchell, D., Mazelle, C., Brain, D., Hara, T., et al. (2018). Magnetic reconnection on dayside crustal magnetic fields at mars: Maven observations. Geophysical Research Letters, 45(10):4550–4558.

Harada, Y., Halekas, J., McFadden, J., Mitchell, D., Mazelle, C., Connerney, J., Espley, J., Larson, D., Brain, D., Andersson, L., et al. (2015). Magnetic reconnection in the near-mars magnetotail: Maven observations. Geophysical Research Letters, 42(21):8838–8845.

Harnett, E. and Winglee, R. (2006). Three-dimensional multifluid simulations of ionospheric loss at mars from nominal solar wind conditions to magnetic cloud events. Journal of Geophysical Research: Space Physics, 111(A9).

Harnett, E. and Winglee, R. (2007). High-resolution multifluid simulations of the plasma environment near the martian magnetic anomalies. Journal of Geophysical Research: Space Physics, 112(A5).

Harnett, E. M. and Winglee, R. (2003). The influence of a mini-magnetopause on the magnetic pileup boundary at mars. Geophysical Research Letters, 30(20).

Hathaway, D. H. and Dessler, A. (1986). Magnetic reversals of jupiter and saturn. Icarus, 67(1):88–95.

Heavens, N. G., Kleinböhl, A., Chaffin, M. S., Halekas, J. S., Kass, D. M., Hayne, P. O., McCleese, D. J., Piqueux, S., Shirley, J. H., and Schofield, J. T. (2018). Hydrogen escape from mars enhanced by deep convection in dust storms. Nature Astronomy, 2(2):126–132.

Holmstrom, M. and Wang, X.-D. (2015). Mars as a comet: Solar wind interaction on a large scale. Planetary and Space Science, 119:43–47.

Hynek, B. M., Beach, M., and Hoke, M. R. (2010). Updated global map of martian valley networks and implications for climate and hydrologic processes. Journal of Geophysical Research: Planets, 115(E9).

Jakosky, B., Brain, D., Chaffin, M., Curry, S., Deighan, J., Grebowsky, J., Halekas, J., Leblanc, F., Lillis, R., Luhmann, J., et al. (2018). Loss of the martian atmosphere to space: Present-day loss rates determined from maven observations and integrated loss through time. Icarus, 315:146–157.

Jakosky, B., Lin, R., Grebowsky, J., Luhmann, J., Mitchell, D., Beutelschies, G., Priser, T., Acuna, M., Andersson, L., Baird, D., et al. (2015a). The mars atmosphere and volatile evolution (maven) mission. Space Science Reviews, 195(1-4):3–48.

Jakosky, B., Slipski, M., Benna, M., Mahaffy, P., Elrod, M., Yelle, R., Stone, S., and Alsaeed, N. (2017). Mars' atmospheric history derived from upper-atmosphere measurements of 38ar/36ar. Science, 355(6332):1408–1410.

Jakosky, B. M., Grebowsky, J. M., Luhmann, J. G., Connerney, J., Eparvier, F., Ergun, R., Halekas, J., Larson, D., Mahaffy, P., Mcfadden, J., et al. (2015b). Maven observations of the response of mars to an interplanetary coronal mass ejection. Science, 350(6261):aad0210.

Jarvinen, R., Brain, D., and Luhmann, J. (2016). Dynamics of planetary ions in the induced magnetospheres of venus and mars. Planetary and Space Science, 127:1–14.

Jarvinen, R., Brain, D. A., Modolo, R., Fedorov, A., and Holmström, M. (2018). Oxygen ion energization at mars: Comparison of maven and mars express observations to global hybrid simulation. Journal of Geophysical Research: Space Physics, 123(2):1678–1689.

Johnson, C. L., Mittelholz, A., Langlais, B., Russell, C. T., Ansan, V., Banfield, D., Chi, P. J., Fillingim, M. O., Forget, F., Haviland, H. F., et al. (2020). Crustal and time-varying magnetic fields at the insight landing site on mars. Nature Geoscience, 13(3):199–204.

Kahler, S., Crocker, N., and Gosling, J. (1996). The topology of intrasector reversals of the interplanetary magnetic field. Journal of Geophysical Research: Space Physics, 101(A11):24373–24382.

Kahler, S. and Hundhausen, A. (1992). The magnetic topology of solar coronal structures following mass ejections. Journal of Geophysical Research: Space Physics, 97(A2):1619–1631.

Kallio, E. and Barabash, S. (2012). Magnetized mars: Spatial distribution of oxygen ions. Earth, planets and space, 64(2):10.

Kallio, E., Fedorov, A., Budnik, E., Säles, T., Janhunen, P., Schmidt, W., Koskinen, H., Riihelä, P., Barabash, S., Lundin, R., et al. (2006). Ion escape at mars: Comparison of a 3-d hybrid simulation with mars express ima/aspera-3 measurements. Icarus, 182(2):350–359.

Kerber, L. and Head, J. W. (2010). The age of the medusae fossae formation: Evidence of hesperian emplacement from crater morphology, stratigraphy, and ancient lava contacts. Icarus, 206(2):669–684.

Kite, E. S., Williams, J.-P., Lucas, A., and Aharonson, O. (2014). Low palaeopressure of the martian atmosphere estimated from the size distribution of ancient craters. Nature Geoscience, 7(5):335–339.

Krasnopolsky, V., Bjoraker, G., Mumma, M., and Jennings, D. (1997). High-resolution spectroscopy of mars at 3.7 and 8 μm: A sensitive search for h2o2, h2co, hcl, and ch4, and detection of hdo. Journal of Geophysical Research: Planets, 102(E3):6525–6534.

Krymskii, A., Breus, T., Ness, N., Acuña, M., Connerney, J., Crider, D., Mitchell, D., and Bauer, S. (2002). Structure of the magnetic field fluxes connected with crustal magnetization and topside ionosphere at mars. Journal of Geophysical Research: Space Physics, 107(A9).

Krymskii, A., Ness, N., Crider, D., Breus, T., Acuna, M., and Hinson, D. (2004). Solar wind interaction with the ionosphere/atmosphere and crustal magnetic fields at mars: Mars global surveyor magnetometer/electron reflectometer, radio science, and accelerometer data. Journal of Geophysical Research: Space Physics, 109(A11).

Lammer, H. and Bauer, S. (1991). Nonthermal atmospheric escape from mars and titan. Journal of Geophysical Research: Space Physics, 96(A2):1819–1825.

Lammer, H., Kislyakova, K., Odert, P., Leitzinger, M., Schwarz, R., Pilat-Lohinger, E., Kulikov, Y. N., Khodachenko, M., Güdel, M., and Hanslmeier, A. (2011). Pathways to earth-like atmospheres. Origins of Life and Evolution of Biospheres, 41(6):503–522.

Lammer, H., Ribas, I., Grießmeier, J.-M., Penz, T., Hanslmeier, A., and Biernat, H. (2004). A brief history of the solar radiation and particle flux evolution. Hvar Observatory Bulletin, 28:139–155.

Langlais, B., Lesur, V., Purucker, M. E., Connerney, J. E., and Mandea, M. (2010). Crustal magnetic fields of terrestrial planets. Space Science Reviews, 152(1-4):223–249.

Larson, D., Lin, R., McTiernan, J., McFadden, J., Ergun, R., McCarthy, M., Reme, H., Sanderson, T., Kaiser, M., Lepping, R., et al. (1997). Tracing the topology of the october 18–20, 1995, magnetic cloud with $0.1–10^2$ kev electrons. Geophysical research letters, 24(15):1911–1914.

Leblanc, F. and Johnson, R. (2001). Sputtering of the martian atmosphere by solar wind pick-up ions. Planetary and Space Science, 49(6):645–656.

Leblanc, F., Martinez, A., Chaufray, J., Modolo, R., Hara, T., Luhmann, J., Lillis, R., Curry, S., McFadden, J., Halekas, J., et al. (2018). On mars's atmospheric sputtering after maven's first martian year of measurements. Geophysical Research Letters, 45(10):4685–4691.

Leblanc, F., Witasse, O., Lilensten, J., Frahm, R., Safaenili, A., Brain, D., Mouginot, J., Nilsson, H., Futaana, Y., Halekas, J., et al. (2008). Observations of aurorae by spicam ultraviolet spectrograph on board mars express: Simultaneous aspera-3 and marsis measurements. Journal of Geophysical Research: Space Physics, 113(A8).

Leblanc, F., Witasse, O., Winningham, J., Brain, D., Lilensten, J., Blelly, P.-L., Frahm, R., Halekas, J. S., and Bertaux, J.-L. (2006). Origins of the martian aurora observed by spectroscopy for investigation of characteristics of the atmosphere of mars (spicam) on board mars express. Journal of Geophysical Research: Space Physics, 111(A9).

Liemohn, M., Ma, Y., Nagy, A., Kozyra, J., Winningham, J., Frahm, R., Sharber, J., Barabash, S., and Lundin, R. (2007a). Numerical modeling of the magnetic topology near mars auroral observations. Geophysical Research Letters, 34(24).

Liemohn, M. W., Ma, Y., Frahm, R. A., Fang, X., Kozyra, J. U., Nagy, A. F., Winningham, J. D., Sharber, J. R., Barabash, S., and Lundin, R. (2007b). Mars global mhd predictions of magnetic connectivity between the dayside ionosphere and the magnetospheric flanks. In The Mars Plasma Environment, pages 63–76. Springer.

Lillis, R., Engel, J., Mitchell, D., Brain, D., Lin, R., Bougher, S., and Acuña, M. (2005). Probing upper thermospheric neutral densities at mars using electron reflectometry. Geophysical research letters, 32(23).

Lillis, R. J. and Brain, D. A. (2013). Nightside electron precipitation at mars: Geographic variability and dependence on solar wind conditions. Journal of Geophysical Research: Space Physics, 118(6):3546–3556.

Lillis, R. J., Deighan, J., Fox, J. L., Bougher, S. W., Lee, Y., Combi, M. R., Cravens, T. E., Rahmati, A., Mahaffy, P. R., Benna, M., et al. (2017). Photochemical escape of oxygen from mars: First results from maven in situ data. Journal of Geophysical Research: Space Physics, 122(3):3815–3836.

Lillis, R. J. and Fang, X. (2015). Electron impact ionization in the martian atmosphere: Interplay between scattering and crustal magnetic field effects. Journal of Geophysical Research: Planets, 120(7):1332–1345.

Lillis, R. J., Fillingim, M. O., and Brain, D. A. (2011). Three-dimensional structure of the martian nightside ionosphere: Predicted rates of impact ionization from mars global surveyor magnetometer and electron reflectometer measurements of precipitating electrons. Journal of Geophysical Research: Space Physics, 116(A12).

Lillis, R. J., Fillingim, M. O., Peticolas, L. M., Brain, D. A., Lin, R. P., and Bougher, S. W. (2009). Nightside ionosphere of mars: Modeling the effects of crustal magnetic fields and electron pitch angle distributions on electron impact ionization. Journal of Geophysical Research: Planets, 114(E11).

Lillis, R. J., Mitchell, D. L., Lin, R. P., and Acuña, M. H. (2008). Electron reflectometry in the martian atmosphere. Icarus, 194(2):544–561.

Lillis, R. J., Mitchell, D. L., Steckiewicz, M., Brain, D., Xu, S., Weber, T., Halekas, J., Connerney, J., Espley, J., Benna, M., et al. (2018). Ionizing electrons on the martian nightside: structure and variability. Journal of Geophysical Research: Space Physics.

Lillis, R. J., Robbins, S., Manga, M., Halekas, J. S., and Frey, H. V. (2013). Time history of the martian dynamo from crater magnetic field analysis. Journal of Geophysical Research: Planets, 118(7):1488–1511.

Luhmann, J. (1990). A model of the ion wake of mars. Geophysical research letters, 17(6):869–872.

Luhmann, J., Dong, C., Ma, Y., Curry, S., Xu, S., Lee, C., Hara, T., Halekas, J., Li, Y., Gruesbeck, J., et al. (2017). Martian magnetic storms. Journal of Geophysical Research: Space Physics, 122(6):6185–6209.

Luhmann, J., Johnson, R., and Zhang, M. (1992). Evolutionary impact of sputtering of the martian atmosphere by o+ pickup ions. Geophysical research letters, 19(21):2151–2154.

Luhmann, J. and Kozyra, J. (1991). Dayside pickup oxygen ion precipitation at venus and mars: Spatial distributions, energy deposition and consequences. Journal of Geophysical Research: Space Physics, 96(A4):5457–5467.

Luhmann, J. G., Dong, C., Ma, Y., Curry, S., Mitchell, D., Espley, J., Connerney, J., Halekas, J., Brain, D., Jakosky, B., et al. (2015). Implications of maven mars near-wake measurements and models. Geophysical Research Letters, 42(21):9087–9094.

Lundin, R., Barabash, S., Holmström, M., Nilsson, H., Yamauchi, M., Fraenz, M., and Dubinin, E. (2008). A comet-like escape of ionospheric plasma from mars. Geophysical research letters, 35(18).

Lundin, R., Barabash, S., Yamauchi, M., Nilsson, H., and Brain, D. (2011). On the relation between plasma escape and the martian crustal magnetic field. Geophysical Research Letters, 38(2).

Lundin, R. and Hultqvist, B. (1989). Ionospheric plasma escape by high-altitude electric fields: Magnetic moment" pumping". Journal of Geophysical Research: Space Physics, 94(A6):6665–6680.

Lundin, R., Lammer, H., and Ribas, I. (2007). Planetary magnetic fields and solar forcing: Implications for atmospheric evolution. Space Science Reviews, 129(1-3):245–278.

Lundin, R., Zakharov, A., Pellinen, R., Barabasj, S., Borg, H., Dubinin, E., Hultqvist, B., Koskinen, H., Liede, I., and Pissarenko, N. (1990). Aspera/phobos measurements of the ion outflow from the martian ionosphere. Geophysical research letters, 17(6):873–876.

Lyons, L. R., Thorne, R. M., and Kennel, C. F. (1972). Pitch-angle diffusion of radiation belt electrons within the plasmasphere. Journal of Geophysical Research, 77(19):3455–3474.

Ma, Y., Fang, X., Russell, C. T., Nagy, A. F., Toth, G., Luhmann, J. G., Brain, D. A., and Dong, C. (2014). Effects of crustal field rotation on the solar wind plasma interaction with mars. Geophysical Research Letters, 41(19):6563–6569.

Ma, Y., Nagy, A. F., Hansen, K. C., DeZeeuw, D. L., Gombosi, T. I., and Powell, K. (2002). Three-dimensional multispecies mhd studies of the solar wind interaction with mars in the presence of crustal fields. Journal of Geophysical Research: Space Physics, 107(A10):SMP–6.

Ma, Y., Russell, C., Fang, X., Dong, C., Nagy, A., Toth, G., Halekas, J., Connerney, J., Espley, J., Mahaffy, P., et al. (2017). Variations of the martian plasma environment during the icme passage on 8 march 2015: A time-dependent mhd study. Journal of Geophysical Research: Space Physics, 122(2):1714–1730.

Ma, Y., Russell, C. T., Fang, X., Dong, Y., Nagy, A., Toth, G., Halekas, J. S., Connerney, J. E., Espley, J. R., Mahaffy, P. R., et al. (2015). Mhd model results of solar wind interaction with mars and comparison with maven plasma observations. Geophysical Research Letters, 42(21):9113–9120.

Ma, Y., Russell, C. T., Toth, G., Chen, Y., Nagy, A. F., Harada, Y., McFadden, J., Halekas, J. S., Lillis, R., Connerney, J. E., et al. (2018). Reconnection in the martian magnetotail: Hall-mhd with embedded particle-in-cell simulations. Journal of Geophysical Research: Space Physics, 123(5):3742–3763.

Mahaffy, P., Webster, C., Stern, J., Brunner, A., Atreya, S., Conrad, P., Domagal-Goldman, S., Eigenbrode, J., Flesch, G. J., Christensen, L. E., et al. (2015). The imprint of atmospheric evolution in the d/h of hesperian clay minerals on mars. Science, 347(6220):412–414.

Matsunaga, K., Seki, K., Brain, D. A., Hara, T., Masunaga, K., Mcfadden, J. P., Halekas, J. S., Mitchell, D. L., Mazelle, C., Espley, J., et al. (2017). Statistical study of relations between the induced magnetosphere, ion composition, and pressure balance boundaries around mars based on maven observations. Journal of Geophysical Research: Space Physics, 122(9):9723–9737.

McElroy, M. B., Kong, T. Y., and Yung, Y. L. (1977). Photochemistry and evolution of mars' atmosphere: A viking perspective. Journal of Geophysical Research, 82(28):4379–4388.

Mitchell, D., Kutchko, F., Williams, D., Eastman, T., Frank, L., and Russell, C. (1987). An extended study of the low-latitude boundary layer on the dawn and dusk flanks of the magnetosphere. Journal of Geophysical Research: Space Physics, 92(A7):7394–7404.

Mitchell, D., Lillis, R., Lin, R., Connerney, J., and Acuña, M. (2007). A global map of mars' crustal magnetic field based on electron reflectometry. Journal of Geophysical Research: Planets, 112(E1).

Mitchell, D., Lin, R., Mazelle, C., Rème, H., Cloutier, P., Connerney, J., Acuña, M., and Ness, N. (2001). Probing mars' crustal magnetic field and ionosphere with the mgs electron reflectometer. Journal of Geophysical Research: Planets, 106(E10):23419–23427.

Mitchell, D., Mazelle, C., Sauvaud, J.-A., Thocaven, J.-J., Rouzaud, J., Fedorov, A., Rouger, P., Toublanc, D., Taylor, E., Gordon, D., et al. (2016). The maven solar wind electron analyzer. Space Science Reviews, 200(1-4):495–528.

Mittelholz, A., Johnson, C., Phillips, R. J., Langlais, B., and Feinberg, J. M. (2019). New constraints on the dynamo timing and crustal magnetization on mars from maven observations. AGUFM, 2019:GP23A–04.

Modolo, R., Chanteur, G., Dubinin, E., and Matthews, A. (2006). Simulated solar wind plasma interaction with the martian exosphere: influence of the solar euv flux on the bow shock and the magnetic pile-up boundary.

Modolo, R., Hess, S., Mancini, M., Leblanc, F., Chaufray, J.-Y., Brain, D., Leclercq, L., Esteban-Hernández, R., Chanteur, G., Weill, P., et al. (2016). Mars-solar wind interaction: Lathys, an improved parallel 3-d multispecies hybrid model. Journal of Geophysical Research: Space Physics, 121(7):6378–6399.

Moore, T. E. and Horwitz, J. (2007). Stellar ablation of planetary atmospheres. Reviews of Geophysics, 45(3).

Morschhauser, A., Lesur, V., and Grott, M. (2014). A spherical harmonic model of the lithospheric magnetic field of mars. Journal of Geophysical Research: Planets, 119(6):1162–1188.

Morschhauser, A., Vervelidou, F., Thomas, P., Grott, M., Lesur, V., and Gilder, S. A. (2018). Mars' crustal magnetic field. In Magnetic Fields in the Solar System, pages 331–356. Springer.

Nagy, A., Winterhalter, D., Sauer, K., Cravens, T., Brecht, S., Mazelle, C., Crider, D., Kallio, E., Zakharov, A., Dubinin, E., et al. (2004). The plasma environment of mars. Space Science Reviews, 111(1-2):33–114.

Němec, F., Morgan, D., Gurnett, D., and Brain, D. (2011). Areas of enhanced ionization in the deep nightside ionosphere of mars. Journal of Geophysical Research: Planets, 116(E6).

Nielsen, E., Fraenz, M., Zou, H., Wang, J.-S., Gurnett, D., Kirchner, D., Morgan, D., Huff, R., Safaeinili, A., Plaut, J., et al. (2007). Local plasma processes and enhanced electron densities in the lower ionosphere in magnetic cusp regions on mars. Planetary and Space Science, 55(14):2164–2172.

Nilsson, H., Edberg, N. J., Stenberg, G., Barabash, S., Holmström, M., Futaana, Y., Lundin, R., and Fedorov, A. (2011). Heavy ion escape from mars, influence from solar wind conditions and crustal magnetic fields. Icarus, 215(2):475–484.

Penz, T., Erkaev, N., Biernat, H., Lammer, H., Amerstorfer, U., Gunell, H., Kallio, E., Barabash, S., Orsini, S., Milillo, A., et al. (2004). Ion loss on mars caused by the kelvin–helmholtz instability. Planetary and Space Science, 52(13):1157–1167.

Peterson, W., Thiemann, E. B., Eparvier, F. G., Andersson, L., Fowler, C., Larson, D., Mitchell, D., Mazelle, C., Fontenla, J., Evans, J. S., et al. (2016). Photoelectrons and solar ionizing radiation at mars: Predictions versus maven observations. Journal of Geophysical Research: Space Physics, 121(9):8859–8870.

Pham, L. B. S., Karatekin, Ö., and Dehant, V. (2009). Effects of meteorite impacts on the atmospheric evolution of mars. Astrobiology, 9(1):45–54.

Pollack, J. B., Kasting, J. F., Richardson, S. M., and Poliakoff, K. (1987). The case for a wet, warm climate on early mars. Icarus, 71(2):203–224.

Rahmati, A., Larson, D., Cravens, T., Lillis, R., Halekas, J., McFadden, J., Dunn, P., Mitchell, D., Thiemann, E., Eparvier, F., et al. (2017). Maven measured oxygen and hydrogen pickup ions: Probing the martian exosphere and neutral escape. Journal of Geophysical Research: Space Physics, 122(3):3689–3706.

Ramstad, R., Barabash, S., Futaana, Y., Nilsson, H., and Holmström, M. (2016). Effects of the crustal magnetic fields on the martian atmospheric ion escape rate. Geophysical Research Letters, 43(20):10–574.

Ramstad, R., Barabash, S., Futaana, Y., Nilsson, H., Wang, X.-D., and Holmström, M. (2015). The martian atmospheric ion escape rate dependence on solar wind and solar euv conditions: 1. seven years of mars express observations. Journal of Geophysical Research: Planets, 120(7):1298–1309.

Ribas, I., Guinan, E. F., Güdel, M., and Audard, M. (2005). Evolution of the solar activity over time and effects on planetary atmospheres. i. high-energy irradiances (1-1700 å). The Astrophysical Journal, 622(1):680.

Sakai, S., Andersson, L., Cravens, T. E., Mitchell, D. L., Mazelle, C., Rahmati, A., Fowler, C. M., Bougher, S. W., Thiemann, E., Eparvier, F. G., et al. (2016). Electron energetics in the martian dayside ionosphere: Model comparisons with maven data. Journal of Geophysical Research: Space Physics, 121(7):7049–7066.

Sakata, R., Seki, K., Sakai, S., Terada, N., Shinagawa, H., and Tanaka, T. (2020). Effects of an intrinsic magnetic field on ion loss from ancient mars based on multispecies mhd simulations. Journal of Geophysical Research: Space Physics, 125(2):e2019JA026945.

Schiaparelli, G. V. (1882). Découvertes nouvelles sur la planète mars. L'Astronomie, 1:216–221.

Schubert, G., Russell, C., and Moore, W. (2000). Timing of the martian dynamo. Nature, 408(6813):666–667.

Shahnas, H. and Arkani-Hamed, J. (2007). Viscous and impact demagnetization of martian crust. Journal of Geophysical Research: Planets, 112(E2).

Shane, A. D., Xu, S., Liemohn, M. W., and Mitchell, D. L. (2016). Mars nightside electrons over strong crustal fields. Journal of Geophysical Research: Space Physics, 121(4):3808–3823.

Smith, A., Jackman, C., and Thomsen, M. (2016). Magnetic reconnection in saturn's magnetotail: A comprehensive magnetic field survey. Journal of Geophysical Research: Space Physics, 121(4):2984–3005.

Steckiewicz, M., Mazelle, C., Garnier, P., André, N., Penou, E., Beth, A., Sauvaud, J.-A., Toublanc, D., Mitchell, D., McFadden, J., et al. (2015). Altitude dependence of nightside martian suprathermal electron depletions as revealed by maven observations. Geophysical Research Letters, 42(21):8877–8884.

Stewart, S. T. and Nimmo, F. (2002). Surface runoff features on mars: Testing the carbon dioxide formation hypothesis. Journal of Geophysical Research: Planets, 107(E9):7–1.

Svetsov, V. (2007). Atmospheric erosion and replenishment induced by impacts of cosmic bodies upon the earth and mars. Solar System Research, 41(1):28–41.

Terada, N., Machida, S., and Shinagawa, H. (2002). Global hybrid simulation of the kelvin–helmholtz instability at the venus ionopause. Journal of Geophysical Research: Space Physics, 107(A12):SMP–30.

Terada, N., Shinagawa, H., Tanaka, T., Murawski, K., and Terada, K. (2009). A three-dimensional, multispecies, comprehensive mhd model of the solar wind interaction with the planet venus. Journal of Geophysical Research: Space Physics, 114(A9).

Ulusen, D., Brain, D. A., and Mitchell, D. L. (2011). Observation of conical electron distributions over martian crustal magnetic fields. Journal of Geophysical Research: Space Physics, 116(A7).

Ulusen, D., Luhmann, J., Ma, Y., and Brain, D. (2016). Solar control of the martian magnetic topology: Implications from model-data comparisons. Planetary and Space Science, 128:1–13.

Vaisberg, O. and Smirnov, V. (1986). The martian magnetotail. Advances in space research, 6(1):301–314.

Vaisberg, O., Smirnov, V., and Omelchenko, A. (1977). Solar wind interaction with martian magnetosphere. STIN, 78:23000.

Verigin, M., Gringauz, K., Kotova, G., Remizov, A., Shutte, N., Rosenbauer, H., Livi, S., Richter, A., Riedler, W., Schwingenschuh, K., et al. (1993). The dependence of the martian magnetopause and bow shock on solar wind ram pressure according to phobos 2 taus ion spectrometer measurements. Journal of Geophysical Research: Space Physics, 98(A2):1303–1309.

Wang, Y.-C., Luhmann, J. G., Fang, X., Leblanc, F., Johnson, R. E., Ma, Y., and Ip, W.-H. (2015). Statistical studies on mars atmospheric sputtering by precipitating pickup o+: Preparation for the maven mission. Journal of Geophysical Research: Planets, 120(1):34–50.

Watson, C., Haff, P., and Tombrello, T. (1980). Solar wind sputtering effects in the atmospheres of mars and venus. In Lunar and Planetary Science Conference Proceedings, volume 11, pages 2479–2502.

Weber, T., Brain, D., Mitchell, D., Xu, S., Connerney, J., and Halekas, J. (2017). Characterization of low-altitude nightside martian magnetic topology using electron pitch angle distributions. Journal of Geophysical Research: Space Physics, 122(10):9777–9789.

Weber, T., Brain, D., Mitchell, D., Xu, S., Espley, J., Halekas, J., Lillis, R., and Jakosky, B. (2019). The influence of solar wind pressure on martian crustal magnetic field topology. Geophysical Research Letters.

Weber, T., Brain, D., Mitchell, D., Xu, S., Espley, J., Halekas, J., Lillis, R., and Jakosky, B. (2020). The influence of interplanetary magnetic field direction on the topology of martian crustal field cusps. Geophysical Research Letters.

West, H., Buck, R., and Walton, J. (1973). Electron pitch angle distributions throughout the magnetosphere as observed on ogo 5. Journal of Geophysical Research, 78(7):1064–1081.

Williams, D., Mauk, B., McEntire, R., Roelof, E., Armstrong, T., Wilken, B., Roederer, J., Krimigis, S., Fritz, T., Lanzerotti, L., et al. (1997). Energetic particle signatures at ganymede: Implications for ganymede's magnetic field. Geophysical research letters, 24(17):2163–2166.

Wood, B. E. (2006). The solar wind and the sun in the past. Space Science Reviews, 126(1-4):3–14.

Wordsworth, R. D. (2016). The climate of early mars. Annual Review of Earth and Planetary Sciences, 44:381–408.

Wray, J. J., Murchie, S. L., Bishop, J. L., Ehlmann, B. L., Milliken, R. E., Wilhelm, M. B., Seelos, K. D., and Chojnacki, M. (2016). Orbital evidence for more widespread carbonate-bearing rocks on mars. Journal of Geophysical Research: Planets, 121(4):652–677.

Xu, S., Fang, X., Mitchell, D. L., Ma, Y., Luhmann, J. G., DiBraccio, G. A., Weber, T., Brain, D., Mazelle, C., Curry, S. M., et al. (2018a). Investigation of martian magnetic topology response to 2017 september icme. Geophysical Research Letters, 45(15):7337–7346.

Xu, S., Liemohn, M. W., and Mitchell, D. L. (2014a). Solar wind electron precipitation into the dayside martian upper atmosphere through the cusps of strong crustal fields. Journal of Geophysical Research: Space Physics, 119(12).

Xu, S., Liemohn, M. W., Mitchell, D. L., and Smith, M. D. (2014b). Mars photoelectron energy and pitch angle dependence on intense lower atmospheric dust storms. Journal of Geophysical Research: Planets, 119(7):1689–1706.

Xu, S., Mitchell, D., Liemohn, M., Dong, C., Bougher, S., Fillingim, M., Lillis, R., McFadden, J., Mazelle, C., Connerney, J., et al. (2016). Deep nightside photoelectron observations by maven swea: Implications for martian northern hemispheric magnetic topology and nightside ionosphere source. Geophysical Research Letters, 43(17):8876–8884.

Xu, S., Mitchell, D., Liemohn, M., Fang, X., Ma, Y., Luhmann, J., Brain, D., Steckiewicz, M., Mazelle, C., Connerney, J., and Jakosky, B. (2017a). Martian low-altitude magnetic topology deduced from maven/swea observations. Journal of Geophysical Research: Space Physics, 122(2):1831–1852. 2016JA023467.

Xu, S., Mitchell, D., Luhmann, J., Ma, Y., Fang, X., Harada, Y., Hara, T., Brain, D., Weber, T., Mazelle, C., et al. (2017b). High-altitude closed magnetic loops at mars observed by maven. Geophysical Research Letters, 44(22):11–229.

Xu, S., Mitchell, D. L., McFadden, J. P., Collinson, G., Harada, Y., Lillis, R., Mazelle, C., and Connerney, J. (2018b). Field-aligned potentials at mars from maven observations. Geophysical Research Letters, 45(19):10–119.

Xu, S., Mitchell, D. L., McFadden, J. P., Fillingim, M. O., Andersson, L., Brain, D. A., Weber, T., Schneider, N. M., Jain, S., Fowler, C. M., et al. (2020a). Inverted-v electron acceleration events concurring with localized auroral observations at mars by maven. Geophysical Research Letters, 47(9):e2020GL087414.

Xu, S., Mitchell, D. L., Weber, T., Brain, D. A., Luhmann, J. G., Dong, C., Curry, S. M., Ma, Y., DiBraccio, G. A., Halekas, J., et al. (2020b). Characterizing mars's magnetotail topology with respect to the upstream interplanetary magnetic fields. Journal of Geophysical Research: Space Physics, 125(3):no–no.

Xu, S., Thiemann, E., Mitchell, D., Eparvier, F., Pawlowski, D., Benna, M., Andersson, L., Liemohn, M. W., Bougher, S., and Mazelle, C. (2018c). Observations and modeling of the mars low-altitude ionospheric response to the 10 september 2017 x-class solar flare. Geophysical Research Letters, 45(15):7382–7390.

Xu, S., Weber, T., Mitchell, D. L., Brain, D. A., Mazelle, C., DiBraccio, G. A., and Espley, J. (2019). A technique to infer magnetic topology at mars and its application to the terminator region. Journal of Geophysical Research: Space Physics.

Yamauchi, M., Hara, T., Lundin, R., Dubinin, E., Fedorov, A., Sauvaud, J.-A., Frahm, R., Ramstad, R., Futaana, Y., Holmstrom, M., et al. (2015). Seasonal variation of martian pick-up ions: Evidence of breathing exosphere. Planetary and Space Science, 119:54–61.

Yau, A. W., Abe, T., and Peterson, W. (2007). The polar wind: Recent observations. Journal of atmospheric and solar-terrestrial physics, 69(16):1936–1983.

Yeroshenko, Y., Riedler, W., Schwingenschuh, K., Luhmann, J., Ong, M., and Russell, C. (1990). The magnetotail of mars: Phobos observations. Geophysical Research Letters, 17(6):885–888.

Zahnle, K. J. and Kasting, J. F. (1986). Mass fractionation during transonic escape and implications for loss of water from mars and venus. Icarus, 68(3):462–480.

Zhang, T., Lu, Q., Baumjohann, W., Russell, C., Fedorov, A., Barabash, S., Coates, A., Du, A., Cao, J., Nakamura, R., et al. (2012). Magnetic reconnection in the near venusian magnetotail. Science, 336(6081):567–570.

Zhang, X.-J., Thorne, R., Ma, Q., Li, W., Mauk, B., Paranicas, C., Haggerty, D., Connerney, J., and Bolton, S. (2017). Searching for low-altitude magnetic field anomalies by using observations of the energetic particle loss cone on juno. Geophysical Research Letters, 44(10):4472–4480.

Zhang, Y., Shen, C., Marchaudon, A., Rong, Z., Lavraud, B., Fazakerley, A., Yao, Z., Mihaljcic, B., Ji, Y., Ma, Y., et al. (2016). First in situ evidence of electron pitch angle scattering due to magnetic field line curvature in the ion diffusion region. Journal of Geophysical Research: Space Physics, 121(5):4103–4110.